

Professur für Hydrologie
der Albert-Ludwigs-Universität Freiburg i. Br.

Maximilian Kehl

Mapping of late seasonal snow patterns with unmanned aerial systems in a high alpine environment

Masterarbeit unter Leitung von Prof. Dr. Markus Weiler
Freiburg i. Br., Januar 2020

Professur für Hydrologie
der Albert-Ludwigs-Universität Freiburg i. Br.

Maximilian Kehl

Mapping of late seasonal snow patterns with unmanned aerial systems in a high alpine environment

Referent: Prof. Dr. Markus Weiler

Korreferent: Prof. Dr. Thomas Vikhamar Schuler

Masterarbeit unter Leitung von Prof. Dr. Markus Weiler
Freiburg i. Br., Januar 2020

Information about the author

Name: Maximilian Kehl
Address: Tirolerweg 14
79111 Freiburg im Breisgau, Germany
E-mail: maxi.kehl@gmx.de
Phone: +49 176 57861557
Studies: Hydrology Master of Science, fourth semester
Matriculation number: 3709759

© Maximilian Kehl 2020

Acknowledgements

First of all, I would like to thank my supervisors, Markus Weiler at the Institute of Hydrology in Freiburg and Thomas Schuler at the Section of Physical Geography and Hydrology in Oslo for the proposition of this topic and for making this binational collaboration possible.

A special thanks goes to Markus Weiler, not only for his constant support and scientific advice, but also for entrusting me with this topic and integrating me into the HILLSCAPE project, inter alia compensating for overnight stays at the Klausen Pass. I am also very thankful for the support of Sven Decker. I am grateful for his reviews on my work, his participation in relevant discussions, the one-day field-support, and generally for always having a sympathetic ear.

A sincere thanks goes to the Professorship of Remote Sensing and Landscape Information Systems for lending me the drone and providing computers for the remote sensed data processing. Without the agreement of Barbara Koch and Holger Weinacker this would not had been possible. I am particularly thankful to Julian Frey's scientific advice, especially in the fields of remote sensing and structure-from-motion processing.

Furthermore, I thank the Department of Geography, Remote Sensing at the University of Zurich for loaning the Trimble Device to me. A special thanks goes to Alessandra Musso for giving me the necessary initial aid but also Julian Djamil Fagir for his counsel in coordinate conversion.

I am also grateful to Alexander Krämer for the executed test flight before the study started to familiarize with the drone. Without his cooperativeness to borrow the indispensable batteries, the campaign could not had been realized that early.

I also thank Jonas Zimmermann and Britta Kattenstroth from the Hydrometry workshop for always providing me with the necessary gear and Jürgen Strub for being company and his support during the first flight mission.

Last but not least, of course I want to thank my proofreaders, friends, family and great girlfriend Lara for their constant support.

Abstract

The spatial distribution of snow is complex and difficult to capture as it depends on multiple factors. In order to assess the water resource potential and to understand interactions between land and atmosphere, a precise quantification of the latter is desirable. While earlier but still, studies in snow science addressing the prediction of snow depth (HS) and its distribution focused on the extrapolation of sparse station data measurements, during the latest years high resolution and continuous data of Terrestrial and Airborne laser scanning found wide application. Those however are costly and only sporadic available. Lately, the potential of digital photogrammetry in capturing the small scale variability of HS is utilized and poses an economic method to map snow parameters on high temporal frequencies on the catchment scale. In order to improve statistical modeling of HS distribution in a high alpine terrain, five *digital surface models* (DSM) with an unmanned aerial system (UAS) in combination with structure-from-motion photogrammetry were generated. A catchment of 3 km² with a mean elevation of 1994 m a.s.l in the Swiss Alps was chosen as a study site. In comparison to other studies the present focusses on the ablation season and captures HS after its peak accumulation. In this context the target is to find out whether and to which extent the remaining characteristic snow distribution can be linked to topographic parameters, and if so, the captured status of the snow cover and its spatial distribution can be predicted with multiple linear regressions. Snow depth was retrieved by subtracting the snow-free DSM from the snow-covered DSMs. A high precision of the subsequent and co-registered DSMs with a geolocation accuracy of ± 20 cm could be determined. The validation of the modeled HS against more than 250 hand-probed measurements produced a RMSE of 0.62, though has to be considered as rather inappropriate dimension due to a GPS geolocation error of 10 m. From the high-resolution DSMs and snow density measurements (up to 590 kg m⁻³), snow water equivalent and total volume loss between each survey could be determined in high accuracy. The collected RGB data was inappropriate for automatic snow cover classification. This study found that UAS surveys in karstified areas, represent a challenge in discrimination of karst- and snow pixels because of their spectral similarity. From the retrieved model outcomes (1 m resolution), it can be concluded that late seasonal HS distribution cannot be linked significantly to topography impeding its precise prediction on that scale. However, the results clearly show the importance of a wind shelter parameter and elevation in explaining HS distribution, and thus highlight their importance in future snow studies. Utilizing satellite data (10 m resolution) to calculate snow cover extent and subsequently link those areas to topographic parameters (derived from a high resolution DSM) resulted in comparable findings, since snow cover could not be modeled in great detail.

Keywords: *remote sensing, photogrammetry, UAS, satellite imagery, snow depth distribution, snow cover area, snow cover modeling, multiple regression, ablation, snow hydrology*

Kurzzusammenfassung

Die räumliche Verteilung von Schnee ist komplex und schwer zu erfassen, da sie von mehreren Faktoren abhängt. Um Aussagen über die Wasserverfügbarkeit treffen zu können sowie die Wechselwirkungen zwischen Boden und Atmosphäre nachzuvollziehen, sind präzise Informationen über die Schneehöhe (HS) im Einzugsgebiet erstrebenswert. Die Modellierung von HS in vergangenen, aber auch rezenten schneehydrologischen Studien basiert meistens maßgeblich auf der Extrapolation von vereinzelten Stationsdatenmessungen. In den letzten Jahren fanden (jedoch) vermehrt durch Airborne und Terrestrial Laser Scanning erhobene, kontinuierliche und hochaufgelöste HS Daten eine breite Anwendung. Diese Methode ist jedoch kostenintensiv (und nur sporadisch verfügbar), weshalb zunehmend das Potential von digitaler Photogrammetrie zur Erfassung der kleinräumigen Variabilität von HS an Bedeutung gewinnt. Dies stellt eine wirtschaftliche Methode dar, um Schneeparameter mit hoher zeitlicher Auflösung auf Einzugsgebietsebene zu kartieren. Um die statistische Modellierung der HS in hochalpinem Gelände zu verbessern, wurden in dieser Studie fünf digitale Oberflächenmodelle (DOM) mit einer Starrflügler-Drohne in Kombination mit structure-from-motion Prozessen generiert. Als Versuchsgebiet wurde eine etwa 3 km^2 große Fläche mit einer mittleren Höhe von 1994 m ü. NN in den Schweizer Alpen ausgewählt. Im Vergleich zu anderen Studien konzentrierte sich die vorliegende Arbeit auf den Ablationszeitraum und erfasst die HS deutlich nach dem Akkumulationsmaximum. Ein Ziel der Arbeit war es zu untersuchen, ob sich die erfasste Schneebedeckung und Schneehöhenverteilung mit topographischen Parametern in Zusammenhang setzen lässt und ob dieser Zusammenhang mittels multipler linearer Regression modelliert werden kann. Schneehöhe wurde durch die Differenz von schneebedecktem und schneefreiem DOM ermittelt. Für die zeitlich aufeinander folgenden und koregistrierten DOMs konnte eine hohe Präzision mit einer Schneehöhen-Genauigkeit von $\pm 20 \text{ cm}$ festgestellt werden. Die Validierung der modellierten HS gegen mehr als 250 Handmessungen ergab einen RMSE von 0,62, der allerdings aufgrund des GPS-Geolokalisierungsfehlers von 10 m als eher ungeeignetes Maß zu betrachten ist. Auf Basis der hochaufgelösten Information über HS und den durchgeführten Schneedichtemessungen (bis zu 590 kg m^{-3}) konnte das Schneewasseräquivalent und das Volumen der Schneeschmelze zwischen den jeweiligen Befliegungszeitpunkten mit hoher Genauigkeit bestimmt werden. Die Informationen der erhobenen RGB-Bilder waren für eine automatische Schneeklassifizierung ungeeignet. Eine zusätzliche Herausforderung in der Diskriminierung von schneebedeckten und schneefreien Bereichen mittels RGB-Daten stellt die spektrale Ähnlichkeit von Karst- und Schneepixeln dar. Die Modellergebnisse (1 m Auflösung) zeigen, dass keine signifikanten Korrelationen zwischen topografischen Parametern und der Schneehöhenverteilung im Ablationszeitraum bestehen, was eine präzise Modellierung der HS verhindert. Nichtsdestotrotz konnte die Relevanz der Geländehöhe und des Windparameters S_x bei der Modellierung der Schneehöhenverteilung

gezeigt werden. Die Verwendung von Informationen aus Satellitenbildern (10 m Auflösung) zur Berechnung der Schneebedeckung und die anschließende Verknüpfung dieser Gebiete mit aus einem hochaufgelösten DOM abgeleiteten topographischen Parametern lieferten vergleichbare Ergebnisse. Auch hier konnte durch multiple logistische Regression die Schneebedeckung nicht detailliert modelliert werden.

Schlüsselworte: *Fernerkundung, Photogrammetrie, Drohne, Satellitenbilder, Schneehöhenverteilung, Schneebedeckung, Multiple Regression, Schneedeckenmodellierung, Ablation, Schneehydrologie*

Table of Contents

1	Introduction.....	1
1.1	Importance of snow: its distribution and relevance.....	1
1.1.1	Scientific findings and state of the art.....	2
1.2	Theoretical background: methods to quantify snow height and distribution.....	3
1.2.1	Snow monitoring stations and hand probe HS measurements.....	3
1.2.2	Optical and micro-wave data from satellite platforms.....	3
1.2.3	LiDAR altimetry – Airborne & Terrestrial laser scanning.....	5
1.2.4	Digital photogrammetry.....	6
1.3	Motivation and objective.....	8
1.3.1	Motivation.....	8
1.3.2	Objectives: methodology and thesis overlook.....	9
2	Methods and data	13
2.1	Study area.....	13
2.2	Data acquisition.....	17
2.2.1	UAS surveys.....	17
2.2.1.1	Unmanned aerial vehicle.....	17
2.2.2	Flight planning.....	19
2.2.2.1	On-site preparation and flight execution.....	20
2.2.3	Differential Global Navigation Satellite System survey.....	22
2.2.4	Satellite imagery.....	26
2.2.4.1	Extracting SCA information from satellite data.....	26
2.2.5	Manual snow depth measurements.....	28
2.2.6	Manual snow density measurements.....	29
2.2.7	Meteorological data.....	29
2.3	Data processing.....	30
2.3.1	Processing image data.....	30
2.4	Geospatial analysis.....	34
2.4.1	Quantification of SCA.....	34
2.4.1.1	Automatic classification.....	34
2.4.1.2	Manual classification.....	37
2.4.2	Snow depth distribution.....	37
2.4.3	Multiple linear regression and multiple logistic regression model.....	37
2.4.3.1	Multiple regression with recorded data.....	37
2.4.3.2	Multiple regression with satellite data.....	39
2.4.3.3	Effect size.....	39

3	Results	41
3.1	Orthophotos	42
3.2	Accuracy of digital photogrammetry products	43
3.2.1	Horizontal and vertical accuracy of GCPs	43
3.2.2	Vertical accuracy of control points in photogrammetric DSMs	46
3.3	Snow depth maps	50
3.3.1	Snow depth validation using the manual snow depth measurements as reference data set	52
3.4	Snow cover area	54
3.4.1	Comparison of SCA with SENTINEL-2 data	54
3.5	Snow water equivalent and ablation rates	57
3.6	Geospatial analysis	60
3.6.1	Statistical preliminary investigations	60
3.6.1.1	Explanatory variables and their distributions	60
3.6.1.2	Correlations between explanatory parameters and response variable HS	64
3.6.1.3	Principal component analysis	66
3.6.2	Multiple linear regression models	68
3.6.2.1	Modeling of snow-covered and snow-free areas	69
3.6.2.2	Modeling of snow depth	72
3.6.2.3	Modeling of ablation	73
3.6.3	Differences between snow-free and snow-covered areas	75
3.6.3.1	Empirical cumulative density functions	75
3.6.3.2	Effect size	78
3.6.3.3	Areas of first snowmelt	78
4	Discussion	81
5	Conclusions and recommendations for future research	89
6	References	93
7	Appendix	103
7.1	List of Abbreviations	103
7.2	Figures	104
7.3	Tables	112

List of Figures

Fig. 2.1:	Hypsometry and statistics of the study site.	15
Fig. 2.2:	View on the study site as seen from Märcher Stöckli (line of sight: South). Besides, the Figure shows the highest mountain around, Clariden (3267 m a.s.l.) and Klausen Pass (1948 m a.s.l.).	16
Fig. 2.3:	Components of the eBee Classic.	17
Fig. 2.4:	eBee.	18
Fig. 2.5:	Polygonal mission area, DEM and flight plan in the eMotion software and generated snow-free 3D model of study site.	19
Fig. 2.6:	Take off location (2300 m a.s.l.) at alternative study site near HILLSCAPE research project field site. Line of sight is east.	22
Fig. 2.7:	Illustration of dGNSS measurement setup with Trimble R7 GPS antenna and receiver fixed on ranging rod and ranging pole tripod (top). Dual-frequency rover antenna (lower left). Receiver and controller (lower middle). Example of photo-identifiable targets as GCP (lower middle & right).	24
Fig. 2.8:	Scale, tube, shovel and avalanche probe.	28
Fig. 2.9:	Tilt of cam.	31
Fig. 2.10:	Manual and automatic (threshold value in blue band) classification of snow cover June 28 th , 2019. Manual represents the <i>real</i> snow cover classification mask.	36
Fig. 3.1:	Flight lines and image capture locations for the five UAV missions.	41
Fig. 3.2:	Maps of image overlap for the five UAV missions.	42
Fig. 3.3:	Orthophotos of the five UAS surveys (Scale: 1:45,000).	43
Fig. 3.4:	Image residuals for Canon IXUS 127 HS (Focal length = 4.3 mm) from camera calibration procedure for UVAs surveys (first = left, last = right).	44
Fig. 3.5:	Orthophoto sections of each survey with GCP 4 to get an impression of the horizontal accuracy.	45
Fig. 3.6:	Orthophoto extract of survey 1 (left) and 5 (right). Point 1 and 2 indicate points with same XY coordinate.	46
Fig. 3.7:	Spatial distribution of the deviation in z-direction (m) between the snow-covered DSMs (DSM1 = upper left; DSM2 = lower left; DSM3 = upper right; DSM4 = lower right) and the snow-free DSM. Pink color represents areas with a deviation smaller - 1 and black dots are locations of the GCPs.	48
Fig. 3.8:	Snow depth maps of the four different surveys retrieved from the corrected DSMs (15 cm resolution).	50
Fig. 3.9:	Boxplots of the HS data from the 4 different surveys (1 m resolution).	50
Fig. 3.10:	Stepwise depletion of the snow cover, exemplary for areas at the study site with initially greatest HS.	51
Fig. 3.11:	Orthophotos of the single flight missions with location and snow depth (m) of manual measurements.	52

Fig. 3.12: Absolute median values of manual and modeled HS (cm) for the four surveys.	53
Fig. 3.13: Real color composite images of study site derived from SENTINEL-2 data (Band 2, 3, 4).....	56
Fig. 3.14: NDSI maps of study site derived from SENTINEL-2 data (Band 3, 11).....	57
Fig. 3.15: Absolute ablation in cm and ablation rate in cm per day for the corresponding periods between the UAS surveys.	58
Fig. 3.16: Data of the IMIS stations <i>Alpler Tor</i> and <i>Schächentaler Windgällen</i> between Oct 1 st , 2018 and Sep 30 th , 2019. Snow depth in cm (HS), 24-h new snow in cm (HN), Air (TA) and snow surface (TS) temperature in °C, wind speed in km h ⁻¹ as daily mean (VW), daily mean maximum(VW_MAX),daily maximum (VW_MAX_MAX) and wind direction as daily mean (DW).....	59
Fig. 3.17: Hydrograph of daily mean of the Schächen from January to August 2019 (FOEN, 2019).....	60
Fig. 3.18: Maps of predictory variables elevation, slope, aspect, solar radiation, terrain parameter Sx and curvature underlayed with hill shade (1m resolution).....	61
Fig. 3.19: View of how wind speed and wind direction are distributed for both winter (left) and summer (right) season according to data of the wind station <i>Gross Windgällen</i> illustrated as wind rose.	61
Fig. 3.20: Histogram for each explanatory variable at the study site with normal curve with the corresponding mean and standard deviation.	62
Fig. 3.21: Histogram of HS at the study site for each survey with normal curve with the corresponding mean and standard deviation.	64
Fig. 3.22: Correlation plot with correlation coefficients of dependent variable HS with predictor variables for the four UAS surveys (1m resolution).	65
Fig. 3.23: Correlation plot with correlation coefficients of dependent variable <i>snow-covered/snow-free</i> with predictor variables for the four UAS surveys (1m resolution).	66
Fig. 3.24: Scree plot of the principal components.....	67
Fig. 3.25: Quality of representation of the explanatory variables on the first two principal components.	68
Fig. 3.26: GLM output for Snow Cover Extent of June 28 th , 2019. Original (left) and predicted (right) SCA. As predictory variables were used Sx and elevation.	70
Fig. 3.27: GLM output for Snow Cover Extent of June 28 th , 2019. Original (left) and predicted (right) SCA. As predictory variables were used Sx, elevation, slope, radiation and curvature (10 m resolution).....	71
Fig. 3.28: GLM output for Snow Cover Extent of June 29 th , 2019. Satellite record (left) and predicted (right) SCA. As predictory variables were used Sx, elevation, slope, radiation and curvature (10 m resolution).....	71
Fig. 3.29: LM output for Snow depth of June 28 th , 2019. Original (left) and predicted (right) SCA. As predictor variables were used Sx and elevation.	72
Fig. 3.30: Solar radiation maps (Wh m ⁻² d ⁻¹) on hill shade with polygons of snow cover extent. Snow cover extent of June 28 th , for period from June 28 th to July 10 th , snow cover	

extent of July 10 th for period from July 10 th to 17 th and snow cover extent of July 17 th for period from July 17 th to 24 th	73
Fig. 3.31: LM output for Ablation of between June 28 th and July 10 th , 2019. Original (left) and predicted (right) ablation. As predictor variables were used radiation, Sx and elevation.	74
Fig. 3.32: ECDF of each predictor variable for June 28 th , 2019 (1 m resoulution).	76
Fig. 3.33: ECDF of each predictor variable for July 10 th , 2019 (1 m resoulution).	76
Fig. 3.34: ECDF of each predictor variable for July 17 th , 2019 (1 m resoulution).	77
Fig. 3.35: ECDF of each predictor variable for July 24 th , 2019 (1 m resoulution).	77
Fig. 3.36: 10 m resolution NDSI June 19 th , 2019 (threshold 0.42). Day where first areas of snow cover were melted to ground. Cumulative density function of each predictor variable. X-axis adjusted to illustrate the shift better. Comparison of the distribution of each parameter for the whole site and for only snow pixels.	79

List of Maps

Map 2.1: Location map of the study site within Switzerland.....	13
Map 2.2: Elevation (m) and hillshade map of the study site within Switzerland.	14
Map 2.3: Aspect and slope within the study site (15 cm resolution) and its surrounding (20 m resolution).	16
Map 2.4: Location of GNSS measurements (GCPs), control points and take-off & landing location at the Klausen Pass field site.	24
Map 2.5: Landsat Mosaic 25 m with location of IMIS stations and runoff station in relation to the Klausen Pass study site.	30
Map 3.1: Location of GNSS measurements (GCPs), control points and take-off & landing location at the Klausen Pass field site.	47

List of Tables

Tab. 1.1: Overview of the most important strengths and weaknesses of the applied methods for large-scale snow depth mapping in high-alpine terrain	7
Tab. 2.1: Key parameters of the UAS missions. Date, Time (in MESZ), N (number of images/flights), Height (average flight height in m above ground level), FL (Focal Length in mm), ISO, SS (Shutter speed), GSD (Ground sampling distance in cm pix ⁻¹), A (area covered in km ²), GCPs (Number of GCPs).	21
Tab. 2.2: Meteorological conditions at 12:00 (IMIS measuring station <i>Alpler Tor</i> at 2338 m a.s.l. and located 387 m higher and 6.5 km northwest of Klausen Pass) and field notes during flight missions.	21

Tab. 2.3: Corrected dGNSS measurements from September 12 th , 2019 with discrimination of measurement technique.....	25
Tab. 2.4: Positioning specifications for the Trimble R7.....	25
Tab. 2.5: Spectral bands for the SENTINEL-2A sensor.....	26
Tab. 2.6: SENTINEL-2 product types.....	27
Tab. 2.7: Swiss coordinates (CH1903+/LV95) of the extent of the generated DSMs and orthophotos for the 5 UAS surveys (x = East, y = North).....	34
Tab. 2.8: Differences between groups, effect size measured by Glass's Δ	40
Tab. 3.1: Ground control points RMSE (X – Easting, Y – Northing, Z – Altitude).	44
Tab. 3.2: RMSE of GCP 4 for the several generated DSMs.....	45
Tab. 3.3: Elevation value (z) and deviation to dGNSS measurement exemplary for GCP 4. ..	45
Tab. 3.4: Elevation (in m) of control points in generated DSMs.	46
Tab. 3.5: Deviation (in cm) of control points from reference DSM5. High deviations are marked in red.....	47
Tab. 3.6: Mean deviation of the several DSMs in respective to DSM 5.	49
Tab. 3.7: Quantiles of the four recorded HS distributions.	51
Tab. 3.8: RMSE of modeled and probed snow depth for the 4 UAS surveys.	53
Tab. 3.9: Snow cover extent in square metres, square kilometres and percentage of the total study area (2.91 km ²) derived from the orthophotos from the UAS missions.	54
Tab. 3.10: Snow cover extent in square metres, square kilometres and percentage of the total study area derived from the NDSI from SENTINEL-2 bands. Green marked rows represent satellite records temporally close or equal to the UAS missions.....	55
Tab. 3.11: Characteristic snow depth values (mean, median, maximum HS), snow density q, snow water equivalent SWE, snow volume V at each day of UAS survey and runoff rate Q of snow covered areas between the UAS surveys.....	58
Tab. 3.12: Statistics (minimum, maximum, mean, median (50%), 25% and 75% quantile) about explanatory variables at study site (1 m resolution).	63
Tab. 3.13: Skewness and kurtosis of explanatory variables and HS (1m resolution).	63
Tab. 3.14: Correlation coefficients of biserial correlation between categorical <i>snow-free/ snow-covered</i> data and continuous explanatory variables.	65
Tab. 3.15: Rotation matrix of the PCA.	68
Tab. 3.16: Effect size of each predictory variable for the four UAV surveys(1m resolution). Strong effect size is marked in green.....	78
Tab. 3.17: 25, 50 and 75% quantiles of parameters of interest for the whole study site. For snow-covered and snow-free areas the deviance to the study site is listed (green = positive shift).....	79
Tab. 3.18: Effect size of each predictory variable for the NDSI of June 19 th , 2019 (10 m resolution). Strong effect size is marked in green.	80

List of Figures in the Appendix

Fig. A1:	Absolute mean values of manual (Buffer of 10 m) and modeled HS (cm) for the four surveys.	104
Fig. A2:	Correlation plot with correlation coefficients of dependent variable HS and predictor variables for the 4 UAS surveys (10 m resolution).	105
Fig. A3:	GLM output for Snow Cover Extent of July 10 th (1), 17 th (2) and 24 th (3), 2019. Original (left) and predicted (right) SCA. As predictory variables were used Sx and elevation.	106
Fig. A4:	LM output for Snow depth of July 10 th (1), 17 th (2) and 24 th (3). Original (left) and predicted (right) snow depth. As predictor variables were used Sx and elevation.	107
Fig. A5:	LM output for Snow depth of June 28 th , 2019. Original (left) and predicted (right) SCA. As predictor variables were used Sx, elevation, slope and curvature.	108
Fig. A6:	Diagnostical illustrations of the regression-analysis of the LM with HS as dependent variable (June 28 th , 2019).	109
Fig. A7:	LM output for ablation between July 10 th and 17 th (1) and July 17 th and 24 th (2), 2019. Original (left) and predicted (right) ablation. As predictor variables were used radiation, Sx and elevation.	110
Fig. A8:	Diagnostical illustrations of the regression-analysis of the LM with ablation as dependent variable (June 28 th –July 10 th , 2019).	111

List of Tables in the Appendix

Tab. A1:	RMSE of GCPs (June 28 th , 2019).	112
Tab. A2:	RMSE of GCPs (July 10 th , 2019).	112
Tab. A3:	RMSE of GCPs (July 17 th , 2019).	112
Tab. A4:	RMSE of GCPs (July 24 th , 2019).	113
Tab. A5:	RMSE of GCPs (September 13 th , 2019).	113
Tab. A6:	Average camera location error (X – Easting, Y - Northing, Z - Altitude).	113

1 Introduction

1.1 Importance of snow: its distribution and relevance

Seasonal snow provides a globally valuable water resource (Mankin et al., 2015; Sturm et al., 2017), which is highly variable in space and time (Clark et al., 2011). Being able to map *snow depth* (HS) over a landscape is desirable for many reasons. In the Northern Hemisphere alone, over 40 million km²—almost half the land surface—becomes covered by snow each winter, making seasonal snow the largest annual topographic change on the planet (Déry and Brown, 2007; Lemke et al., 2007).

Snow is an important resource in alpine regions not only for tourism (Elsasser and Bürki, 2002; Nöthiger and Elsasser, 2004; Rixen et al., 2011) but also for hydropower generation, water supply (Farinotti et al., 2012; Marty, 2008), and ecological aspects of the local mountain flora and fauna (Wipf et al., 2009). Billions of people rely on snow in some capacity, whether for drinking water, crop irrigation, or electricity (Barnett et al., 2005). Snow also plays an essential role in the surface energy balance of the planet; it thermally insulates the soil while efficiently reflecting sunlight because of its high albedo (Goodrich, 1982).

The spatio-temporal variability of mountain snow cover determines the snow water storage, permafrost distribution, and the local distribution of plants and animals (Grünwald et al., 2010). Snow is also a hazard, producing avalanches or floods, and thus important for the prevention of avalanches (Castebrunet et al., 2014) and flood forecasting in spring and early summer for the valleys downstream. Information on snow extent, especially when combined with HS to estimate *snow water equivalent* (SWE), is important for water management purposes since it enables basin managers to assess the risk of snowmelt floods (Niedzielski et al., 2018). The amount and timing of the melt strongly depend on the thickness and the spatial distribution of the snow cover. Therefore, the spatiotemporal variability of the snow cover significantly impacts the alpine water balance and strongly affects nature and humankind (Elder et al., 1998). It has been shown that the snow distribution at the winter maximum before the beginning of the melting period strongly determines the temporal evolution of the remaining snow resources and, if converted to SWE (Jonas et al., 2009), the potential melt water runoff during the melting period (Egli, 2011). Several studies have reported a very high spatial variability of HS and other snowpack parameters at different spatial scales in mountainous regions (Egli, 2011; Elder et al., 1991; Grünwald et al., 2010; Lehning et al., 2008; Schweizer et al., 2008). This high variation in snow cover distribution on very small scales requires a high spatial resolution of snow samples to measure different parameters of the snowpack such as the areal mean HS on complex alpine topography and the temporal evolution of *snow-covered areas* (SCA) during the melt period with high areal representativeness and absolute precision. Hence, snowpack monitoring in alpine terrain requires an area-wide observation with a large number of HS point

measurements distributed over the area of interest (Bühler et al., 2015). To make reliable assessments of current and future snow dynamics, it is essential to obtain a better understanding of the total amount of snow stored in a catchment and how snow cover changes in space and time, especially in the ablation period (Grünwald et al., 2010).

Snow is generally quantified in terms of its SWE through measurements of its depth and density. Since density varies less than depth (López-Moreno et al., 2013; Shook and Gray, 1996), much of the spatial variability of SWE can be described by the spatial variability of HS. Thus, the ability to measure HS and its spatial distribution is crucial to assess and predict how the snow water resource responds to meteorological variability and landscape heterogeneity (Harder et al., 2016).

1.1.1 Scientific findings and state of the art

So far, mainly snow deposition and snow transport due to wind have been investigated in great detail (Doorschot et al., 2001; Lehning et al., 2008), and it has been shown that snow distribution influences runoff dynamics in mountain catchments (Lehning et al., 2006). Many of these efforts, however, are based on model studies, and insufficient validation measurements exist. Very often, limited HS and SWE observations are extrapolated to large areas using statistical models (Bavera and Michele, 2009; Chang and Li, 2000; Erickson et al., 2005; López-Moreno and Nogués-Bravo, 2006; Luce et al., 1999; Marchand and Killington, 2004). Currently in most regions (e.g., Swiss Alps), HS is measured at specific locations by automated weather stations or observers in the field, while both observations are restricted to flat sites exhibiting a rather homogeneous snow cover (Bründl et al., 2004; Egli, 2008). These flat field point measurements are assumed to represent snow cover characteristics for a larger area around the stations and are therefore interpolated over large distances and then combined with snow cover information from optical satellites (Foppa et al., 2007). Unfortunately, this method is unable to capture the small-scale variability of HS. Even a dense measurement network (e.g. the one in Switzerland with, on average, more than one measurement station per 10 km²), is not able to capture the large spatial variability of HS present in alpine terrain (Bühler et al., 2016). Investigations into the representability of point HS measurements on HS for entire catchments are sparse (Grünwald and Lehning, 2015).

The latest scientific findings show that HS maps provide geostatistically robust insights into seasonal snow processes in unprecedented detail, resolving snowpack features associated with redistribution and preferential accumulation and ablation (Redpath et al., 2018). This emphasizes the need for accurate and widespread HS mapping.

Currently, many different techniques to monitor HS exist. These techniques will be explained in the following, including a discussion of the advantages and disadvantages, in order to give an understanding of why HS mapping with drones—the objective of this thesis—gained popularity during the last years.

1.2 Theoretical background: methods to quantify snow height and distribution

Nowadays, increasing interest is growing around distributed measurements of snow extent, HS, and SWE (Dietz et al., 2012) that can substitute or integrate point and sparse measurements. Existing techniques include *terrestrial* or *airborne laser scanning* (TLS/ALS) (Dadic et al., 2010; Deems et al., 2006, 2006; Grünewald et al., 2010; Grünewald et al., 2013; Grünewald and Lehning, 2015; Hedrick et al., 2015; Hopkinson et al., 2004; Lehning et al., 2011a; Prokop et al., 2008, 2008; Prokop, 2008b), *tachymetry* (Prokop et al., 2008), *ground penetration radar* (GPR) (Machguth et al., 2006; Wainwright et al., 2017), *synthetic aperture radar* (SAR) (Luzi et al., 2009), *aerial photography* (Blöschl and Kirnbauer, 1992; König and Sturm, 1998; Worby et al., 2008) *time-lapse photography* (Farinotti et al., 2010; Parajka et al., 2012), and *optical and micro-wave data from satellite platforms* (Dietz et al., 2012; Parajka and Blöschl, 2006). The effective performance of these methods has been widely discussed, but survey expenses are still a constraint (Hood and Hayashi, 2010).

1.2.1 Snow monitoring stations and hand probe HS measurements

For many years and even currently, traditional manual methods (snow pits and probing or profiling) (Luzi et al., 2009; Miziński and Niedzielski, 2017), conventional observation stations, and automatic snow and weather stations (Grünewald and Lehning, 2015), such as standalone *snow monitoring stations* (SnoMoS) (e.g., snow pillows and sonic rangiers), have been employed successfully. However, like all point measurements (e.g., HS and SWE), they require statistical modeling to move from limited discrete point data to large areas by extrapolation (Liston et al., 2007; Liston and Sturm, 2002; Serreze et al., 1999; Slater and Clark, 2006).

1.2.2 Optical and micro-wave data from satellite platforms

Remote sensing, led by the help of satellites as an advanced technique, allows for the comprehensive, safe, and spatially continuous monitoring of dynamic and variable snow cover (Eker et al., 2019). SCA is a common parameter measured since it can be detected successfully within the spectral and thermal wavelengths by a range of satellite sensors, and the area and frequency of observation is a function of both spatial and temporal resolution. As described by

Eker et al. (2019) this technique is commonly used due to its global coverage, the regular repeatability of measurements, and the availability of a large number of sensors and platforms.

In particular, the *Advanced Very High Resolution Radiometer* (AVHRR), *Moderate Resolution Imaging Radiometer* (MODIS), *Landsat* (MSS/TM/ETM+/OLI), *SPOT*, and *SPOT-XS* platforms have been used at different pixel resolutions (Crawford et al., 2013; Haefner et al., 1997; Hall et al., 1995). Snow observation is inhibited by sensor saturation problems in addition to cloud cover, which both obscure the snow surface and exhibit some spectral overlap with snow. Several developed techniques allow snow/cloud discrimination, with varying degrees of success. The close correspondence of the distribution of snow cover with terrain has also enabled the interpolation of snow cover into cloud obscured regions. Shadows from terrain generally confuse the location of snow-covered pixels, and procedures correcting for the variation in illumination have been generated. The detection of the snow/no snow boundary and subsequent estimation of snow area has been achieved by using a variety of approaches ranging from interactive delineation and planimetry or thresholding to multi-temporal analysis and more sophisticated gridding or digital techniques (Lucas and Harrison, 1990).

Remote sensing of snow coverage using *optical sensors* is relatively routine. Still, remote sensing of HS or SWE based on the *microwave* emissivity or radar scattering properties of the snow requires complex and problematic inversions in order to infer the depth and has coarse spatial resolution (25 km) (Clifford, 2010; Rittger et al., 2013; Rott et al., 2008). The results do not display small-scale snow cover characteristics of alpine catchments. Microwave radiometry is very sensitive to the presence of snow on soil. It is used for estimating SWE and melting/refreezing cycles at both basin (Macelloni et al., 2005) and global scales combined with optical and active sensors (Tedesco and Miller, 2007). It does, however, have difficulty in distinguishing wet snow from wet soil and, at lower frequencies, usually suffers from a limited spatial resolution.

Synthetic Aperture Radar (SAR) interferometry evaluates snow mass characteristics based on relating the measured interferometric phase shift to a change in the snow mass (Luzi et al., 2009). Active microwave sensors (e.g., SAR) use much smaller wavelengths (millimeters to centimeters) and achieve finer spatial resolutions of up to 20 m (Dozier and Shi, 2000; Schanda et al., 1983). However, this method is limited to dry snowpacks and faces problems in steep high-alpine terrain (Buchroithner, 1995). The use of *SAR images* aimed at snow monitoring from satellites has been around since the 1990s (Bernier and Fortin, 1998; Kendra et al., 1998). In comparison, the use of *differential SAR interferometry* (DInSAR) to monitor dry snow is a rather new application (Guneriusson et al., 2001; Oveisgharan and Zebker, 2007). Lately, microwave interferometry has been applied through *ground-based SAR interferometry* (GB SAR) configuration to estimate HS from interferometric phase (Martinez-Vazquez et al., 2005) (C-band) along with the experimentation described in Luzi et al. (2009) (C- and S-bands). *GB*

SAR backscattering measurements have also been carried out at higher frequencies (X- and Ku-bands) (Morrison et al., 2007).

Until today, problems in quantifying HS remain primarily due to the heterogeneity of terrain complexity and vegetation cover (Harder et al., 2016).

1.2.3 LiDAR altimetry - Airborne & Terrestrial laser scanning

A technique that has received considerable attention in recent years and is often applied as the preferred method to obtain HS data is to measure the elevation of the snow surface by airborne or ground-based *Light Detection and Ranging* (LiDAR) and subtract from this the snow-free surface elevation with the difference interpreted as HS (Deems et al., 2013; Egli et al., 2012; Grünewald et al., 2010; Grünewald et al., 2014; Hopkinson et al., 2004; Prokop, 2008a, 2008b).

LiDAR altimetry is a promising method to obtain areawide high-resolution HS data (Grünewald et al., 2010). To date, LiDAR techniques have provided the highest-resolution estimates of HS spatial distribution from both terrestrial (Grünewald et al., 2010) and airborne (Hopkinson et al., 2012) platforms.

TLS was previously used to derive spatially continuous HS (Grünewald et al., 2010; Prokop, 2008b)). Even though the accuracy of such measurements is very high (usually better than 0.1 m, depending on laser footprint and distance from sensor), largescale catchments cannot be covered completely. Data acquisition with TLS is time and manpower consuming and only applicable to easily accessible areas (sensor viewshed) under fair conditions (depending on the avalanche situation, weather) and for areas within the line of sight of the measurement location. This results in limited coverage and many data gaps, e.g., behind bumps. ALS from helicopters or airplanes can cover larger areas in a shorter time also under difficult avalanche danger situations. Recent studies demonstrate that the accurate mapping of HS is possible (Deems et al., 2013; Melvold and Skaugen, 2013). Typically, airborne LiDAR provides data with a *ground sampling distance* (GSD) of nearly 1 m and a vertical accuracy of 15 cm (Deems et al., 2013; Deems and Painter, 2006). While detailed, this resolution still does not provide observations of the spatial variability of snow distributions that can address microscale processes such as snow–vegetation interactions or wind redistribution in areas of shallow snow cover. Additionally, the frequency of airborne LiDAR observations is typically low, except for NASA’s Airborne Snow Observatory applications (Mattmann et al., 2014). Nonetheless, the main limitation encountered is the high costs and long lead time needed for planning repeat flights for the aerial scanner to cover large areas (Bühler et al., 2012; Deems et al., 2013), and overflights are, as with digital photogrammetry, restricted to fair weather conditions (Bühler et al., 2015).

1.2.4 Digital photogrammetry

In addition to satellite remote sensing, aerial imagery has been frequently used for mapping HS. *Digital surface models* (DSMs) can be calculated from optical imagery acquired from two different viewing angles using photogrammetric image correlation techniques (Bühler et al., 2012). Operating on the similar principles of repeat or overlapping coverage, but pre-dating LiDAR studies by 30 years, airborne and terrestrial photogrammetry for determining HS were seriously investigated starting in the 1960s, though little published information is currently available (McKay, 1968). At that time, lacking any other method of mapping HS at the landscape scale using scanned aerial imagery from manned aircrafts (Smith et al., 1967), it was an obvious technique to consider as it was already being used for the study of glaciers (Brandenberger, 1959; Hamilton, 1965; Post, 1969, 1995).

The topic was investigated in detail by Cline (1993, 1994). However, his results suffer from image saturation and insufficient reference data which led him to the conclusion that *photogrammetry* has much potential but is not yet accurate enough for large-scale HS mapping. Ledwith and Lundén (2001) used scanned aerial imagery to derive digital elevation models over glaciated and snow-covered areas in Norway. They report a mean accuracy of 2.8 m in comparison to *differential Global Navigation Satellite System* (dGNSS) transects, which is clearly too low for meaningful HS mapping in alpine regions. Lee et al. (2008) used a digital mapping camera to cover an area of approximately 2.3 km² with a very high mean ground sampling distance of 0.08 m. The reported mean differences compared to dGNSS measurements are approximately 0.15 m, stressing the great potential of digital photogrammetry for accurate HS mapping. However, no HS mapping has been performed and compared to different reference data sets, covering larger areas (Bühler et al., 2015). Beside satellite products, *digital photography* has also been used to assess the occurrence of avalanches (Edwards et al., 2007; Farinotti et al., 2010) or to statistically analyze the development of the snow cover during the snowmelt season on a mountain crest (Edwards et al., 2007).

Presently, modern digital sensors have been able to overcome the limitations of *analog imagery* through the acquisition of very high mean ground-sampling data (Lee et al., 2008) with 12-bit radiometric resolution (Bühler et al., 2015; Nolan et al., 2015). A more comprehensive investigation of the use of digital photogrammetry for catchment-wide mapping of HS was presented in Bühler et al. (2015).

Studies using stereo-imagery from optoelectronic linescanners incorporating near-IR wavelengths in addition to RGB to map HS are rather novel (Bühler et al., 2014; Bühler et al., 2015). Recently, digital photogrammetry has emerged as a cheaper tool to perform these surveys. Nolan et al. (2015) have evaluated this methodology in three case studies in Alaska and have compared airborne measurements of HS with about 6000 manual measurements. They have found a standard deviation between these two data sets around ± 0.1 m. Bühler et al. (2016) have applied a similar method in the Swiss Alps and estimated HS distribution with a *root mean*

square error (RMSE) of 0.30 m. This technique is, therefore, an accurate solution useful for obtaining distributed information about HS dynamics at meter (or centimeter) resolution (Michele et al., 2016).

Recent advances in digital photogrammetric technology have now made it possible to not only produce accurate HS maps through airborne photogrammetry, but to also do so at larger spatial scales, at a lower cost than LiDAR technology, and without loss of accuracy compared to most other techniques. These advances include improvements in consumer camera sensors, GPS processing techniques (using digital imagery in combination with dGNSS), desktop computational power, and especially, photogrammetric software. This software largely eliminates the need for purpose-built photogrammetric cameras and *inertial motion units* (IMUs), saving a significant amount of money (Nolan et al., 2015). Recent developments in remote sensing offer opportunities to clearly improve the representation of spatial snow cover variability in hydrological modeling (Freudiger et al., 2017).

Table 1.1 gives an overview of the most important strengths and weaknesses of the applied methods for large-scale HS mapping in high-alpine areas based on the experiences gained through the investigation of Bühler et al. (2015).

Table 1.1: Overview of the most important strengths and weaknesses of the applied methods for large-scale snow depth mapping in high-alpine terrain

Method	Strengths	Weaknesses
ALS	- Large coverage	- Expensive
	- Fast measurements	- Costly data processing
	- Spatially continuous	- Need for an airplane
	- High precision	- Expensive device
	- Nadir view	
Airborne photogrammetry	- Very large coverage	- Limited precision
	- Fast measurements	- Costly data processing
	- Spatially continuous	- Need for an airplane
	- Many devices in use	- Expensive device
	- Nadir view	
TLS	- Intermediate coverage	- Oblique view
	- Spatially continuous	- Need for being in the field
	- High precision	- Costly data processing
	- Suitable for steep slopes (>50°)	- Expensive device
GPR	- High precision	- Limited coverage
	- Direct HS measurement	- Transect measurements
		- Extreme terrain inaccessible
		- Need for being in the field
		- Expensive device
Hand plots	- Most economical method	- Very limited coverage
	- Direct HS measurement	- Point measurements
	- No special devices necessary	- Extreme terrain inaccessible
	- Possible in forested areas	- Need for being in the field
dGNSS	- High precision	- Very limited coverage
		- Point measurements
		- Extreme terrain inaccessible
		- Need for being in the field
		- expensive device

1.3 Motivation and objective

1.3.1 Motivation

During the last few years, the use of *unmanned aerial system* (UAS) technology in the context of snow and avalanche studies has often been reported in literature (Adams et al., 2018; Avanzi et al., 2018; Bühler et al., 2016; Bühler et al., 2017; Eckerstorfer et al., 2016; Eker et al., 2019; Harder et al., 2016; Lemke et al., 2007; Lendzioch et al., 2016; Michele et al., 2016; Miziński and Niedzielski, 2017; Redpath et al., 2018; Vander Jagt et al., 2015; Wainwright et al., 2017). Initially, studies in HS mapping investigated the potential and limitations of UAS by using manual HS probing for accuracy assessment. More recently, time series of a UAS are used and compared with other techniques, e.g., airborne sensors such as the ADS100 (Boesch et al., 2016), TLS (Adams et al., 2018; Bühler et al., 2017; Eker et al., 2019), and *very high-resolution* (VHR) tri-stereoscopic Pléiades satellite images (Marti et al., 2016). Different camera sensors recording data in various parts of the electromagnetic spectrum, e.g., visible (350–680 nm) and *near-infrared* (NIR) (>700 and >830 nm), have also been applied (Adams et al., 2018; Bühler et al., 2017; Miziński and Niedzielski, 2017). This study is unique as rather few have used the potential of UAS technology methods to monitor ablation or the melting process (few especially over glaciers) (Bash et al., 2018; Rossini et al., 2018).

Multiple studies show that HS can be accurately mapped by differentiating two surface models (snow-free and snow-covered, respectively). In addition to accurate HS determination, Vander Jagt et al. (2015) show that high-resolution (50 cm) spatially continuous HS maps can be created using a low-cost photogrammetric approach with a UAS. Results indicate the UAS is capable of providing high-accuracy (<10 cm) estimates of HS over a small alpine area (0.7 ha) with snow depths greater than one meter being a fraction of the cost of full-size aerial survey approaches (Vander Jagt et al., 2015). Performing photogrammetric surveys using UASs may, therefore, represent a definitive solution to the problem of mapping HS with fine spatial and temporal resolutions (Michele et al., 2016).

Increasing the spatial resolution of a UAS survey captures additional variability in HS and thus makes it possible to add significant information. It has been observed that HS variability increases with higher sampling resolutions (López-Moreno et al., 2015), but according to Michele et al. (2016), not many data sets are available with a horizontal sampling resolution <1 m (Nolan et al., 2015; Vander Jagt et al., 2015). Consequently, it is not easy to compare this behavior with other analyzes. These dynamics will be the object of future investigations, since, if confirmed, they may define a threshold for sampling resolution when measuring HS during the accumulation season (say 1m resolution) (Michele et al., 2016).

The major disadvantage that accompanies UAS photogrammetry is its limitation in spatial scale compared to airborne LiDAR. However, resolving HS in this way across an entire catchment facilitates robust integration into hydrological models enhanced by validation against

catchment discharge (e.g., from streamflow data) (Redpath et al., 2018). Furthermore, the mapping of HS enables the estimation of snowpack volume across the catchment. Based on in situ measurements of snow density the snowpack mass balance in terms of SWE can also be calculated (Redpath et al., 2018). This enables the quantification of the ablation.

Snow redistribution by wind and avalanches plays a vital role in alpine catchments. A good understanding of snow processes in such catchments is important for both current and future water management, and there is a real need for robust modeling of snowpack in hydrological models (Freudiger et al., 2017). In many hydrological studies, modeling snow redistribution is not considered in the detail it should be, especially because snow redistribution approaches still have limitations. Furthermore, a large gap exists between the know-how and processes implemented in highly detailed physically-based snow models and the widely used bucket-type hydrological models used for water resources and climate change studies (Freudiger et al., 2017). Information earned by snow redistribution modeling with established physically-based models could be used to develop more conceptual approaches for the application in bucket-type models and hence bridge the described gap (Freudiger et al., 2017). According to Freudiger et al. (2017), disregarding snow redistribution in models can lead to the formation of so called *snow towers* (in other words: multi-year accumulation of snow at high altitudes), and an incorrect water balance. Photogrammetric UAS surveys represent an opportunity to capture effective concentration of snow in preferred areas and the complex spatial distribution that results. Although those data sets are temporally limited, the ability to detect such details highlights the potential of this method for improving resolution and the understanding of snow hydrology (Redpath et al., 2018). In particular, such data sets may even offer the opportunity to assess the performance of models forced by remotely sensed data of coarser resolution in estimating SWE from estimates of subpixel fractional SCA (Bair et al., 2016).

Hydrological models are so far not able to describe the distribution of HS in detail, even though information about HS distribution is essential for accurate discharge modeling. Models manage to describe the mean of snow height for a whole catchment but are not able to describe the full distribution with its extreme values in detail. That is where this thesis comes into play.

1.3.2 Objectives: methodology and thesis overlook

Achieved accuracies with UASs are expected to be slightly lower than those using LiDAR technology, but there is an absence of investigations quantifying the achieved accuracy and quality of such DSMs, especially in high-alpine terrain (Bühler et al., 2012). The first objective of this study is to quantify the HS and its spatial distribution at a high alpine site remotely by using a fixed-wing drone. Achieved accuracy and quality of the derived DSMs will be quantified purposefully to improve the aforementioned actual state of knowledge. For validation, numerous manual HS measurements were taken. Another objective is to automatically define SCA from orthophotos and compare the results to satellite products. A

further objective is to retrace the ablation process during summer by determining areas within the catchment that show earliest/latest complete snowmelt to ground. This volume loss will also be quantified.

What makes this study unique and novel in its scientific context is the following:

Based on the generated high-resolution DSMs and proceeding geospatial analysis, such areas of a catchment will be defined and quantified, where abundant snow, and such areas, where there is little snow, i.e. the extreme value ranges, is expected throughout the season. The necessary information represents the own collected HS and derived SCA data. Hence, the assumption is taken that such snowfields in the last UAS survey represent areas where potentially most snow accumulates during the season.

An ever-present question in snow science—whether snow distribution can be linked to topography—will also be addressed. Therefore, the found snow areas and depths are compared to the parameters elevation, slope, aspect, solar radiation, a wind sheltering parameter S_x , and curvature, to test whether a clear linkage can be obtained. A further goal of the study is to use the aforementioned parameters to model both the HS distribution and SCA of the study site based on a snow-free DSM by applying *multiple linear regression* (MLR) models and multiple logistic regression models. Finally, the estimated snow depth distribution for the study site will be presented and compared with the retrieved UASs data.

In other words, this study aims to test the following hypotheses:

- 1. UAS serve to deliver valuable spatiotemporal HS data on a catchment scale for snow-hydrological modeling.**
- 2. Late seasonal HS distribution can be linked to topography.**
- 3. Based on a high-resolution snow-free DSM and retrieved explanatory parameters, both the HS distribution and snow-free/snow-covered areas can be predicted in detail.**
- 4. Satellite data can provide equal information about SCA as recorded high-resolution UAS data in order to model SCA.**
- 5. Based on information about incoming solar radiation, the ablation amount during two consecutive flights can be predicted in detail.**

The overarching intention of this study is to test if HS distributions modeled based on snow-free DSMs with high-resolution can be used as valuable information in hydrological modeling (especially snowmelt modeling), thus improving the often-neglected redistribution of HS.

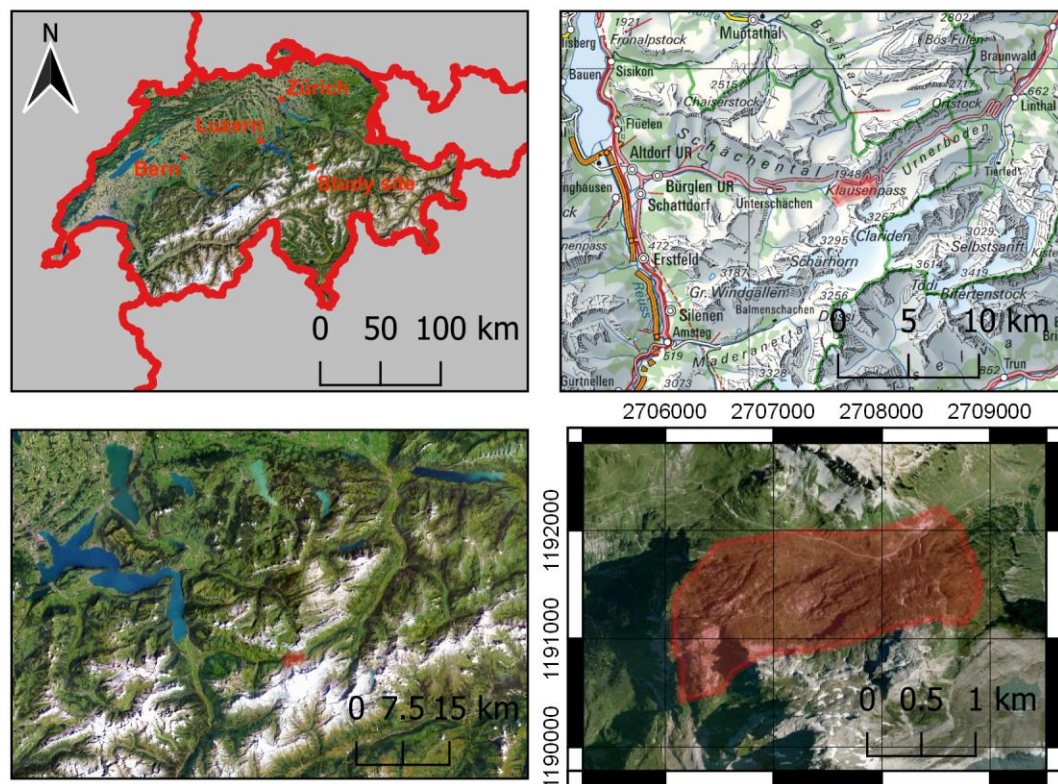
By performing multiple drone flights and applying digital photogrammetry, temporally different orthophotos and DSMs are retrieved that allow for determining the SCA and characterizing (visually) and quantifying its temporal evolution: i.e., the characteristic snowmelt and snow cover depletion pattern of the study site. As additional data source for the period before the first drone flight, satellite images are also analyzed. Once such areas with earlier/late total snowmelt are characterized they will be compared with results from the conducted geospatial analysis applied to the high-resolution DSMs.

Correlations between remaining HS and elevation, slope, aspect, solar radiation, wind exposition, and curvature are investigated, which finally lead to valuable information about which parameters mainly drive the characteristic distribution of HS at the study site. For specific areas within the study site, those parameters explain the corresponding HS.

2 Methods and data

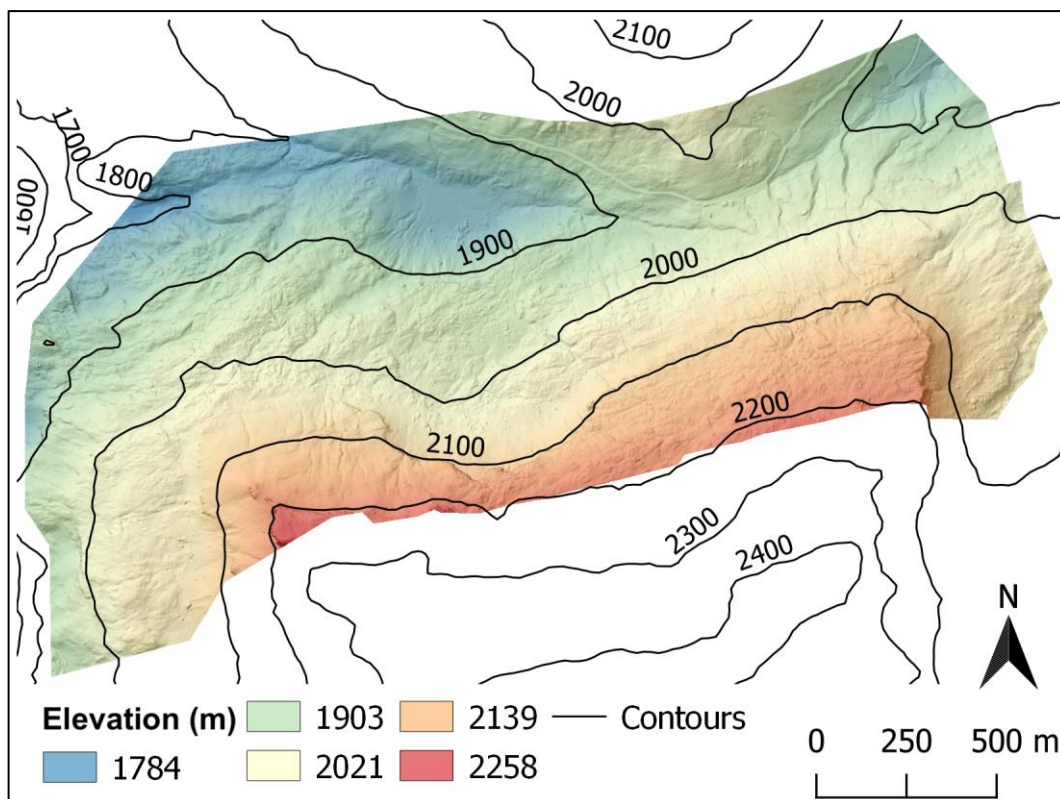
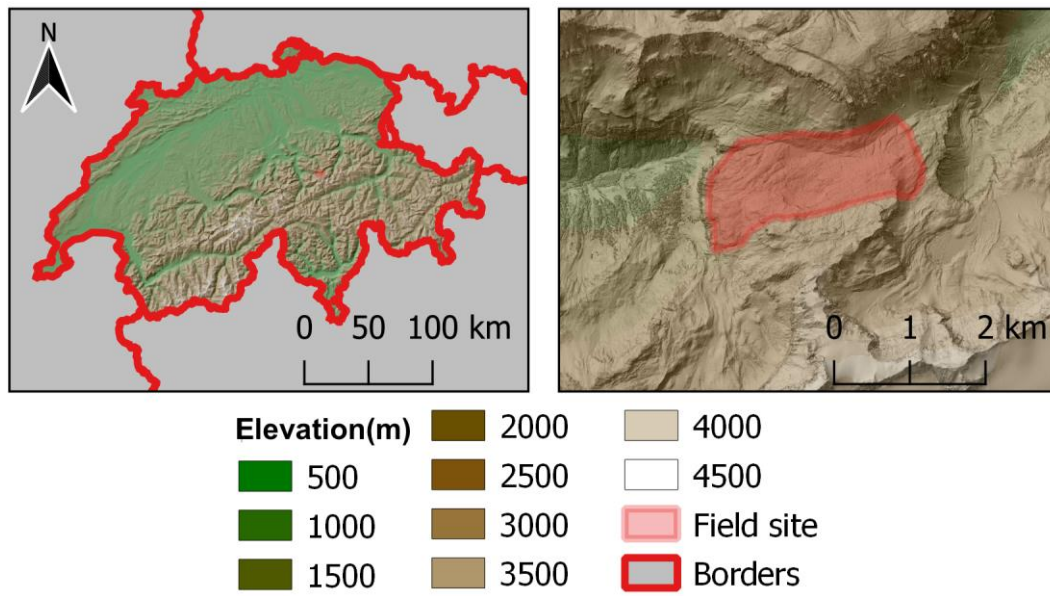
2.1 Study area

This study aims at improving the snow routine of hydrological models of alpine catchments. Although many suitable alpine areas above 2000 m a.s.l. can be found in the Alps, it was mainly due to logistical reasons that the choice fell on the Klausen Pass, located around 45 km southwest of Luzern and connecting the Swiss cantons Uri and Glarus (Map 2.1).



Map 2.1: Location map of the study site within Switzerland

As the hillshade in Map 2.2 illustrates, the mountain pass is surrounded by steep terrain to both north and south and the study site shows a high altitudinal difference with 1784 m at its lowest and 2258 m at its highest location.



Map 2.2: Elevation (m) and hillshade map of the study site within Switzerland.

Figure 2.1 illustrates the hypsometric curve of the study site (derived from the generated snow-free DSM with 10 cm resolution) and its statistics. The elevation range is 474 m.

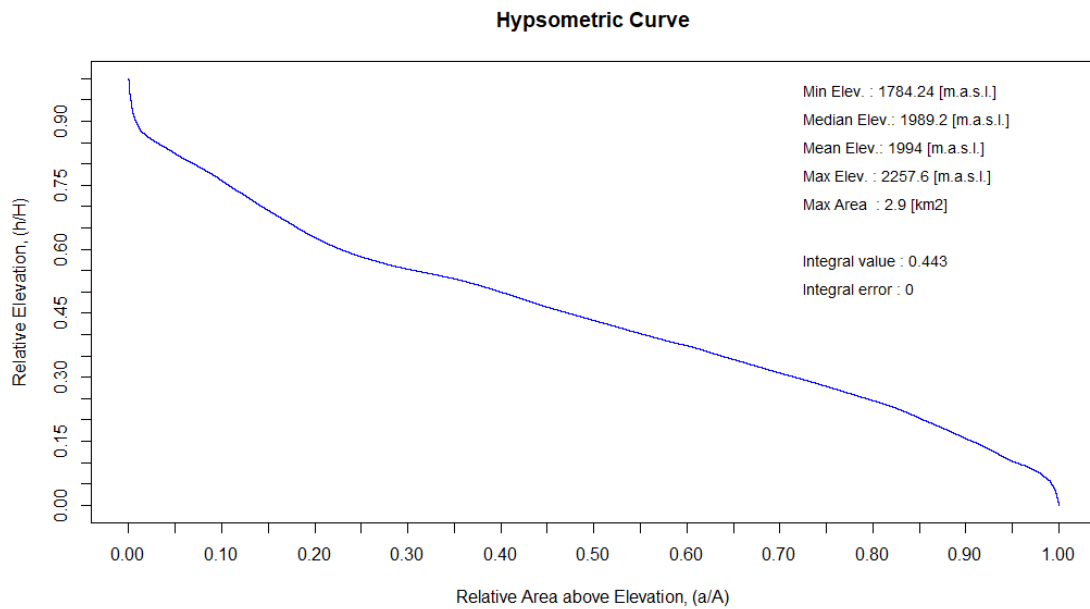
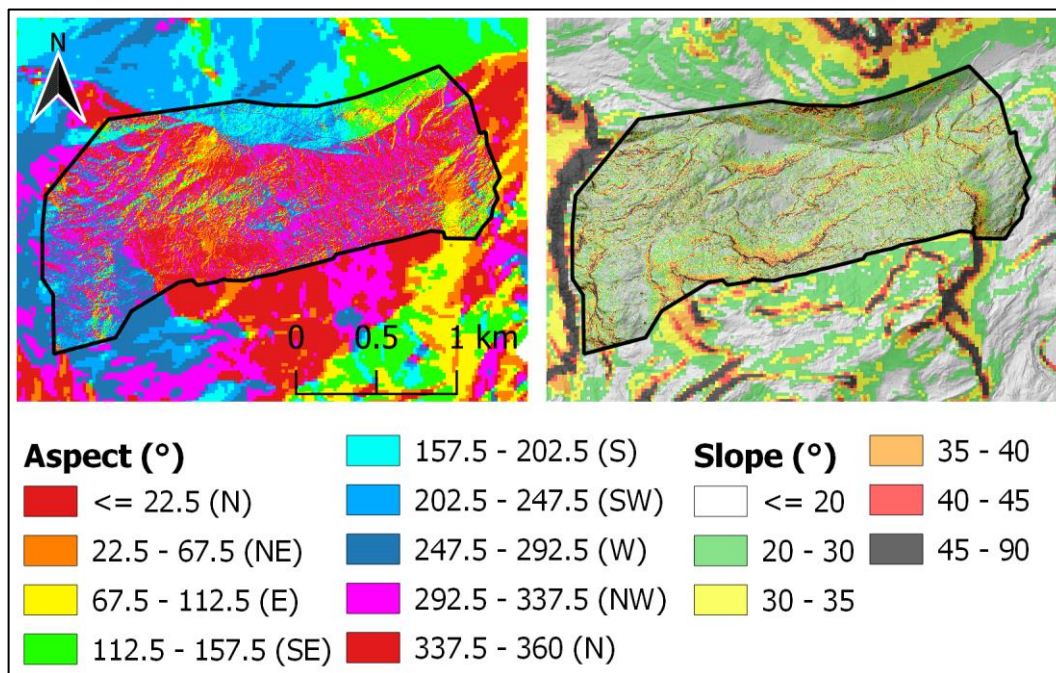


Figure 2.1: Hypsometry and statistics of the study site.

The complete site is located above the tree line and there are no settlements in the area. The major vegetation can be described by small alpine bushes (mainly alpine rose, juniper and erica) and short alpine grass. Steep rocky outcrops can be found in most parts of the study site. The geology is dominated by limestone with high karstification which makes the hydrology really interesting and rather challenging to describe. While the mean exposition is SW (220°) the study site mainly faces towards north (Map 2.3). With slopes exceeding 30 degrees in many areas and a mean of 25 degrees within the test site (Map 2.3), high avalanche activity can be expected, which might be a large factor in local snow redistribution. Because of its location on top of the mountain pass (Figure 2.2) the study site is exposed to strong winds for which reason a high HS variability can be expected especially in this area. In order to realistically capture HS distribution, further factors (e.g., elevation or a wind shelter parameter) should be considered as well. A more detailed analysis can be found in chapter 3.6.



Map 2.3: Aspect and slope within the study site (15 cm resolution) and its surrounding (20 m resolution).



Figure 2.2: View on the study site as seen from Märcher Stöckli (line of sight: South). Besides, the Figure shows the highest mountain around, Clariden (3267 m a.s.l.) and the highest point of the Klausen Pass (1948 m a.s.l.).

At the beginning of the study (June 28th, 2019), below 2000 m elevation it was mainly snow-free and only in depressions snow was remaining. The southerly exposed areas were already totally snow-free. Up to the highest elevation of the study site, the snow cover was not closed anymore and thus can be described as rather patchy with locally big snowfields.

2.2 Data acquisition

2.2.1 UAS surveys

2.2.1.1 Unmanned aerial vehicle

a. Components

For this study, the *eBee Classic* (hereafter *eBee*) was used, an autonomous flying drone system of senseFly®, comprised of the following components (Figure 2.3):

The central body is the core of the eBee and includes all the electronics, actuators and communications hardware on-board the drone. The eBee has two detachable wings, each with two wing struts and two clips to hold it in place within the central body. Winglets add aerodynamic stability to the drone while it is in flight and ailerons are used to control the eBee while in flight. The ailerons are connected to the servomotors within the central body of the drone (servo connection mechanism). The eBee features a built-in camera for taking aerial images stored within the camera compartment. A *Data Link Antenna* is used by the drone to communicate with the *eMotion* software through the USB ground modem. The *Pitot probe* is the sensor used by the eBee to calculate airspeed, wind and altitude. The ground sensor, composed of a high-speed optical sensor and lens assembly, is used to detect the proximity of the ground (senseFly Ltd, 2016).

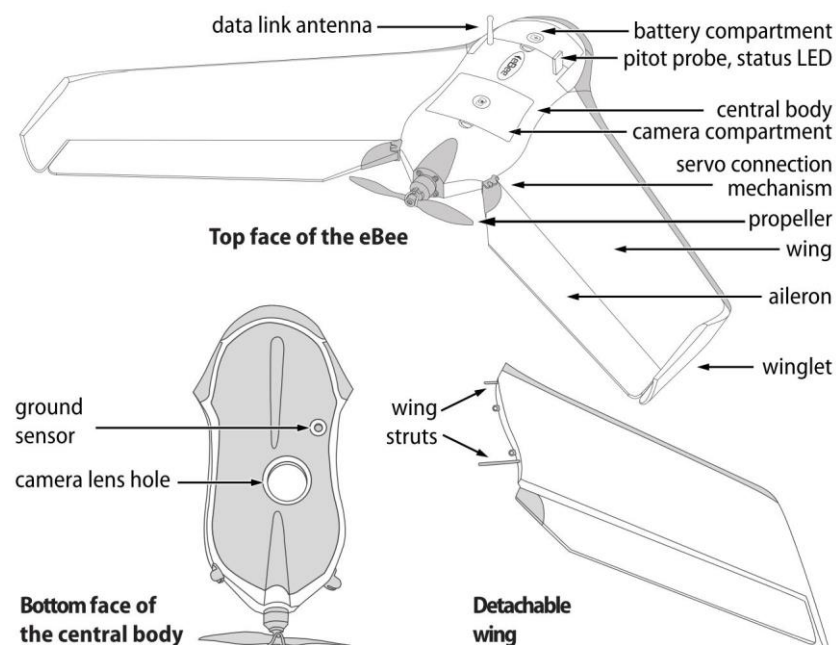


Figure 2.3: Components of the eBee Classic (senseFly Ltd, 2016).

b. Drone Specifications

The eBee (Figure 4.2) has a wingspan size of 96 cm and has an approximate nominal take-off weight of 0.67 kg (with standard camera and 3-cell Lithium-Polymer battery). These features make it suitable for performing photogrammetric flights over limited areas at a very high spatial resolution. It is made from *expandable polypropylene* (EPP) foam, carbon structure and composite parts. According to senseFly the nominal endurance (flight time) is



Figure 2.4: eBee.

about 50 minutes. It has to be mentioned that this can vary greatly depending on external factors such as wind, altitude change and temperature. The propulsion of the eBee is made by an electric brushless motor that enables the device to fly with nominal cruise speed of $40\text{--}90\text{ km h}^{-1}$ ($11\text{--}25\text{ m s}^{-1}$). The eBee resists wind speeds of up to 45 km h^{-1} (12 m s^{-1}). The maximum single flight coverage (on a single battery charge) is 12 km^2 .¹ As communication devices, either a ground modem can be used working on a frequency of 2.4 GHz with a range of approximately 3 km (this can vary greatly depending on external factors such as cruise altitude, presence of obstacles and radio-frequency interference), or remote control working on a frequency of 2.4 GHz with a range of approximately 1 km. The eBee can achieve a GSD (per pixel) down to 1.5 cm. Whereas without ground control points (GCPs) an absolute horizontal accuracy of 1–5 m and a vertical accuracy of 2–5 m can be achieved, with GCPs accuracies of down to 3 cm (horizontal) and 5 cm (vertical) can be achieved. The relative orthomosaic and 3D model accuracy results in 1–3 times the GSD.

Since the eBee continuously analyses data from the onboard autopilot, it is able to perform a pre-planned flight in a fully automated mode. However, the operator can always recover full control of the system. In its body, it incorporates a compact camera Canon IXUS 127 HS (16.1 MP and focal length of 4.3 mm) that captures red, green and blue band imagery as triggered by the autopilot. The sensor is capable of 4608 by 3456 pixels resolution. The full-auto mode includes self-adjustment of aperture, ISO and shutter speed for the given light condition. Depending on flight height, the camera can acquire images at a GSD of some centimeters. The camera lacks a stabilizing gimbal as often seen on multirotor UAVs and upon image capture levels the entire platform and shuts off the motor to minimize vibration, resulting in consistent nadir image orientation (Harder et al., 2016). Images are stored as JPEGs, resulting in 8 bit depth for the three color channels. Images are geotagged with location supplied by the drone's on-board GPS.

¹ The maximum single flight coverage was calculated based on the following test conditions: GSD of 30 cm per pixel, no wind, moderate air temperature of 18 °C, new fully-charged battery, flight altitude of 1000 m above ground and take off at approx. sea level from center of coverage area.

2.2.2 Flight planning

a. Creating a new flight plan

Flights were planned and performed with senseFly's *eMotion* software. *eMotion* is the integrated software package that allows interaction with the eBee. Flights are built using mission blocks. This means that the user has to choose a block (aerial mapping, corridor, etc.), highlight the preferred region to map and define the key settings. *eMotion* then auto-generates the drone's flight plan. *eMotion* has the ability to take into account elevation data to set the altitude of mission waypoints and the resulting flight lines of a mapping mission. This not only improves the resulting ground resolution but also increases mission safety (particularly in uneven terrain) by keeping a more even height between the drone and the ground. To enable a campaign at a field site without internet connection, default *Improved SRTM elevation data* (Shuttle Radar Topography Mission) of *eMotion* has to be downloaded as tiles from senseFly's servers. The data can then be overlaid above the map as a color map (Figure 2.5), making flight planning easier. Once downloaded, elevation tiles are cached and can then be used offline. Once the drone is launched, the wireless connection of *eMotion* with the eBee can be used to track its position, monitor the progress of the mapping flight and send commands (senseFly Ltd, 2016).

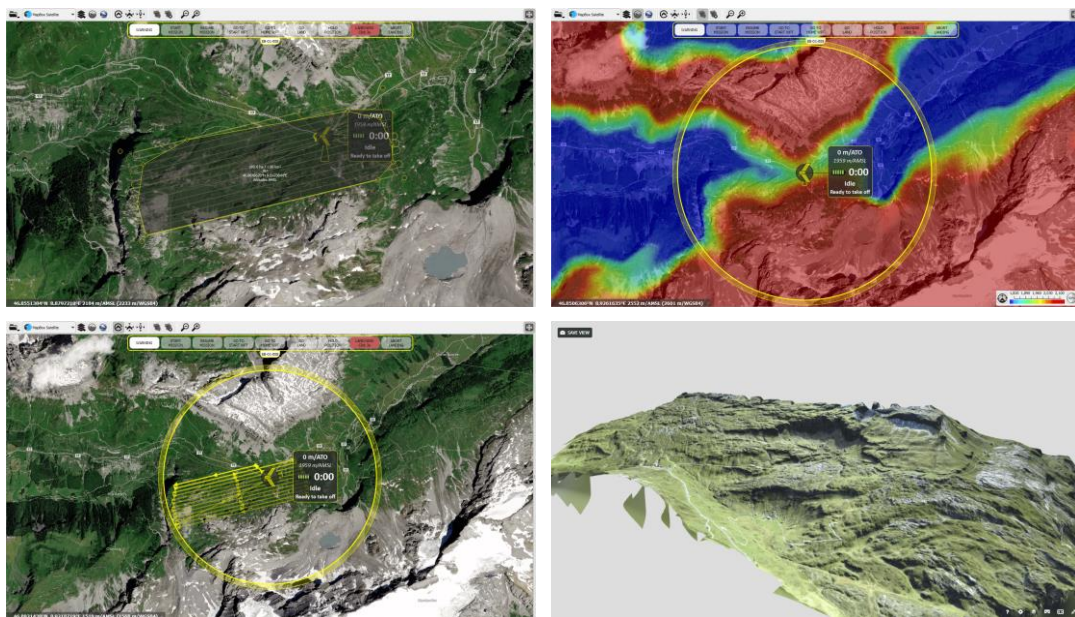


Figure 2.5: Polygonal mission area (top left), DEM (top right) and flight plan in the *eMotion* software (bottom left) and generated snow-free 3D model of study site (bottom right).

b. Mission phase of a flight

As mission area a polygon was defined (parallel to the contour lines to enable higher accuracy), covering an area of 1.86 km². Based on the elevation data, camera specifications, desired GSD and image overlap, eMotion calculated the waypoint navigation (19 waypoints) for the autonomous flight (flight duration of 54 min 45 sec). Since the Lithium Polymer batteries do not endure such a time span, the mission was planned based on a maximum flight time of 30 minutes. This resulted in three single flights each lasting 21 min 52 sec. All flights imaged 13 strips, aligned along the major axis of the study area and representing an estimated total flight distance of 42.4 km. The mean flight lines altitude above elevation data was 227 (7.0 cm px⁻¹) while the min/max flight lines altitude was 162 m (5.0 cm px⁻¹) / 399 m (12.3 cm px⁻¹). The cameras aspect ratio of 4:3 resulted in an image footprint of 230.4 m x 169.9 m. In order to maintain sufficient overlap when covering steep areas, the flight plan incorporated an 80%/70% overlap (longitudinal/lateral).

c. Simulation of a flight

As a final phase of planning, the different flights were simulated to minimize the risk of failure. Here, different scenarios of wind strength and direction were simulated to check the drone's reaction to changing meteorological conditions. Furthermore, by simulating the flights, possible collisions with obstacles (e.g., electrical towers, mountain walls) could be checked and information about position and size of images that will be taken during the flight was gained. In addition, simulations present a great opportunity to familiarize oneself with more advanced functions such as in-flight waypoint editing and camera control without putting the eBee at risk. The flights could be simulated in 3D in GoogleEarthTM.

2.2.2.1 On-site preparation and flight execution

In order to maximize contrast and minimize the risk of corrupted data or damage to the drone, a weather check preceded each flight campaign. Sunny days with minimal cloud coverage and calm wind conditions were preferred, especially to minimize wind speed that can cause staggering of the UAV and consequently produce blurred images. The timing was also considered to minimize shadow effects caused by a low sun angle. High contrast on the RGB images is crucial for discrimination between pixel classes, as well as performing precise orthophoto generation with *structure-from-motion* (SFM) software. In the field, the flight plan had to be uploaded wirelessly to the drone's autopilot. After performing a general inspection, the propeller was mounted on the motor axis and attached with a rubber band. Then, the camera was connected to the eBee and the wings attached. Once the eBee was connected to eMotion and had detected its GPS location, the defined take-off location, start- and home waypoint and

the approaching sector were rechecked. Then, the eBee was hand-launched to map the desired area. During the flight mission, the UAS automatically moves from waypoint to waypoint, however, the eBee was permanently controlled and potential in-flight errors solved (if possible). Only the launch and final landing phases require manual interaction.

In the present study, in total five UAS flight missions with identical planning were carried out, capturing differing states of the snow cover during the ablation period at the study site. The key parameters for the different flight missions are given in Table 2.1.

Table 2.1: Key parameters of the UAS missions. Date, Time (in MESZ), N (number of images/flights), Height (average flight height in m above ground level), FL (Focal Length in mm), ISO, SS (Shutter speed), GSD (Ground sampling distance in cm pix⁻¹), A (area covered in km²), GCPs (Number of GCPs).

Date	Time	Img/Fl.	Height	FL	ISO	SS	GSD	A	GCPs
06/28	8:30-16:30	588/6	238	4.3	100-200	1/200-1250	6.91	3.75	10
07/10	11:00-13:20	634/4	236	4.3	100-200	1/320-1250	6.79	3.77	10
07/17	9:00-10:20	741/4	230	4.3	100-200	1/320-1250	6.66	3.84	10
07/24	9:15-10:15	645/3	239	4.3	100-200	1/320-1250	6.89	3.69	10
09/13	12:40-15:00 16:30-16:45	745/4	238	4.3	100-250	1/320-1250	6.89	3.9	10

Due to the large mission area of 180 hectares, minimum three, sometimes six batteries, each with an estimated flight time between 15–25 min (Table 2.2), were needed to image the whole site. Hence, due to low battery status, the eBee had to be forced to land before finishing the mapping mission and launched again subsequently.

Table 2.2: Meteorological conditions at 12:00 (IMIS measuring station *Alpler Tor* at 2338 m a.s.l. and located 387 m higher and 6.5 km northwest of Klausen Pass) and field notes during flight missions.

Date	HS [cm]	T _a [°C]	v [m s ⁻¹]	Field notes
06/28	173	14.8	4.4	Partly cloudy (40%)
07/10	74	7.0	2.3	Few low clouds moved within study site
07/17	39	9.5	4.3	Windy, instable flight obvious, partly cloudy (40%)
07/24	4	17.2	4.3	Perfect radiation, 0.8–2.6 m s ⁻¹ SW, almost no clouds
09/13	4	13.9	3.1	Sunny, no clouds

Launch and landing location were set beside the highest point of the Klausen Pass at 1960 m a.s.l. and the maximum flight height was 240 m. The UAV was flown according to the local topography and thus parallel to the laterally rising terrain (Figure 2.2), for a total flight time of about 105 minutes. Although snow cover was higher at the start of the campaign, terrain above 2250 was not investigated due to UAV flight limitations, including battery life and line-of-sight

operation and considering that reaching higher elevation in a short time could have entailed significant radial distortion in the acquired pictures (Fugazza et al., 2015).

Alternative test site: the *Griessgletscher* moraine

One flight was conducted at the old moraine of the *Griessgletscher*, where the HILLSCAPE (HILLSlope Chronosequence And Process Evolution) research project took place (Figure 2.6) since it had a bit more snow at the beginning of the campaign, but not significantly more.

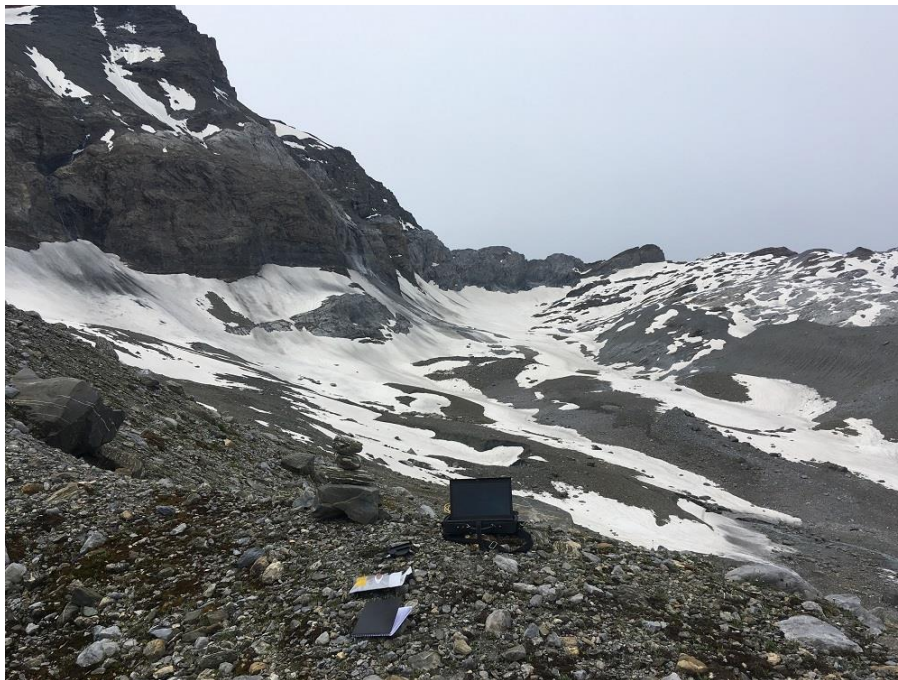


Figure 2.6: Take off location (2300 m a.s.l.) at alternative study site near HILLSCAPE research project field site. Line of sight is east.

The shielding effect of the north face of the tall Chammliberg (3215 m) and Gross Schärhorn (3297 m) caused poor GPS coverage and connection issues between receiver and autopilot. In fact, the conditions were so problematic, that the mission had to be aborted. Additionally, alpine choughs once attacked the drone. Furthermore, landing conditions in the steep, rocky terrain were not optimal. All those factors made the area an inappropriate choice for the planned study campaign of multiple flight missions.

In addition to the presented five UAV missions for image data acquisition, in this study further data was collected.

2.2.3 Differential Global Navigation Satellite System survey

In this study, absolute referencing with detailed observations of the land surface elevation (natural GCPs) was performed to achieve high accuracy of the targeted high resolution DSMs

and orthophotos. The GCPs were measured with a dGNSS with *real-time kinematic* (RTK) positioning technique, since this enhances the precision of position data derived from satellite-based positioning systems. The need for dGNSS measurements becomes clear in this respect, since the geotag errors of the in the present study used non-RTK eBee were ± 5 m (error of GPS Standard Positioning Service) and therefore required GCPs to generate accurate georeferenced data products satisfying the requirements of this study.

There is a special need for correct reference points in photogrammetry, because, particularly in steep terrain, large differences in the elevation value can result from small horizontal shifts (Bühler et al., 2016; Harder et al., 2016). Thus, it was attempted to take the measurements distributed equally over the entire area of interest and all elevation bands. As natural GCPs only such locations with distinct terrain features that are not covered by snow came into consideration.

The first GNSS survey, utilizing a Leica GS20 as a base station, took place July 10th, 2019, but could not be realized since no network connection to a station of the *Automated GNSS Network for Switzerland* (AGNES) could be initialized. The AGNES stations enable further densifications using classical baseline calculations in post-processing or in real-time using the *swipos* positioning service (German: *Schweizer Positionierungsdienst des Bundesamts für Landestopographie*). Unfortunately, the provided GNSS only works within the German satellite reference service SAPOS (German: *Satellitenpositionierungsdienst der deutschen Landesvermessung*). Therefore, September 12th, 2019 (10:30–18:15 MESZ), with a Trimble R7 GPS Receiver (and Trimble TSC2 Controller) (Figure 2.7) ten points (Map 2.4; Table 2.3) were acquired, placing the antenna on a tripod over beforehand selected photo-identifiable targets (Figure 2.7). Because of poor network coverage, RTK could not always be performed. For that reason, static longer-term point measurements (without reference station) were regarded as an alternative. In that case, the receiver takes about eight minutes to correctly store the point one wants to measure. The controller established connection with the AGNES station *OALP* (E = 2'694'527.607 N = 1'168'390.748, H = 2090.349 (ell.)) and coordinates were taken in the Swiss coordinate system CH1903+/LV95. The measurements were stored on the controller and subsequently post-processed as correct reference information for photogrammetry.

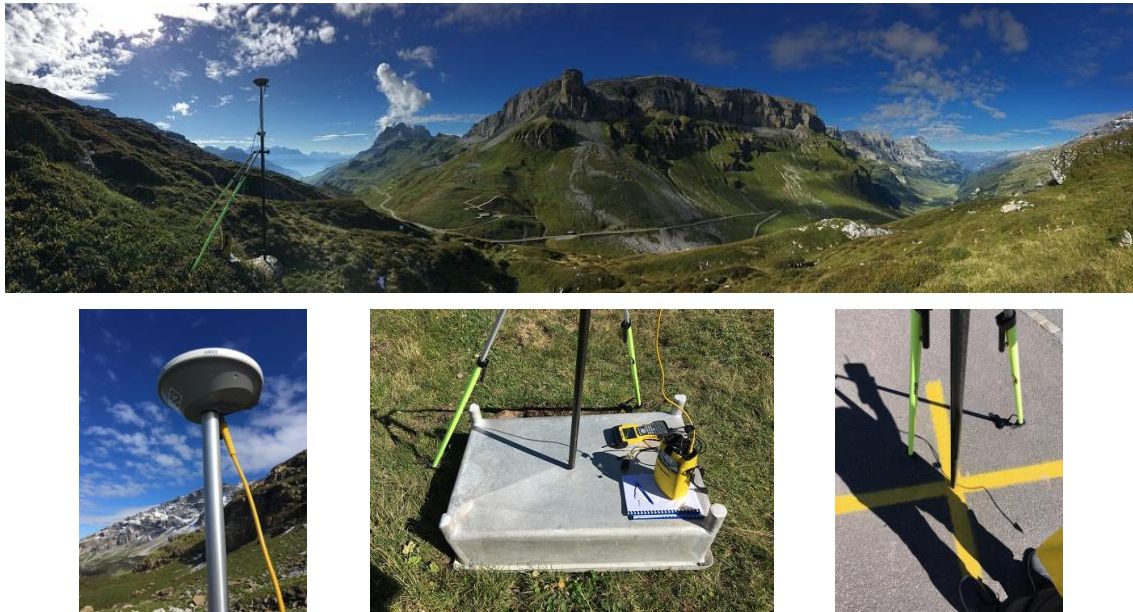
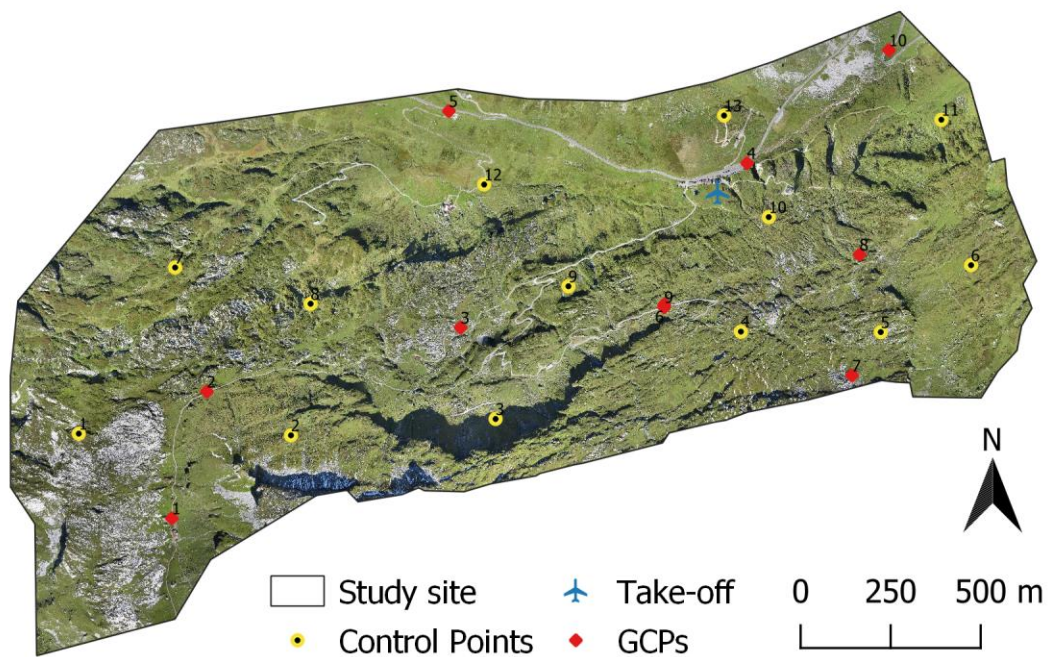


Figure 2.7: Illustration of dGNSS measurement setup with Trimble R7 GPS antenna and receiver fixed on ranging rod and ranging pole tripod (top). Dual-frequency rover antenna (lower left). Receiver and controller (lower middle). Example of photo-identifiable targets as GCP (lower middle & right).



Map 2.4: Location of GNSS measurements (GCPs), control points and take-off & landing location at the Klausen Pass field site.

Table 2.3: Corrected dGNSS measurements from September 12th, 2019 with discrimination of measurement technique.

Point ID	Easting	Northing	Elevation [m]	technique
1	2706520.868	1190805.416	2054.781	RTK
2	2706618.087	1191157.473	2049.858	RTK
3	2707322.874	1191335.104	1966.799	static
4	2708118.156	1191792.086	1942.388	static
5	2707290.204	1191936.895	1898.258	RTK
6	2707887.813	1191391.784	2058.691	RTK
7	2708409.704	1191202.059	2194.979	RTK
8	2708430.553	1191537.942	2081.468	RTK
9	2707888.271	1191399.058	2057.197	RTK
10	2708512.551	1192106.011	1866.703	static

According to the producer (Trimble Navigation Limited, 2019b), the device allows for measurements with a positioning performance of 3 mm + 0.1 ppm RMS (horizontal) and 3.5 mm + 0.4 ppm RMS (vertical) in high precision static GNSS surveying, and 8 mm + 0.5 ppm RMS (horizontal) and 15 mm + 0.5 ppm RMS (vertical) in real time kinematic surveying. The error that can result from Agisoft Photoscan in 3D processing therefore minimizes significantly.

By identifying the ten surveyed GCPs of September 12th, 2019, in the image data of all surveys relative co-registration of the five DSMs was made. According to Bühler et al. (2016), GCPs would not be necessary if a very accurate (better than 0.05 m) GNSS/IMU system was available directly on the UAS. First UAS products with such high-accuracy GNSS sensors are already available on the market. However, Harder et al. (2016) clarify that the achieved orientation accuracy is not sufficient for HS mapping without GCP measurements.

Table 2.4: Positioning specifications for the Trimble R7 (Trimble Navigation Limited, 2019a).

Positioning	Mode	Horizontal Acc. (RMS)	Vertical Acc. (RMS)
RTK (OTF)	Synchronized	1 cm + 1 ppm	2 cm + 1 ppm
	Low Latency	2 cm + 2 ppm (x baseline length) ^a	3 cm + 2 ppm (x baseline length) ^b
L1 C/A Code Phase	Synchronized/Low Latency	0.25 m + 1 ppm RMS	0.50 + 1 ppm RMS
Static/FastStatic	N/A	5 mm + 0.5 ppm	5 mm + 1 ppm
WAAS	N/A	Less than 5 m	Less than 5 m

^adepends on radio link latency.

^b3D RMS values depend on WAAS system performance.

2.2.4 Satellite imagery

2.2.4.1 Extracting SCA information from satellite data

Prior to the UAS survey, satellite data (SENTINEL-2) was gathered from the Copernicus Open Access Hub (2019) of the European Space Agency (ESA) and post-processed to gain initial insights into the extent of the snow cover as well as the evolution of the snow melt process during the ablation season. SENTINEL-2 is a European wide-swath, high-resolution, multi-spectral imaging mission and carries an optical instrument payload that samples 13 spectral bands: four bands at 10 m, six bands at 20 m and three bands at 60 m spatial resolution (Table 2.5). The twin satellites of SENTINEL-2 provide continuity of SPOT and LANDSAT-type image data, contribute to ongoing multispectral observations and benefit Copernicus services and applications such as land management, agriculture and forestry, disaster control, humanitarian relief operations, risk mapping and security concerns (ESA, 2019).

Table 2.5: Spectral bands for the SENTINEL-2A sensor (according to ESA).

Band number	Spectral region	Central wavelength [nm]	Bandwidth [nm]	Spatial resolution [m]
1	Coastal aerosol	442.7	21	60
2	Blue	492.4	66	10
3	Green peak	559.8	36	10
4	Red	664.6	31	10
5	Vegetation Red edge	704.1	15	20
6	Vegetation Red edge	740.5	15	20
7	Vegetation Red edge	782.8	20	20
8	NIR	832.8	106	10
8A	NIR _{narrow}	864.7	21	20
9	Water vapour	945.1	20	60
10	SWIR - Cirrus	1373.5	31	60
11	SWIR	1613.7	91	20
12	SWIR	2202.4	175	20

The images used in this study were already corrected surface reflectance images (Level 2A) (Table 2.6).

Table 2.6: SENTINEL-2 product types.

Name	High-Level Description	Production & Distribution	Data Volume
Level-1C	Top-Of-Atmosphere reflectances in cartographic geometry	Systematic generation and online distribution	~600 MB (each 100km x 100km ²)
Level-2A	Bottom-Of-Atmosphere reflectances in cartographic geometry	Systematic and on-User side (using Sentinel-2 Toolbox)	~800 MB (each 100km x 100km ²)

The satellite data was used to calculate the *Normalized Difference Snow Index* (NDSI) for days without cloud cover at the test site, before, during and after the UAS missions. Potential cloudy pixels were excluded from the snow cover calculation. The NDSI is a ratio of two bands: one in the *Visible and Infrared* (VIR) (Band 3) and one in the *Short-wavelength infrared* (SWIR) (Band 11). The NDSI takes advantage of spectral differences of snow in SWIR and visible spectral Bands. Snow absorbs in the SWIR (1.6 μm), but reflects in the VIR, whereas clouds are generally reflective in these Bands. Since snow absorbs in the SWIR it appears darker than clouds enabling an effective differentiation. In only visible wavelengths, snow appears as bright as clouds making a differentiation difficult. The NDSI ranges from -1 to 1.

$$NDSI = \frac{Band3 - Band11}{Band3 + Band11} \quad (1)$$

Pixels with a NDSI value under 0.20 are considered *no snow* pixels while pixels with NDSI values exceeding 0.42 are considered *snow* pixels. Pixels with NDSI values between 0.2 and 0.42 are considered potentially snowy (ESA, 2019).

Since a NDSI of 0.42 is a common threshold value in literature and potentially cloudy pixels are excluded, values above 0.42 were considered snow pixels. The satellite data thus allowed to quantify the snow cover extend for days with potentially no cloud cover and could be verified by the 1 m resolution own retrieved UAS data (chapter 3.4).

The analyzed satellite data shows the stepwise depletion of the snow cover at the field site from March to August and the subsequent autumn snowfalls. The image of June 17th, 2019 was of special interest and considered a good example for areas where the full snowpack depleted, and ground becomes visible. Hence, those snow-free areas are considered such within the field site, where not only potentially the least snow accumulates but also several factors, such as solar radiation input and others (especially terrain characteristics), cause the snowpack to fully melt to ground the earliest.

To compare the calculated snow extent from the high-resolution images taken with the UAS with the medium-resolution of the satellite, cloud-free data of SENTINEL-2 overpass for the specific UAV mission days was processed if possible, otherwise from the next closest day. The NDSI maps were later used for statistical analysis. Snow and snow-free pixels were linked to the specific parameters of the terrain (resampled to 1 and 10 m) to test if a prediction of snow cover was possible (chapter 3.6).

2.2.5 Manual snow depth measurements

In order to validate the computed HS, manual measurements were taken in the field during the first, second, third and fourth UAS survey with a marked avalanche probe of 2.4 m length (Figure 2.8) simultaneously. The reference measurements were mostly performed in the middle of the lasting snow patches. Snowfields of especially large extent were probed by more than one measurement. The probing proved difficult since the snow was really compact and dense, and in many places melt-freeze crusts from the last winter season built a sometimes impermeable layer. Acquiring much manual HS data was particularly challenging due to the really steep terrain and limit of human power. Therefore, the number of performed measurements distributed over the entire study



Figure 2.8: Scale, tube, shovel and avalanche probe.

area is close to the possible maximum that can be obtained by one person in a day. For some locations the probe was unfortunately way too short to measure the full HS. Nevertheless, specific care was taken to guarantee that only those measurements were taken for validation where the contact to ground could be felt. However, the measurements were still defective which is in line with the investigation by Prokop et al. (2008) who found that such HS measurements are effected in the range of 0.05–0.10 m. Measurements, especially in areas with many stones or in plateaus with high karstification showed a high local variability in HS. Especially dangerous at snow fields that were eroded by a stream. In total, more than 250 measurements were performed. For each point the coordinates were recorded with a Garmin GPSMAP 76CSx (with an expected accuracy better than 10 m) as approximate reference. However, acquiring the coordinates with a dGNSS at each HS measurement location would allow for direct comparison of UAS derived and manual HS values but go beyond the scope of the thesis.

2.2.6 Manual snow density measurements

Calculating SWE and ablation rates from HS data requires average snow cover density estimations. Many studies have found that the spatial variability of density is relatively small in comparison to HS (Dickinson and Whiteley, 1972; Marchand and Killington, 2004; Mizukami and Perica, 2008; Pomeroy and Gray, 1995). Consequently, it is common to estimate areal SWE with a small number of representative density measurements and a high number of HS data (Elder et al., 1998; Jonas et al., 2009; Rovaneck et al., 1996). Thus, in this study, SWE was calculated based on a small number of well-selected density measurements. Although snow density and especially its depth-average is often assumed to be controlled by a small number of topographical and meteorological parameters which are total HS, elevation, solar radiation, climatic region and vegetation patterns (Anderton et al., 2004; Jonas et al., 2009), this study does not consider snow density in such detail. Because of the limited extent of the investigation area, the present investigation focusses on the conducted measurements and assumes those to represent the average density within the investigated area.

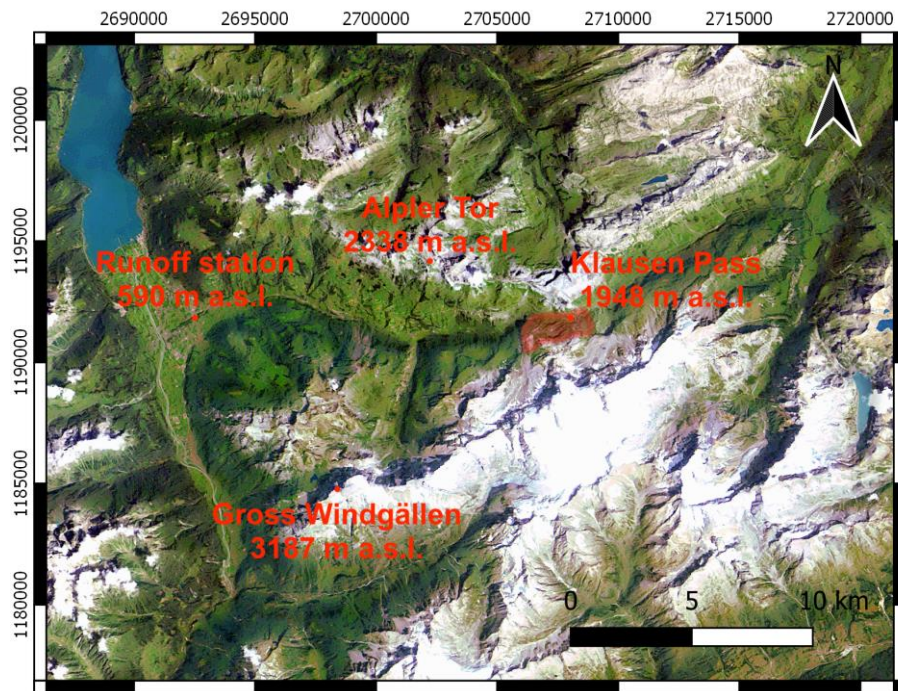
Snow density measurements were conducted at each flight date. The measurements were taken at specific elevations to test for variability. As tools, snow probe, shovel, scale and a tube with a cross-sectional area of 24.6 cm^2 were used. For each measurement, a full snow pit was dug to the ground first, subsequently HS measured and finally the column excavated with the tube (Figure 2.8). Proceeding this way ensured that no snow was lost when extracting the core from the snow cover and no undesired manual compression of the snow took place. Moreover, this procedure ensures most accurate simultaneous HS measures on the same spot. The snow density was always determined for the whole HS and not for several layers. The measuring sites varied in exposition, slope, elevation and snow depth.

2.2.7 Meteorological data

To receive information about the start and end of accumulation and ablation of the snowpack and the annual and seasonal dominant wind direction to calculate the terrain (wind shelter) parameter S_x , station data from the WSL Institute for Snow and Avalanche Research SLF was used. While the information about HS, new snow and air temperature comes from the *IMIS* (Intercantonal Measurement and Information System) snow station *Alpler Tor* (2'702'186.032, 1'194'253.055, 2338 m a.s.l.), located 6.3 km NW and 385 m higher, the wind data comes from the IMIS wind station *Gross Windgällen* (2'698'728.600, 1'184'823.850, 3187 m a.s.l.), located 11.6 km SW and 1217 m higher.

The snow and wind stations of the IMIS network are usually situated close to each other and measure the key weather data required for assessing the avalanche danger in concert. Snow stations are erected in flat terrain that is protected from the wind. The snowpack model SNOWPACK calculates the layering and properties of the snowpack throughout the winter for

each of the IMIS snow stations. The results are not only essential for determining the amount of fresh snow, but also give an indication of the bonding of the snowpack, the formation of surface hoar and snowdrift accumulations, and of increasing moisture throughout the snowpack, which is a symptom of imminent wet-snow avalanches. Like most IMIS stations, the station *Alpler Tor* is located in the vicinity of starting zones of potentially destructive avalanches, and provides those who are responsible locally for public safety in settlements and on the roads with essential information (WSL Institute for Snow and Avalanche Research SLF, 2019).



Map 2.5: Landsat Mosaic 25 m with location of IMIS stations and runoff station in relation to the Klausen Pass study site (Scale: 1:250,000).

2.3 Data processing

2.3.1 Processing image data

Post-processing included all working steps to obtain the high-resolution DSMs and orthophotos from the retrieved UAS imagery. After each mission, the flight manager of *eMotion* was used to geotag the gained raw images with information from the corresponding drone flight log files. Without geoinformation, high-resolution photogrammetric processing would not be possible. As software for processing Agisoft PhotoScan Professional was used, an advanced image-based 3D modeling solution aimed at creating professional quality 3D content from still images (Agisoft LLC, 2018), using a SfM algorithm. Further details about the processing procedure can be found in the PhotoScan user manual (Agisoft LLC, 2018), as well as at the Agisoft website (Agisoft, 2019). PhotoScan enables the exterior orientation of large data sets, by performing the image relative orientation and camera self-calibration, in an arbitrary

reference system, which is often obtained using a minimum constraint coming from the approximate orientation provided by telemetry (Michele et al., 2016).

SfM software and traditional photogrammetric-processing software triangulate the positions of points on the ground that have been imaged multiple times in overlapping photographs to create a so called point cloud (collection of data points (X, Y, Z) defining the shape of the measured surface). Subsequently, the point cloud can be gridded into a DSM or an orthometrically corrected image mosaic (Gibbs et al., 2015). In the following, the procedure of images processing and 3D model construction will be explained in detail. The number of photos that can be processed by PhotoScan depends on the available RAM and reconstruction parameters used. Therefore, processing had to be done on a computationally strong computer, in this case a Microsoft Windows 8 64 bit, Intel® Core™ i7–4930K CPU @ 3.40GHz processor with 64 GB of RAM. As GPU a Nvidia GeForce GTX 780 Ti was used.

Stage 1: Image matching and bundle block adjustment

After importing all images of a survey with their corresponding X, Y, Z coordinates (WGS94 + EGM96), image alignment was conducted. Here, PhotoScan searches for common points on the block of images and matches them. During this step, PhotoScan also finds the position of the camera for each image and defines the camera calibration parameters. The software then extracts topographic points (which represent a cloud of points) and rejects outliers from the cloud for each survey to avoid reconstruction errors.

...short information about camera orientation and lens distortion

Before a DSM can be generated, two types of unknowns, exterior and interior orientation of the camera, must be determined. In this study, images were shot with a frame camera (Canon IXUS 127 HS). For successful estimation of camera orientation parameters, thus the information on appropriate focal length (in pix) is required. To calculate focal length value in pixel, it is enough to know focal length in mm (here: 4.3) along with sensor pixel size in mm (here: 0.0013 x 0.0013). Exterior orientations refer to the position and tilt of the images and include six unknowns: X, Y, Z (point coordinates in the local camera coordinate system), yaw, pitch, and roll (tilt of the camera, Figure 2.9). While many photogrammetric cameras are equipped onboard with both GPS and inertial measurement unit (IMU), the camera model used in this study is only provided with the first, and thus pitch, yaw and roll need to be estimated by the software. Interior orientations refer to the specifics of the camera and lens: focal length, sensor dimensions, pixel pitch of the sensor, lens distortions, and principle point. These result in about ten unknown parameters, depending on the lens distortion model. The distortion of the lens used to capture the images should be well simulated with the Brown's distortion model because otherwise it is most unlikely that processing results will be accurate (Agisoft LLC, 2018).

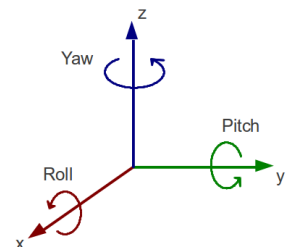


Figure 2.9: Tilt of cam.
(GitHub, Inc, 2019).

Camera orientation and calibration parameters:

- X, Y, Z : point coordinates in the local camera coordinate system
- u, v : projected point coordinates in the image coordinate system (in pixels)
- f_x, f_y : focal length in x- and y-dimensions measured (in pixels)
- c_x, c_y : principal point offset, i.e. coordinates of lens optical axis interception with sensor plane
- b_1, b_2 : affinity and non-orthogonality (skew) coefficients
- k_1, k_2, k_3, k_4 : radial distortion coefficients
- p_1, p_2, p_3, p_4 : tangential distortion coefficients
- w, h : image width and height in pixels

Equations used to project a point in the local camera coordinate system to the image plane for frame camera models such as the Canon IXUS 127 HS:

- $x = X / Z$
- $y = Y / Z$
- $r = \sqrt{x^2 + y^2}$
- $x' = x(1 + k_1r^2 + k_2r^4 + k_3r^6 + k_4r^8) + (p_1(r^2 + 2x^2) + 2p_2xy)(1 + p_3r^2 + p_4r^4)$
- $y' = y(1 + k_1r^2 + k_2r^4 + k_3r^6 + k_4r^8) + (p_2(r^2 + 2y^2) + 2p_1xy)(1 + p_3r^2 + p_4r^4)$
- $u = w * 0.5 + cx + x'f + x'b_1 + y'b_2$
- $v = h * 0.5 + cy + y'f$

As a result of image alignment, a sparse point cloud and a set of camera positions are formed.

Stage 2: Inclusion of GCPs and sparse geometry reconstruction

Based on the sparse point cloud, geometry (i.e., a 3D polygonal mesh representing the object surface) is reconstructed which enables guided marker placement. Markers represent the surveyed GCPs. As next step, the coordinate system is set (here: CH1903+/LV95) and coordinates of the GCPs (here: CH1903+/LV95) are imported. The advantage of guided marker placement is that PhotoScan automatically projects the corresponding ray onto the model surface and calculates marker projections on the rest of the photos where the marker is visible. This reduces the chance of incorrect marker placement. However, sometimes markers are projected not that accurate demanding manual replacement. The subsequent use of surveyed GCPs allows translating and rotating the photogrammetric blocks in a specific coordinate reference system (here: CH1903+/LV95) The bundle adjustment is recalculated and fine-tuned in this step making absolute accuracy of the DSM and orthophoto possible (e.g., no anomaly of 50 m in height due to the different reference ellipsoids of WGS84 and LV95).

Stage 3: Optimization of camera alignment

After correct *marker placement*, the camera alignment was optimized to achieve a higher accuracy of the model (lower geo-referencing errors). The optimization procedure was run based on markers data only since GCPs coordinates are measured with significantly higher accuracy compared to the GPS data of the UAS that indicates the camera positions. Thus, more precise optimization results could be achieved. In addition, GCPs and camera coordinates were measured in different coordinate systems, which had complicated the optimization.

Stage 4: Point cloud generation based on imported camera data

Based on the initial precise GCP and camera data a 3D reconstruction job was realized. Based on the estimated camera positions and images themselves, PhotoScan calculates depth information for each camera to be combined into a single dense point cloud. To obtain more detailed and accurate geometry, *high* reconstruction quality, requiring longer processing time, was selected. Since the geometry of the scene to be reconstructed (here: high alpine field site) is complex with numerous small details, *mild* filtering mode was chosen for important features not to be sorted out in the 3D reconstruction process.

Stage 5: Generation and exporting of DSMs and orthophotos

A *DEM* (Digital elevation model) represents a surface model as a regular grid of height values. Since most accurate results are calculated based on dense point cloud data the DEMs of this study were rasterized from dense point clouds. From the point clouds of the different surveys, DSMs of different ground sampling resolutions were extracted by generating a polygonal mesh model from the cloud data through interpolation. Enabling interpolation forces PhotoScan to calculate the DEM for all areas of the scene that are visible on at least one image. Exact relative geo-referencing between the different DSMs is essential for correct HS calculation (snow-covered DSM minus snow-free DSM). Even small shifts in x and y can lead to large differences in z direction on steep terrain (Bühler et al., 2016).

First, *relative referencing* with natural GCPs that were well visible in the snow-free and the snow-covered imagery was conducted, since no artificial GCPs were measured with differential GNSS allowing for *absolute referencing*. Here, the first DSM was generated without GCPs. From the product, well distributed over the area of interest and its elevations, 30 markers with X , Y , Z coordinates were taken from outstanding snow-free terrain features. Those markers were used for relative geo-referencing of the following DSMs. The results turned out to be not accurate enough (especially vertically) and thus inappropriate for HS calculation. Possible errors could have been an excessive demand of the Agisoft software due to a too large number of GCPs and wrong marker placement, for instance. Since GCPs were measured with a dGNSS in the later course of the study, enabling both relative and absolute accuracy of the DSMs, only

those results will be presented: For each of the five UAS surveys the same ten GCPs measured with differential GPS were used for absolute referencing. The DSMs were projected in the same resolution (i.e. 15 cm pix^{-1}) in the Swiss coordinate system CH1903+/LV95 for a desired region (Table 2.7) to reach an accurate overlap of the raster cells.

Table 2.7: Swiss coordinates (CH1903+/LV95) of the extent of the generated DSMs and orthophotos for the 5 UAS surveys (x = East, y = North).

	x	y
min	1'190'188.523	2'705'507.832
max	1'192'588.222	2'709'475.632

Orthophotos were generated based on the DEM as type of surface data for the orthorectified imagery to be projected onto. Generation of the orthophotos was done according to the settings for the DEM generation.

The abovementioned workflow operations with the desired processing parameters were applied to the different chunks and performed as batch process ascertaining that all surveys were processed under equal settings. Due to the excessive calculations on large data, batch processing was crucial (processing times varied from nine to twelve hours). Generated DSMs and orthophotos are analyzed in chapter 3.

2.4 Geospatial analysis

With the digital photogrammetry products, further analysis was conducted to test the proposed hypotheses.

2.4.1 Quantification of SCA

2.4.1.1 Automatic classification

To quantify the SCA of the single surveys, an automatic classification of the snow-covered and snow-free areas was striven for. Furthermore, a correct snow mask was considered very useful to validate the retrieved HS maps by the subtraction of the snow-free DSM from the snow-covered since it gives clear information about where snow is present and where not. The target of automatic classification of the RGB orthophotos with discrimination of snow-covered and snow-free areas turned out not to be achievable but the carried-out techniques in the open source software *QGIS* will be mentioned briefly.

Initially, the unsupervised *k-means clustering* procedure was applied to the RGB orthophoto to produce a dichotomous snow extent numerical map. The clustering algorithm divides observations into k clusters and can be described as type of unsupervised machine learning which aims to find homogeneous subgroups such that objects in the same group are more similar to each other than to others. The clustering was run to detect both *snow* and *no snow* raster cells (two classes) and the identification of *snow* and *no snow* raster cells with possible artefact detection (three or more classes). The artefacts may be of different origins, e.g., caused by SfM failures or shadows. This procedure has proven to be appropriate in the study of Niedzielski et al. (2018), where a three-cluster classification detected shadows on continuous snow cover, but failed to identify shadows when snow cover was discontinuous. Also, the RGB snow extent maps produced with the *k-means clustering* were found to agree well with the human digitized analogues.²

In this study, the resulting raster maps with each cell representing one of the k possible values showed certain inaccuracies. Although the classification correctly discriminated snow-covered from snow-free terrain in most places, the clustering classified erroneously shadowed snow areas as *snow-free* and led to an overestimation of SCA in total, since most karst areas were classified as *snow* while dirty snow was classified as *no snow*. Different cloud cover and sunlight could be a potential explanation for the failure of the classification but Niedzielski et al. (2018) report that uneven lighting conditions had no impact on snow detection. Altogether, the crucial issue of this study site is that karst is present. Albeit karst is generally grey, it features parts that are almost white with RGB values towards 255. However, most of those features occur on areas where the sunlight reflects in an unfavorable angle during image capture. For this reason, a logic discrimination of snow and no snow terrain for the whole study area was impossible because of the local similarity of karst and snow. In retrospect, it is highly recommended to perform the UAS surveys with NIR cameras enabling the discrimination of snow-covered and snow-free terrain (chapter 4). This is because snow absorbs more energy in the NIR part ($\lambda \approx 760\text{--}2500\text{ nm}$) of the electromagnetic spectrum than in the visible part ($\lambda \approx 400\text{--}700\text{ nm}$) (Bühler et al., 2015).

As further method, a *semi-automatic classification* was tested. Here within the RGB image training input data was defined. This means, multiple polygons (regions of interest) were drawn and assigned to different classes and subclasses (bright snow, dark snow, bright karst, dark karst, vegetation, roads, etc.) representing the specific spectral signature of each class. Afterwards, the classification was run. Also here, the similarity of karst and snow pixels could not be separated. While the semi-automatic classification was not successful in the RGB, it showed good results with multispectral data from SENTINEL-2 bands. The resulting binary

² For further information about the *k-means clustering* procedure and its concept I refer to Zhang, van der Werff et al. (2012); Zhang, Skjetne et al. (2012); Niedzielski et al. (2018) and Julitta et al. (2014).

information raster 0/1 (no snow/snow) were only further used for logistic regression on 10 m resolution since the satellite products are not available in lower resolution.

Because Eker et al. (2019) received good results in mapping the areal extent of the snow cover with this technique, the snow cover was estimated by classifying snow-covered and snow-free areas based on a *threshold value* applied to the *blue band* information of the orthophotos. However, their study included absence of vegetation or tall objects playing a role in shadow effect and flat topography, the latter condition was not met in this study. The technique itself is the easiest and least robust in snow cover classification since band ratios, supervised- and unsupervised classifications generally provide more successful results by minimizing incorrect pixel classifications. The SCA was estimated multiple times by changing the threshold of the blue band but just as for the other tried techniques, karst could not be discriminated clearly from snow and thus the results also appeared to be inappropriate for further analysis, as Figure 2.10 clarifies.

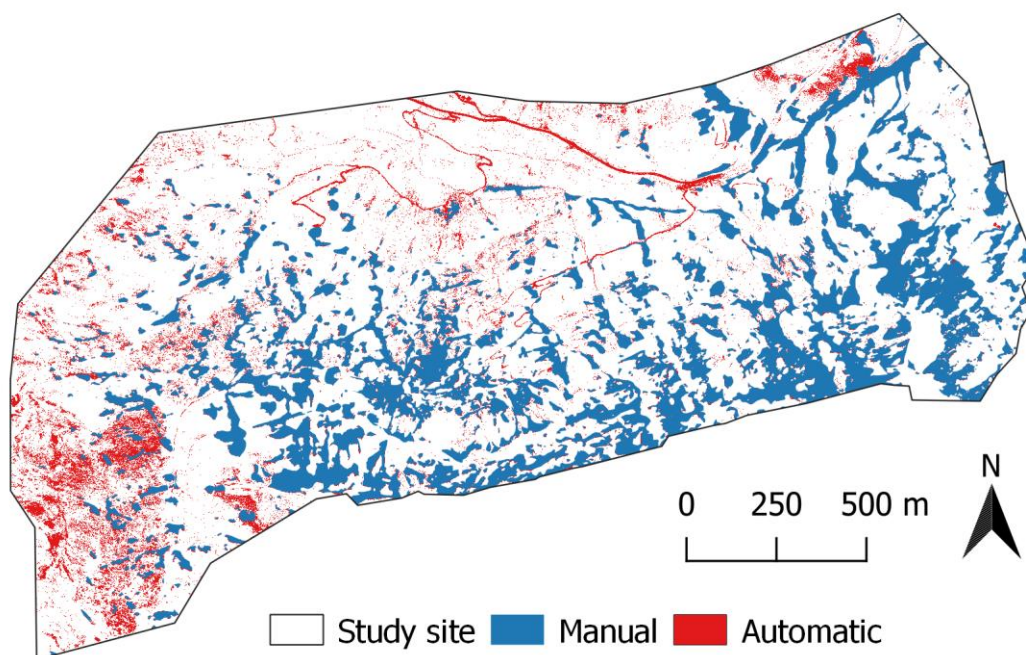


Figure 2.10: Manual and automatic (threshold value in blue band) classification of snow cover June 28th, 2019. Manual represents the *real* snow cover classification mask.

Increasing the contrast of the orthophotos before the automatic classification procedures neither resulted in a greater differentiation of karst- nor snow pixels.

2.4.1.2 Manual classification

As best approximate for the snow cover area polygons were drawn around the snow cover which resulted in a snow mask appropriate for SCA quantification and further geospatial analysis. It needs to be mentioned that the polygons are not as precise as the resolution of 15 cm of the orthophotos because such classification is extremely time-consuming and goes well beyond the scope and purpose of this thesis. However, the mask covers the corresponding snow cover in great detail and certainly more accurate as results of the tested automatic classifications. A clear benefit of the polygon mask is that it is human digitized, and the phenomena of snow-free areas classified as *snow* show a tendency towards zero. Since the logistic regression model needs discrete information about snow and snow-free areas, polygonising was an indispensable step to go.

With the gained polygons masks, the SCA and its temporal change could be quantified. Besides, the gained information could be compared to the calculated NDSI from the analyzed satellite data.

2.4.2 Snow depth distribution

Snow depth for the four different stages was obtained by subtracting the snow-free DSM from the respective snow-covered DSMs:

$$HS = DSM_{Snow\ covered} - DSM_{Snow\ free} \quad (2)$$

The resulting difference maps representing the HS distribution were reviewed with the manual drawn snow cover polygon mask to ascertain that only such areas, where visually snow cover was present, were included in further analysis. Negative HS values were regarded as *no snow*. The resulting maps had a resolution of 0.15 cm.

2.4.3 Multiple linear regression and multiple logistic regression model

2.4.3.1 Multiple regression with recorded data

For each of the surveys, where snow cover was present, it was tried to fit a Linear Model (LM) and Generalized Linear Model (GLM) on the data to predict either (1) snow height, (2) snow cover or (3) ablation for the specific day or period. The statistical analysis was performed in *RStudio* with the following data:

The dependent (or response) variable was either continuous data of HS or the categorical information about snow cover NO (0) and YES (1). The difference to a simple linear regression is that more than one parameter has to be determined using *maximum likelihood*. As predictor variables, *elevation*, *slope*, *aspect*, *solar radiation*, *wind shelter* S_x and *curvature* were used, all retrieved from the generated snow-free DSM 5 (fifth UAS survey). More information about the parameters can be found in chapter 3.6. The DSM was resampled to 1 m beforehand, since the statistical excess profit in 0.15 cm resolution is questionable and much computation time could be saved with less data.

MLR estimates the linear influence of topographic variables on snow depth. Despite its simplicity and the rather limited capability under nonlinear conditions (López-Moreno et al., 2010), MLR was used to quantify the relative contribution of each variable to the entire HS distribution model. HS was calculated from the explanatory variables for the entire study site and all UAS record days. The threshold for a predictor variable to enter in the model was set at $\alpha < 0.05$. Beta coefficients were obtained by dividing the standardized units of the coefficients by the mean value of each variable. Those were used to compare the weight of each variable within the regression models.

Building a GLM requires certain considerations and thoughts such as the interaction of predictors, the collinearity of predictors and model simplification. A problem arises when many predictors are thought to be responsible for the variance of the dependent variable because the more variables are fitted, the better becomes the fit. This problem is also referred as *variance-bias-trade-off*.³

Given the close link between the selection of a suitable model and the aforementioned problem to select the optimal from all possible parameter combinations, the model selection has received special consideration in the workflow. Because the LM assumes normally distributed data, the data was tested for normal distribution and transformed, whenever necessary. When no improvement to normal distribution could be achieved, the variable was excluded from the LM.

Before performing a regression, it is useful to test the data for correlation, similar patterns of the variables. The covariance $s_{x_1x_2}$ describes the summarized product of the deviation of each data point from the mean:

$$cov(x_1x_2) = s_{x_1x_2} = \frac{1}{n} \sum_{i=1}^n (x_{1i} - \bar{x}_1)(x_{2i} - \bar{x}_2) \quad (3)$$

³ *Variance* stands for the fraction of explained variance, thus how good the model explains the data. *Bias* describes the deviation of the model prediction for a new, independent data set, thus the error in generalizability. *Trade-off* means the consideration of two mutually exclusive objectives.

The greater the covariance, the stronger is the correlation between two variables. Given that the absolute value of the covariance depends on the absolute values of the parameters x_1 and x_2 , the standardization to values in the range of -1 and 1, the so-called *Pearson's Correlation Coefficient* r , was established:

$$\text{cor}(x_1, x_2) = r = \frac{\sum_{i=1}^n (x_{i1} - \bar{x}_1)(x_{i2} - \bar{x}_2)}{\sqrt{\sum_{i=1}^n (x_{i1} - \bar{x}_1)^2 \sum_{i=1}^n (x_{i2} - \bar{x}_2)^2}} \quad (4)$$

To test the correlation between a categorical response variable (no snow/snow) and continuous variables (e.g. elevation) *Pearson's Correlation Coefficient* or others such as *Spearman's* or *Kendall's* cannot be used. This involves a biserial correlation with Bernoulli- (snow) and normal-distributed (elevation, etc.) (Dormann, 2013).

2.4.3.2 Multiple regression with satellite data

To find out, whether a GLM has equal predictive power when fitted to free available data of coarser resolution (10 m) than the recorded data (1 m), a GLM was also fitted to the satellite data. Therefore, the recorded DSM was resampled to 10 m (satellite band resolution) and the specific parameters recalculated. The logistic regression model was built using the *glm()* function and setting family to binomial because of the discrete dependent variable (no snow/snow). The *glm* function does not assume a linear relationship between dependent and independent variables, however it assumes a linear relationship between link function and independent variables in the logit model.

2.4.3.3 Effect size

In order to detect differences between snow-covered and snow-free terrain cumulative probability curves of the explanatory variables were computed. To test whether both groups of each corresponding predictor variable were significantly different from each other, the *effect size* was calculated. Effect size is the magnitude of the difference between groups. The absolute effect size is the difference between the average, or mean, outcomes in two different intervention groups. Absolute effect size does not take into account the variability in scores, in which not every subject achieved the average outcome. Thus, effect size can refer to the raw difference between group means, or absolute effect size, as well as standardized measures of effect, which are calculated to transform the effect to an easily understood scale.

For two groups, effect size can be measured by the standardized difference between two means, or $\text{mean (group 1)} - \text{mean (group 2)} / \text{standard deviation (sd)}$. The denominator standardizes the difference by transforming the absolute difference into *sd* units. Cohen's term *d* is an example of this type of effect size index:

$$d = \frac{M_1 - M_2}{sd} \quad (5)$$

with M_1 and M_2 as difference between the group means (M) and *sd* as standard deviation of either group. Cohen classified effect sizes as *small* ($d = 0.2$), *medium* ($d = 0.5$), and *large* ($d \geq 0.8$). Between group means, the effect size can also be understood as the average percentile distribution of group 1 versus that of group 2 or the amount of overlap between the distributions of interventions 1 and 2 for the two groups under comparison (Table 2.8) (Sullivan and Feinn, 2012).

Table 2.8: Differences between groups, effect size measured by Glass's Δ (Sullivan and Feinn, 2012).

Relative size	Effect size	Percentile	% of Non-overlap
	0	50	0
Small	0.2	58	15
Medium	0.5	69	33
Large	0.8	79	47
	1.0	84	55
	1.5	93	71
	2.0	97	81

3 Results

The outcomes of the processing will be presented in this chapter. Figure 3.1 shows the flight lines and image locations for the five UAV missions. Apart from the first flight mission, all other missions were conducted in the same direction with the start of image capture at the highest elevation in the study site. Figure 3.2 illustrates the image overlap at the field site for each mission. Areas with insufficient image overlap were ignored for this study as they tend to give inaccurate outcomes through the SfM process.

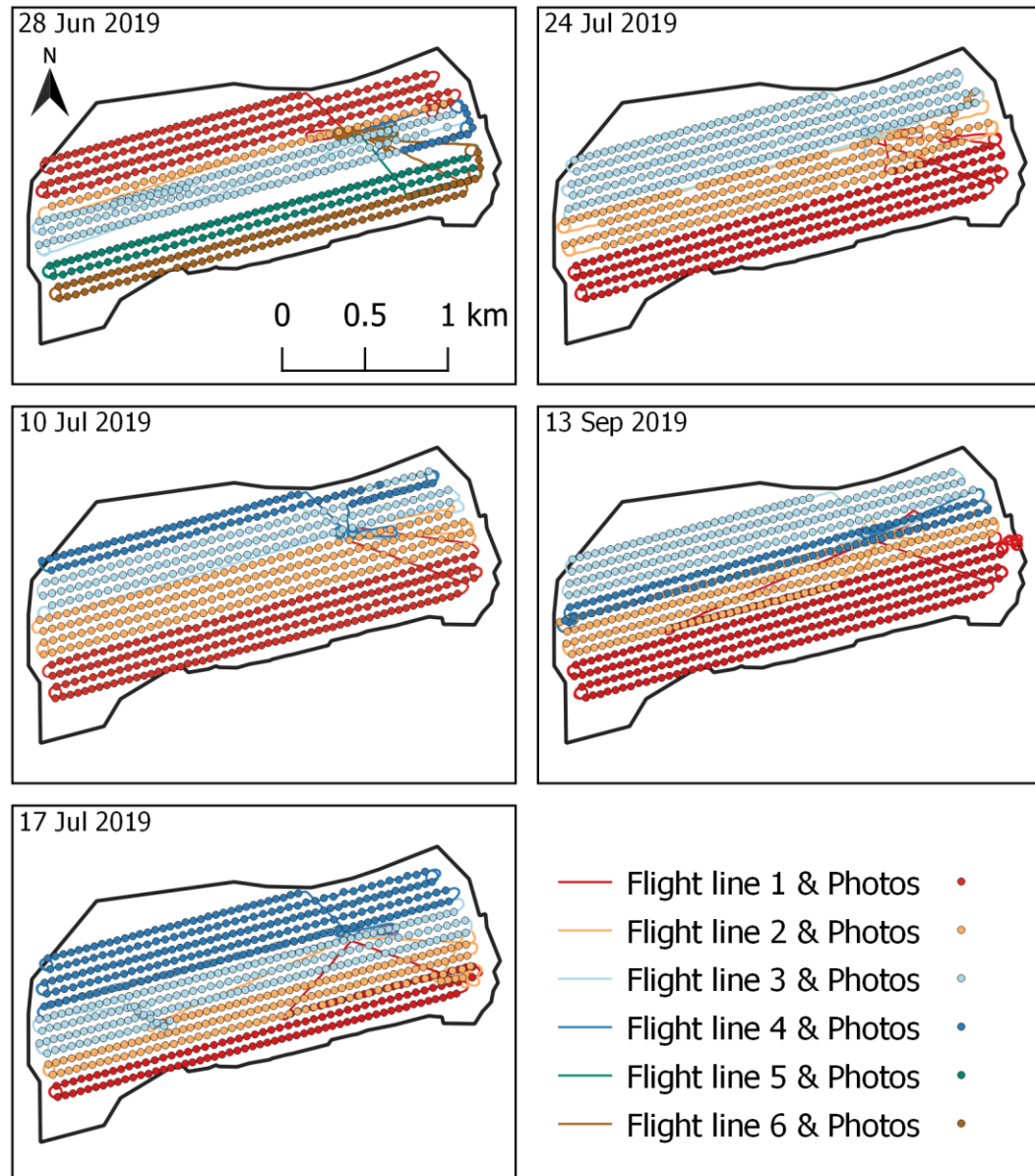


Figure 3.1: Flight lines and image capture locations for the five UAV missions.

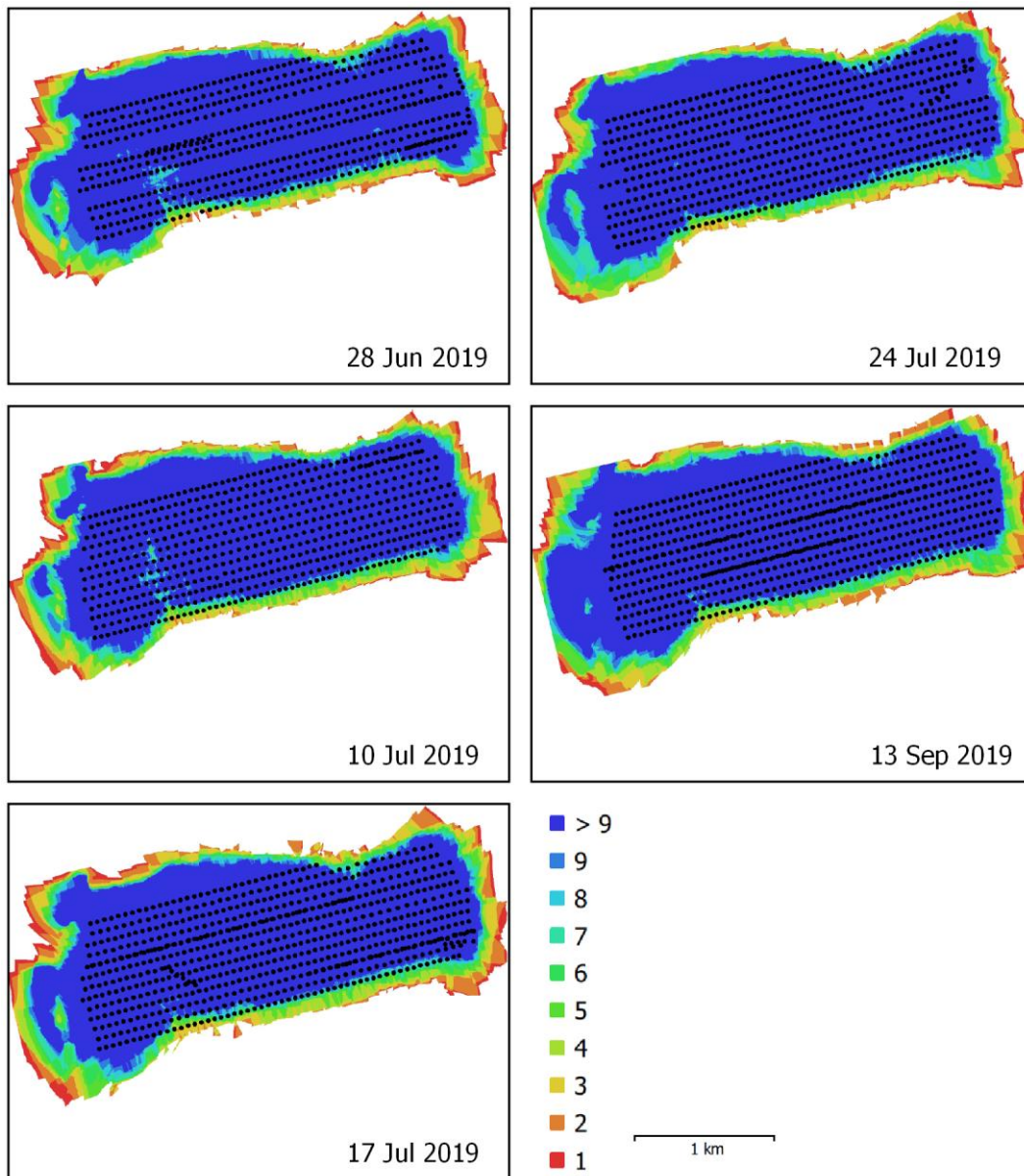


Figure 3.2: Maps of image overlap for the five UAV missions.

3.1 Orthophotos

Figure 3.3 illustrates the processed orthophotos (7.5 cm resolution) with the characteristic snow cover extent. The karst region within the study site becomes clearly visible.

For all flights with snow cover (i.e., all except the last), the snow surface had considerable texture. Since the missions were conducted in summer, the phenomena of wind-affected recent fresh snow, representing particularly challenging targets for photogrammetry, was not present for a single flight (Bühler et al., 2017). The image quality and dynamic range of the camera used in this study provided for the bigger part enough contrast across the mixed snow-bare ground conditions. However, the first mission is regarded as the most challenging one since due to high cloud coverage the light conditions were not as good which resulted in poor image

quality (blurred images with often low contrast). Still, for all missions, full photogrammetric restitution could be completed without the need for image post-processing.

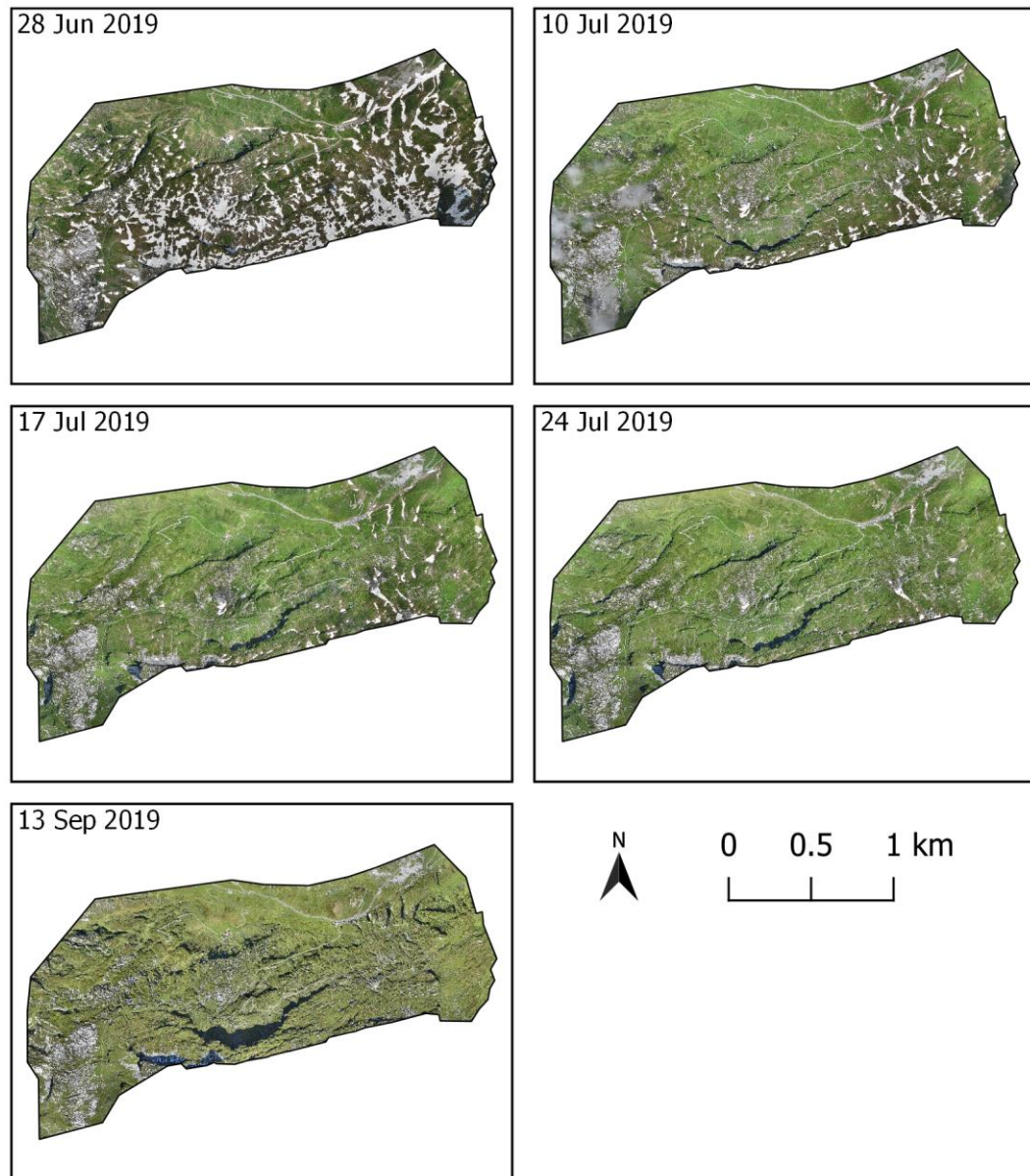


Figure 3.3: Othophotos of the five UAS surveys (Scale: 1:45,000).

3.2 Accuracy of digital photogrammetry products

3.2.1 Horizontal and vertical accuracy of GCPs

Since DEMs based on SfM-MVS are vulnerable to inappropriate error estimates, and poor image and control accuracy estimates produce complex systematic errors in DEMs (James et al., 2017), the exact accuracy of the produced DSMs, a necessity for the proceeding geospatial analysis, was examined.

As general measure of accuracy of the DSMs, the RMSE of the ten GCPs in x , y , z direction within the UAV missions was determined. It can be described as the difference in the corresponding direction between source (measured) value and estimated by PhotoScan for marker. As Table 3.1 shows, the error in x and y direction varies from 2–9 cm and 2–12 cm, while the error in z direction ranges from 4–13 cm. A total error, the distance between source and estimated location of the marker, of 20 cm is not exceeded in any DSM. The highest output resolution of the DSMs was 13.3 cm pix^{-1} but for processing reasons, all DSMs were resampled to 15 cm. For further information about the RMSE of all GCPs of the five flight missions, Tables A1–A5 are attached in the Appendix.

Table 3.1: Ground control points RMSE (X – Easting, Y – Northing, Z – Altitude).

Date	X error [cm]	Y error [cm]	Z error [cm]	Total error [cm]	Image error [pix]	Resolution [cm pix ⁻¹]	Point density [points m ⁻²]
06/28	8.07	6.78	11.84	15.85	0.126	13.8	52.3
07/10	9.28	8.50	9.56	15.81	0.145	13.6	54.3
07/17	7.59	11.81	13.30	19.34	0.159	13.3	56.4
07/24	8.33	10.90	6.87	15.34	0.263	13.8	52.7
07/13	2.94	2.16	4.30	5.64	0.147	13.8	52.7

As further indication and explanation for potential inaccuracies in the DSMs, the image residuals of the used camera can be considered (Figure 3.4). The Figure shows, that the lense distortion is unequally high within the five UAV missions but in general quite high at the edges of each image. This could be a sign of imprecise grinding. Information about the average camera location error in x , y , z direction can be found in the Appendix (Table A6).

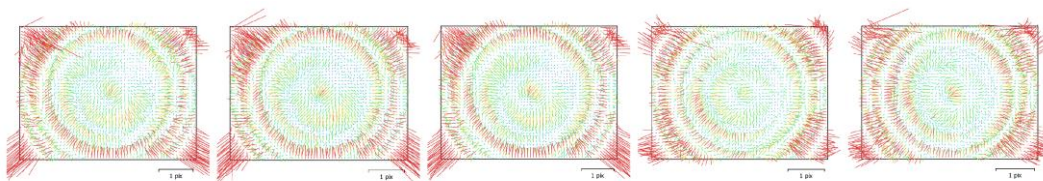


Figure 3.4: Image residuals for Canon IXUS 127 HS (Focal length = 4.3 mm) from camera calibration procedure for UVAs surveys (first = left, last = right).

To get a visual impression of the horizontal and marker placement accuracy, Figure 3.5 illustrates exemplary the location of GCP 4 (LV95: 2'708'118.156, 1'191'792.086, 1942.388) within each generated orthophoto. The corresponding X, Y, Z errors are listed in Table 3.2. With a maximum local horizontal deviation of 5 cm the orthophotos have high precision.

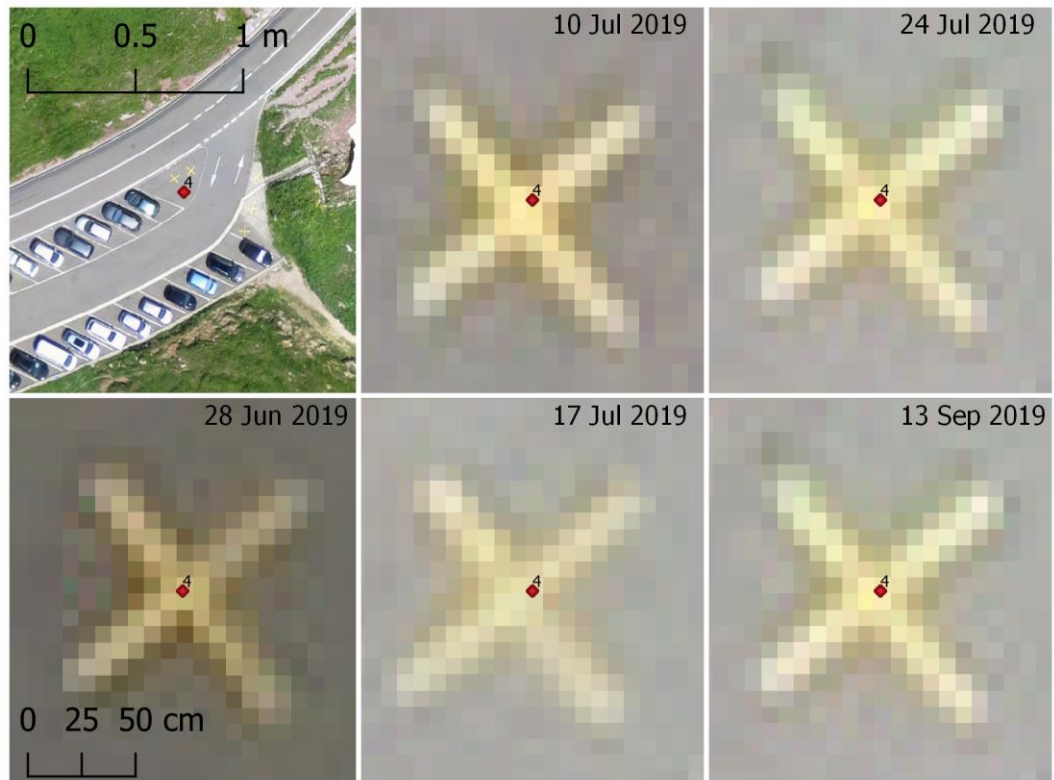


Figure 3.5: Orthophoto sections of each survey with GCP 4 to get an impression of the horizontal accuracy.

Table 3.2: RMSE of GCP 4 for the several generated DSMs

Date	X error [cm]	Y error [cm]	Z error [cm]	Total [cm]	Image [pix]	Image amount
Jun 28 19	-0.4	-0.6	17.2	17.2	0.1	13
Jul 10 19	-4.2	-1.0	9.2	10.1	8.6	22
Jul 17 19	-5.0	-2.4	5.9	8.0	0.1	20
Jul 24 19	3.6	-3.2	3.2	5.8	0.1	18
Sep 13 19	-3.2	2.6	-3.5	5.4	8.1	23

To determine the accuracy in z direction elevation values from GCP 4 were extracted from all DSMs and compared to the dGNSS measurement. Table 3.3 lists those values and deviations.

Table 3.3: Elevation value (z) and deviation to dGNSS measurement exemplary for GCP 4.

	Elevation [m]	Deviation [m]
GCP 4 (dGNSS)	1942.388	
Jun 28 19	1942.536	0.148
Jul 10 19	1942.461	0.073
Jul 17 19	1942.430	0.042
Jul 24 19	1942.395	0.007
Sep 13 19	1942.369	-0.019

The horizontal precision of the orthophotos can also be judged in Figure 3.6. It shows the location of Point 1 and 2 in large and small scale for the day of maximum snow cover during the study and the snow-free situation.



Figure 3.6: Orthophoto extract of survey 1 (left) and 5 (right). Point 1 and 2 indicate points with same XY coordinate.

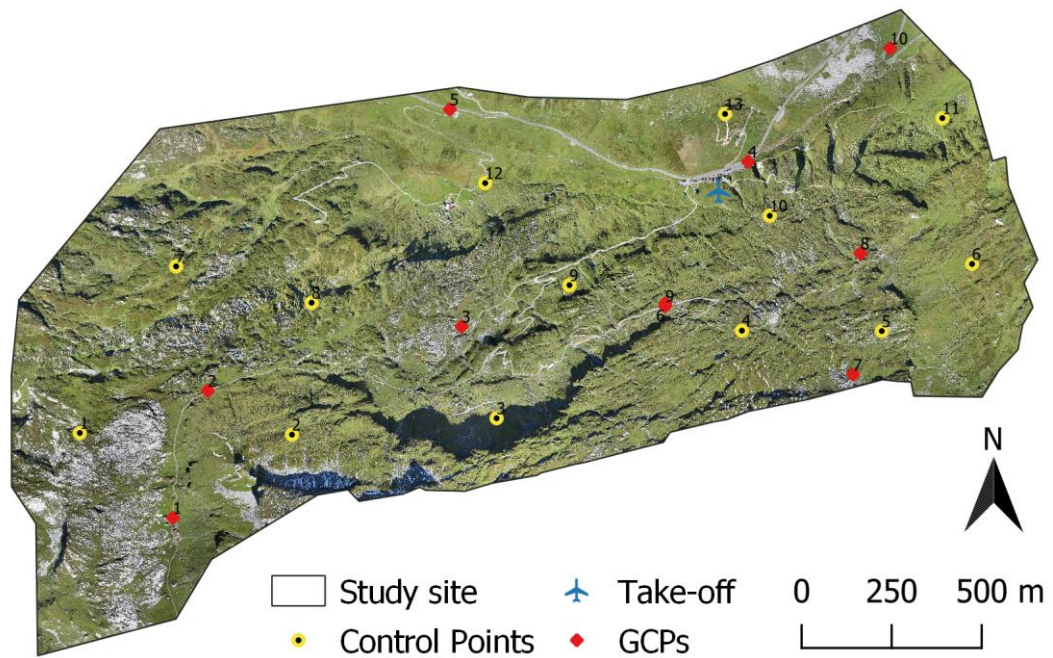
3.2.2 Vertical accuracy of control points in photogrammetric DSMs

Since the HS is retrieved by subtracting the snow-free DSM from a snow-covered DSM, only the elevation value is of interest. One needs to furthermore consider the universal accuracy in z direction, since the afore discussed accuracy mainly focused on the GCPs, points the DSM is adjusted to. To do so, 13 control points (Map 3.1) were manually distributed within the snow-free study site and elevation values for the five flight missions extracted from the generated DSMs (Table 3.4). Subsequently, the local deviation of those elevation values from DSM 1–4 from the reference DSM 5 was calculated to quantify their accuracy (Table 3.5).

Table 3.4: Elevation (in m) of control points in generated DSMs.

ID	DSM1	DSM2	DSM3	DSM4	DSM5
1	2123.24	2123.33	2123.27	2123.45	2123.36
2	2059.54	2059.32	2059.37	2059.82	2059.74
3	2130.78	2130.45	2130.20	2130.77	2130.78
4	2049.76	2049.47	2049.01	2050.34	2050.06
5	1997.94	1997.62	1997.51	1997.76	1997.81
6	1988.63	1988.59	1988.59	1988.84	1988.87
7	1969.89	1970.09	1970.09	1970.08	1970.03
8	1833.92	1834.25	1834.36	1834.18	1834.14
9	1986.80	1986.83	1986.96	1986.71	1986.63

10	1910.06	1909.94	1910.00	1910.36	1910.11
11	1904.47	1904.91	1904.75	1904.60	1904.66
12	1995.45	1995.24	1995.20	1995.04	1995.16
13	2163.76	2163.32	2162.95	2164.07	2163.92



Map 3.1: Location of GNSS measurements (GCPs), control points and take-off & landing location at the Klausen Pass field site.

Table 3.5: Deviation (in cm) of control points from reference DSM5. High deviations are marked in red.

ID	DSM1	DSM2	DSM3	DSM4	SD
1	-12.3	-3.1	-8.9	8.6	9.2
2	-20.1	-42.4	-37.5	7.4	22.5
3	-0.7	-33.6	-58.1	-1.6	27.7
4	-29.6	-58.6	-105.1	28.2	55.8
5	12.7	-18.6	-30.2	-5.3	18.5
6	-24.5	-27.9	-28.3	-3.5	11.8
7	-13.4	6.8	6.1	5.6	9.8
8	-21.6	10.6	21.9	4.0	18.5
9	17.9	20.6	33.1	8.6	10.1
10	-4.9	-17.3	-11.1	24.9	18.7
11	-19.1	24.7	8.8	-5.9	18.9
12	29.0	8.6	3.9	-12.4	17.0
13	-15.8	-60.0	-97.3	15.2	49.4
SD	17.9	28.7	42.7	11.9	

Table 3.5 highlights that the SfM products with 15 cm resolution have local deviations of between -105 and 29 cm illustrating that there is a bias within the data. With a standard deviation of 11.9 and 17.9 cm (calculated from the 13 control points) DSM 4 and DSM 1 seems to match best with the reference DSM 5 while DSM 3 matches the worst. The spatial distribution of the bias in deviation from the reference DSM 5 is highlighted in Figure 3.7.

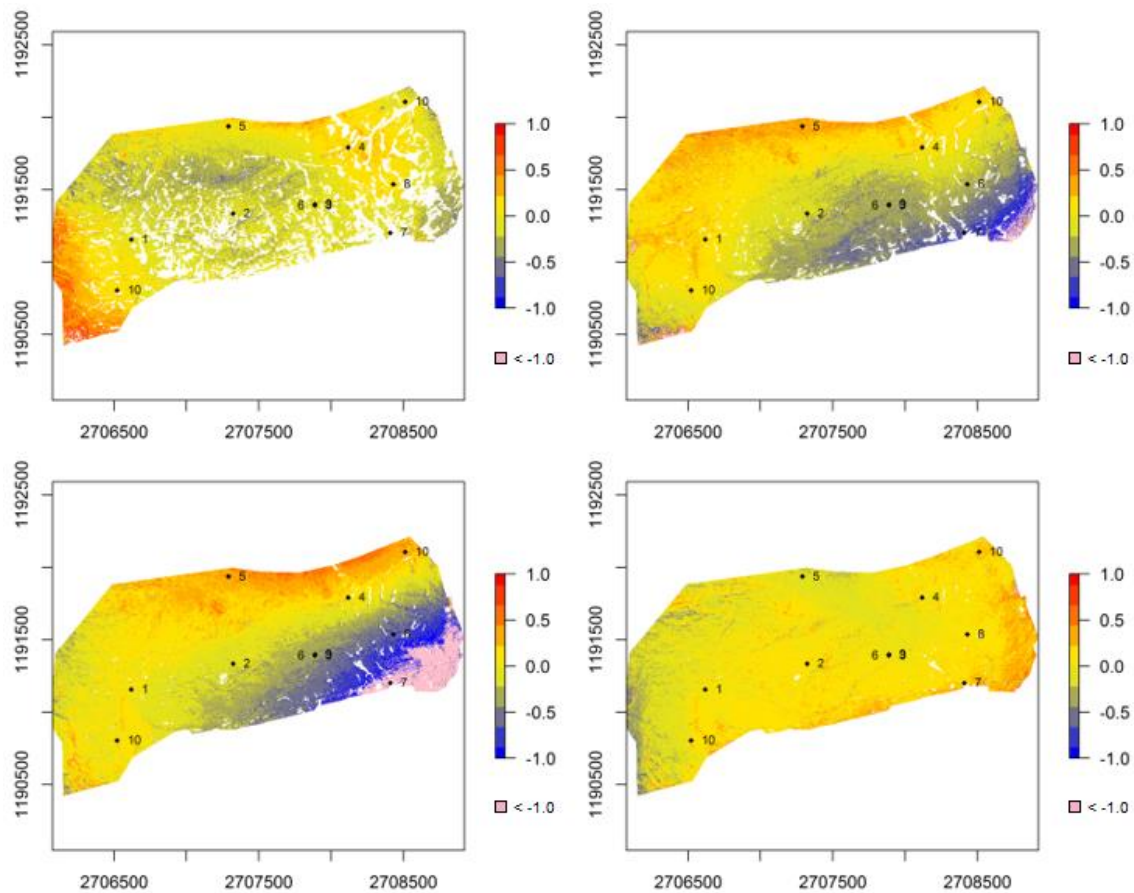


Figure 3.7: Spatial distribution of the deviation in z-direction (m) between the snow-covered DSMs (DSM1 = top left; DSM2 = bottom left; DSM3 = top right; DSM4 = bottom right) and the snow-free DSM. Pink color represents areas with a deviation smaller -1, white areas represent snow and black dots are locations of the GCPs.

To quantify the total deviation of the single DSMs from the reference DSM, only the snow-free areas were analyzed. As demonstrated in the Figure above, the four surveys had different deviations of the snow-free areas to the reference DSM with survey 2 and 3 showing the highest deviation of less than -1 m deviation locally. With a mean deviation of 14 cm within the snow-free areas, the DSM of day 4 differs the most from DSM 5, while DSM 4 shows a mean deviation of 4 cm (Table 3.6).

Table 3.6: Mean deviation of the several DSMs in respective to DSM 5.

DSM	Deviation [m]
28 Jul 2019	-0.035
10 Jul 2019	-0.086
17 Jul 2019	-0.145
24 Jul 2019	0.035

Since DSMs with this bias-artefact are inappropriate for accurate HS determination, a bias correction was applied to the four surveys. The goal here was to correct the snow-covered DSMs (1–4) in all locations for their specific deviation from the reference DSM to receive a corrected snow surface for accurate HS determination. The open source software *RStudio* was used to do the bias correction for the four surveys and was rather computation time intense for the 15 cm resolution DSMs. The bias correction was performed as follows to receive the corrected DSMs.

First, the reference DSM was subtracted from the snow-free mask of each survey to receive a deviation mask. Then, the deviation raster was interpolated to fill the unknown data (areas where snow was existent). Subsequently, a 3 m Median filter was applied to the interpolated deviation map to smooth the surface and exclude outliers. A 3 m window was considered to be sufficient, since among others, the computation with a 10 m Median filter would have been far more time-consuming, as a test run showed. By subtracting the smooth deviation raster of survey 1–4 from the original DSMs 1–4 the surface of the original DSM was corrected for every raster cell by its specific local deviation. As a result, DSMs with corrected snow surface were retrieved. The accurate HS could subsequently be calculated by subtracting the reference DSM from the new corrected DSMs 1–4.

Processing steps of bias correction compact:

- 1) Calculate DSM deviation of survey 1–4 (only snow-free areas) with snow-free reference DSM 5
- 2) Cubic Interpolation of NoData values in deviation raster
- 3) Apply 3m Median filter on deviation raster with interpolated *snow surface*
- 4) Subtraction of interpolated and filtered deviation map from original DSM of survey 1–4

➔ Corrected DSMs 1–4 ➔

3.3 Snow depth maps

As illustrated in Figures 3.8 and 3.9 and listed in Table 3.7 the snow depth varied from zero to the absolute maximum of 6.78 m. The resulting snow depth maps visualize the high spatial variability of HS even within short distances of a few meters. Snow traps for wind-blown snow and potentially deposits from past avalanche activity can be identified easily by high HS values.

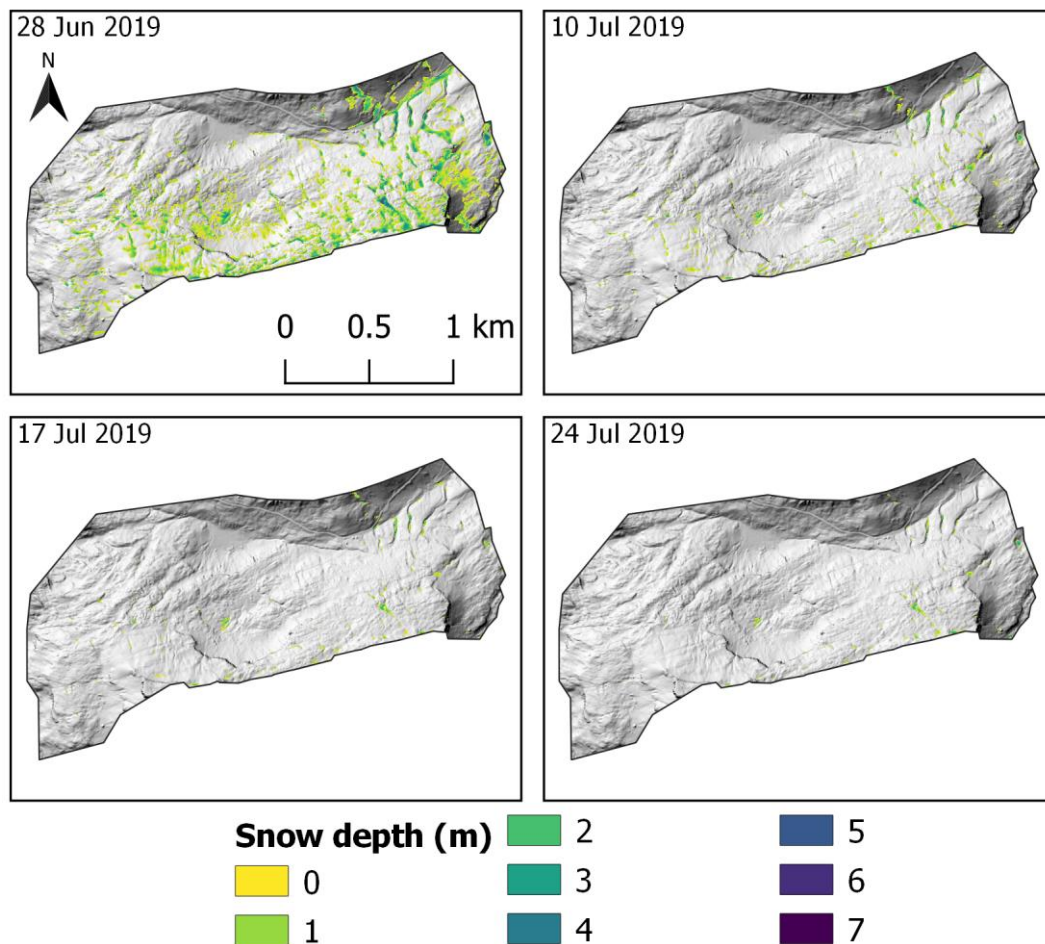


Figure 3.8: Snow depth maps of the four different surveys retrieved from the corrected DSMs (15 cm resolution).

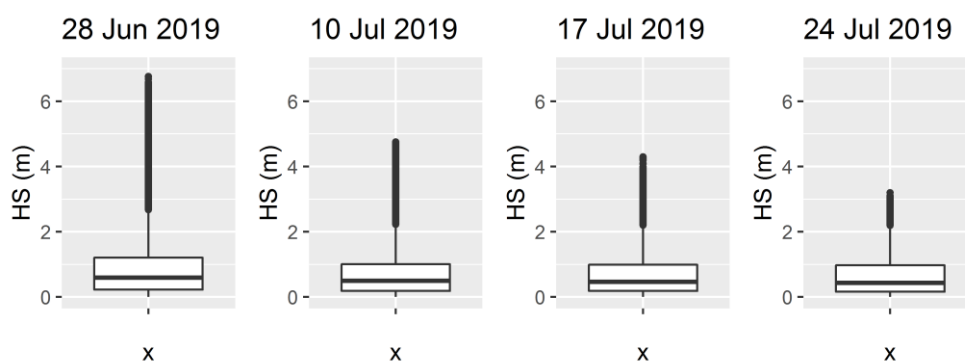


Figure 3.9: Boxplots of the HS data from the 4 different surveys (1 m resolution).

Table 3.7: Quantiles of the four recorded HS distributions.

Date	25%	50%	75%	100%
Jun 28 2019	0.22	0.60	1.20	6.78
Jul 10 2019	0.19	0.50	1.00	4.86
Jul 17 2019	0.18	0.47	0.99	4.31
Jul 24 2019	0.16	0.43	0.97	3.50

From the quantiles for the cell values of the corrected HS raster layers cannot be ascertained large differences between the last records. The reason for this behavior is the already extensively depleted snow cover with only small but densely packed snow patches remaining. The only greater difference can be ascertained for the transition from June 28th to July 10th where a great amount of the absolute snow cover depleted (81%, chapter 3.4).

Figure 3.10 shows sections scaled up to illustrate the spatial and temporal depletion of the snow cover exemplary for the two areas at the study site with the initially greatest HS. It seems that the greatest HS and snow in general is deposited in depressions, as the hillshade shows.

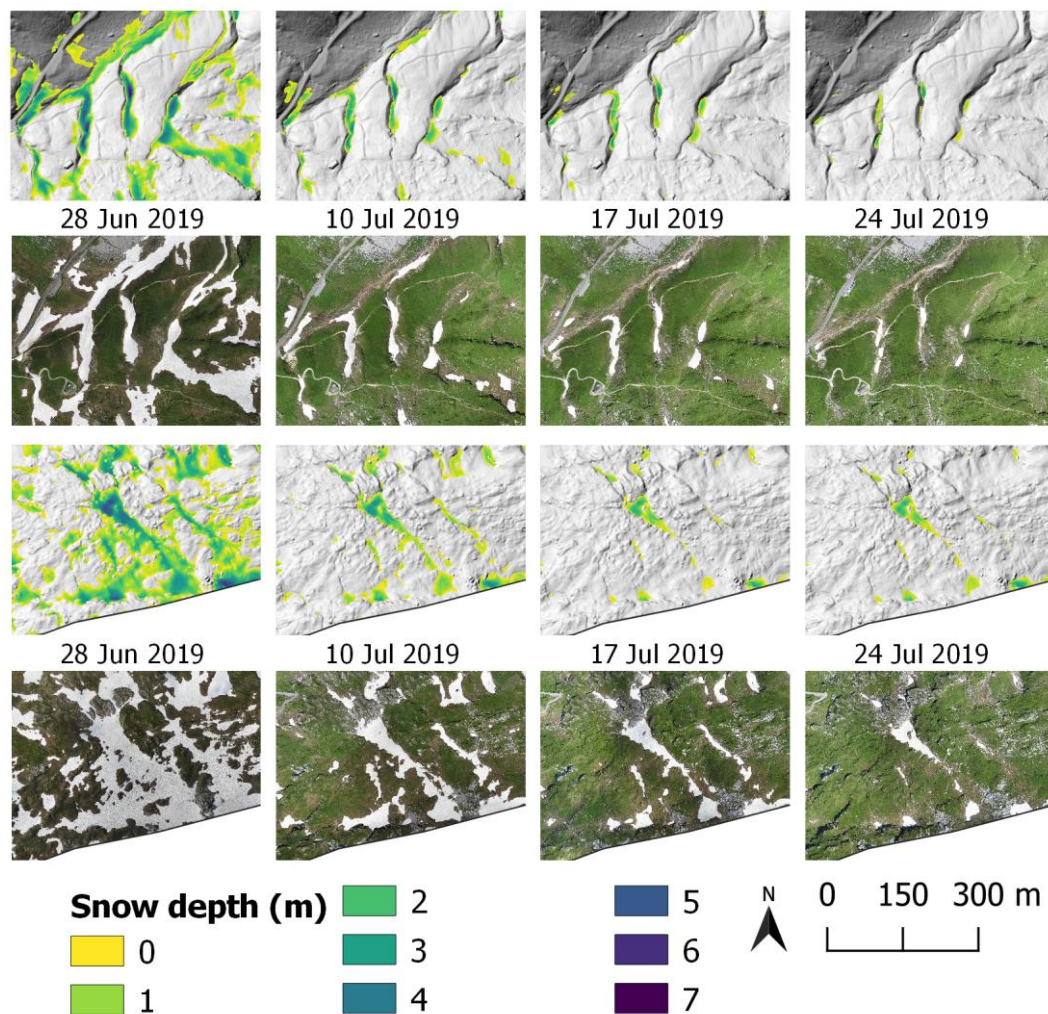


Figure 3.10: Stepwise depletion of the snow cover, exemplary for areas at the study site with initially greatest HS.

3.3.1 Snow depth validation using the manual snow depth measurements as reference data set

To get an estimate of the accuracy of the modeled HS, these were validated against the manually measurements in the field during the surveys. Since the coordinates of the HS measurements were not taken with a dGNSS but with a GPS of 10 m accuracy, a direct comparison is impossible. To get at least an estimate of accuracy, from the generated HS raster maps, median values were extracted in a buffer of 10 m around the in total 252 manual HS measurement locations (Figure 3.11).

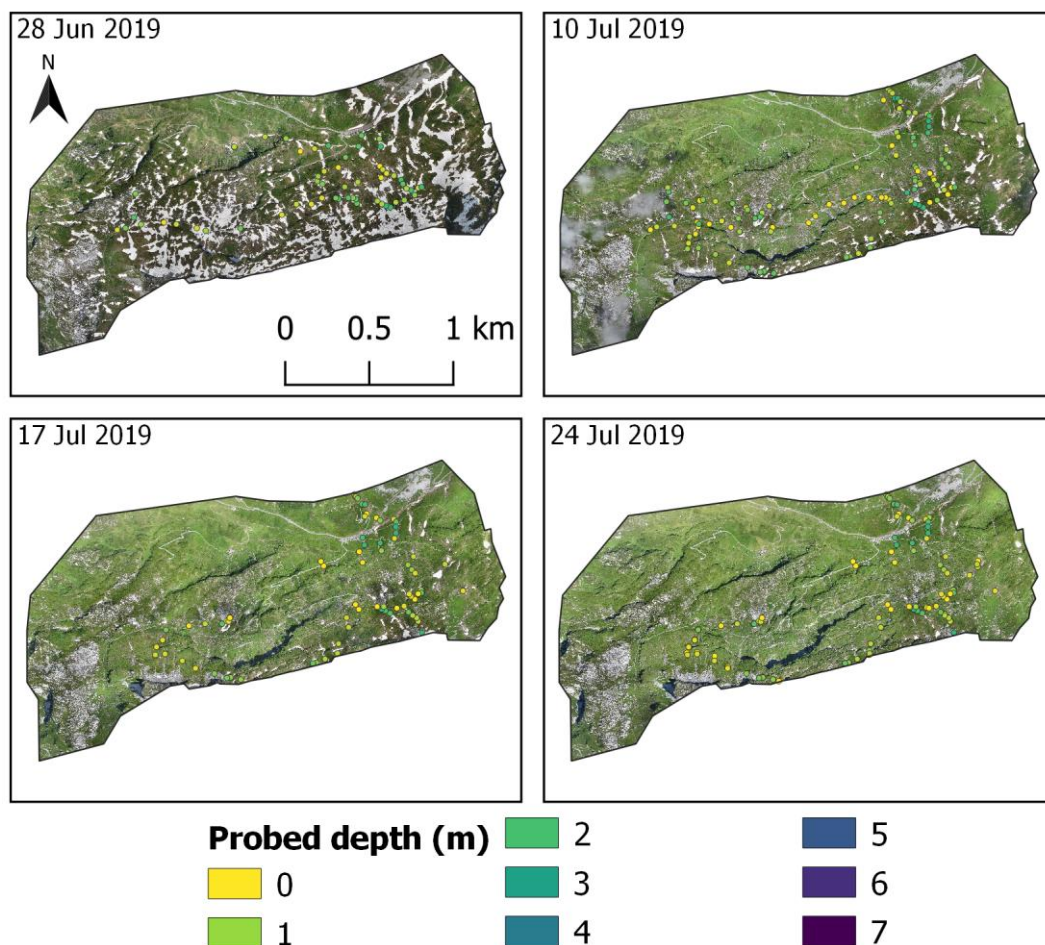


Figure 3.11: Orthophotos of the single flight missions with location and snow depth (m) of manual measurements.

The median was chosen because of its robustness against outliers compared to the mean (see attached Figure A1 in Appendix). Figure 3.12 shows that the HS produced from the difference DSMs are underestimated for great probed HS while HS under 75 cm match quite well. With a RMSE of 0.62 (Table 3.8) the difference between sampled and modeled HS is slightly highest.

According to the coefficient of determination R^2 (between 0.12 and 0.23) for none of the validation data a clear conformity with the modeled HS can be found but again, a direct comparison is impossible and hence the information about the accuracy of HS here given should

be interpreted with caution. Sources of error in the measurement of especially thin snowpack (< 20 cm) such as real changes on the ground like frost heave, vegetative compaction by snow or even footprints (Nolan et al., 2015) need to be considered. However the data shows that mapping HS can be done at substantially lower costs than current methods and may find wide application in the future in studying snow cover change on the catchment scale.

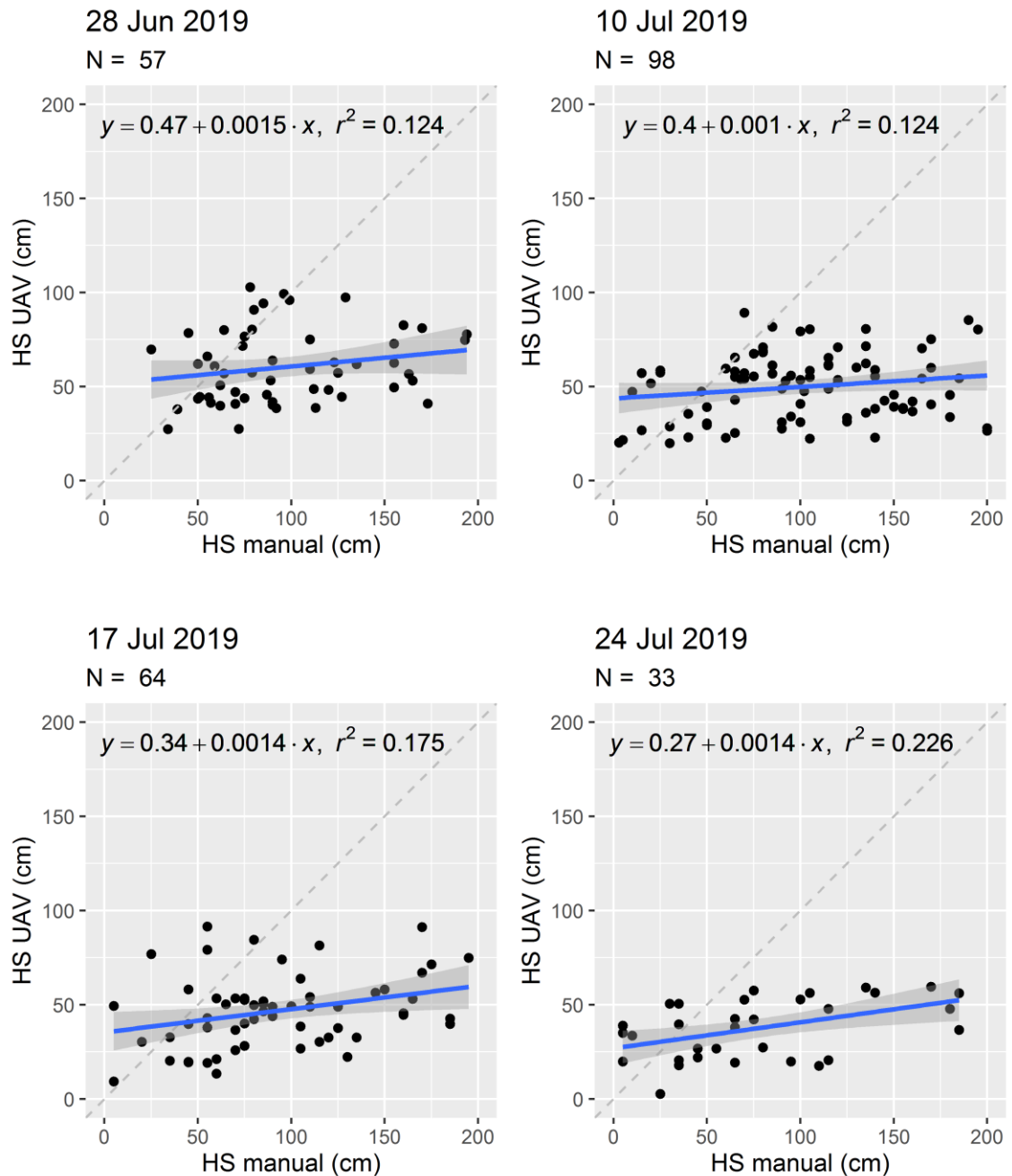


Figure 3.12: Absolute median values of manual and modeled HS (cm) for the four surveys.

Table 3.8: RMSE of modeled and probed snow depth for the 4 UAS surveys.

	Jun 28	Jul 10	Jul 17	Jul 24
RMSE	0.62	0.86	0.77	0.64

3.4 Snow cover area

The analysis of the UAS data obtained a maximum snow coverage of almost 21% at the beginning of this study campaign with 0% coverage at its end (Table 3.9), calculated from the 7.5 cm resolution orthophotos.

Table 3.9: Snow cover extent in square metres, square kilometres and percentage of the total study area (2.91 km^2) derived from the orthophotos from the UAS missions.

Day	Extent [m ²]	Extent [km ²]	Part of area [%]
Jun 28 2019	605199	0.6052	20.8
Jul 10 2019	112805	0.1128	3.9
Jul 17 2019	50663	0.0507	1.7
Jul 24 2019	14788	0.0148	0.5

3.4.1 Comparison of SCA with SENTINEL-2 data

To get an idea of the deviation of SCA retrieved from satellite and UAS data, the downloaded SENTINEL-2 products were analyzed and compared to the UAS data. Table 3.10 indicates that the SCA of flight mission 1 is underestimated by the coarser resolution satellite data by about 0.25 km^2 and thus almost 9% of the total study site. This is a total error of about 42%. However, it must be mentioned that the satellite record originates from one day later than the UAS mission. The error of underestimation decreases with decreasing SCA. For flight mission 3 the SCA is underestimated by 1.5% by the satellite, which can be described as an absolute error of 88%.

To receive information about when the SCA started to deplete, satellite data before the first flight campaign was analyzed. Table 3.10 indicates that the main snowmelt occurred during May 30th and June 19th with a shrinkage of SCA by about 53%. Those areas on the generated NDSI map for June 24th are considered areas where the snowpack totally melts to ground earliest and could potentially represent sections where the least snow accumulates during winter season. Therefore, such areas were further analyzed for their characteristic topographic parameters to test the hypothesis whether snow cover can be linked to topography. June 24th suits especially well for the proceeding analysis (chapter 3.6.3), since it splits the study site in 50% snow-covered and 50% snow-free terrain.

Since the SCA had about 1.5 hectares on July 24th and the snow-free DSM was recorded on September 13th and thus 1.75 months later, the satellite record of August 8th provides information about the total depletion of the SCA.

Table 3.10: Snow cover extent in square metres, square kilometres and percentage of the total study area derived from the NDSI from SENTINEL-2 bands. Green marked rows represent satellite records temporally close or equal to the UAS missions.

Date	Extent [m ²]	Extent [km ²]	Part of area [%]
Mar 23 2019	2905100	2.91	99.7
Mar 31 2019	2896400	2.90	99.4
Apr 20 2019	2884400	2.88	99.0
May 30 2019	2897900	2.90	99.5
Jun 01 2019	2776500	2.78	95.3
Jun 19 2019	1363400	1.36	46.8
Jun 24 2019	813300	0.81	27.9
Jun 26 2019	607000	0.61	20.8
Jun 29 2019	348900	0.3489	12.0
Jul 16 2019	5900	0.0059	0.2
Jul 19 2019	6800	0.0068	0.2
Jul 24 2019	2300	0.0023	0.1
Aug 08 2019	0	0	0
Aug 18 2019	0	0	0
Aug 25 2019	0	0	0
Aug 30 2019	0	0	0
Sep 09 2019	2472900	2.4729	84.9
Sep 12 2019	21200	0.0212	0.7
Oct 17 2019	2196600	2.1966	75.4

Figures 3.13 and 3.14 illustrate the generated real color composite images and corresponding NDSI maps at the study site for most dates listed in Table 3.10. These figures visualize the snow cover depletion process between March 23rd and August 8th and also indicate the subsequent transition to autumn with the first snow accumulation events since the end of September 2019.

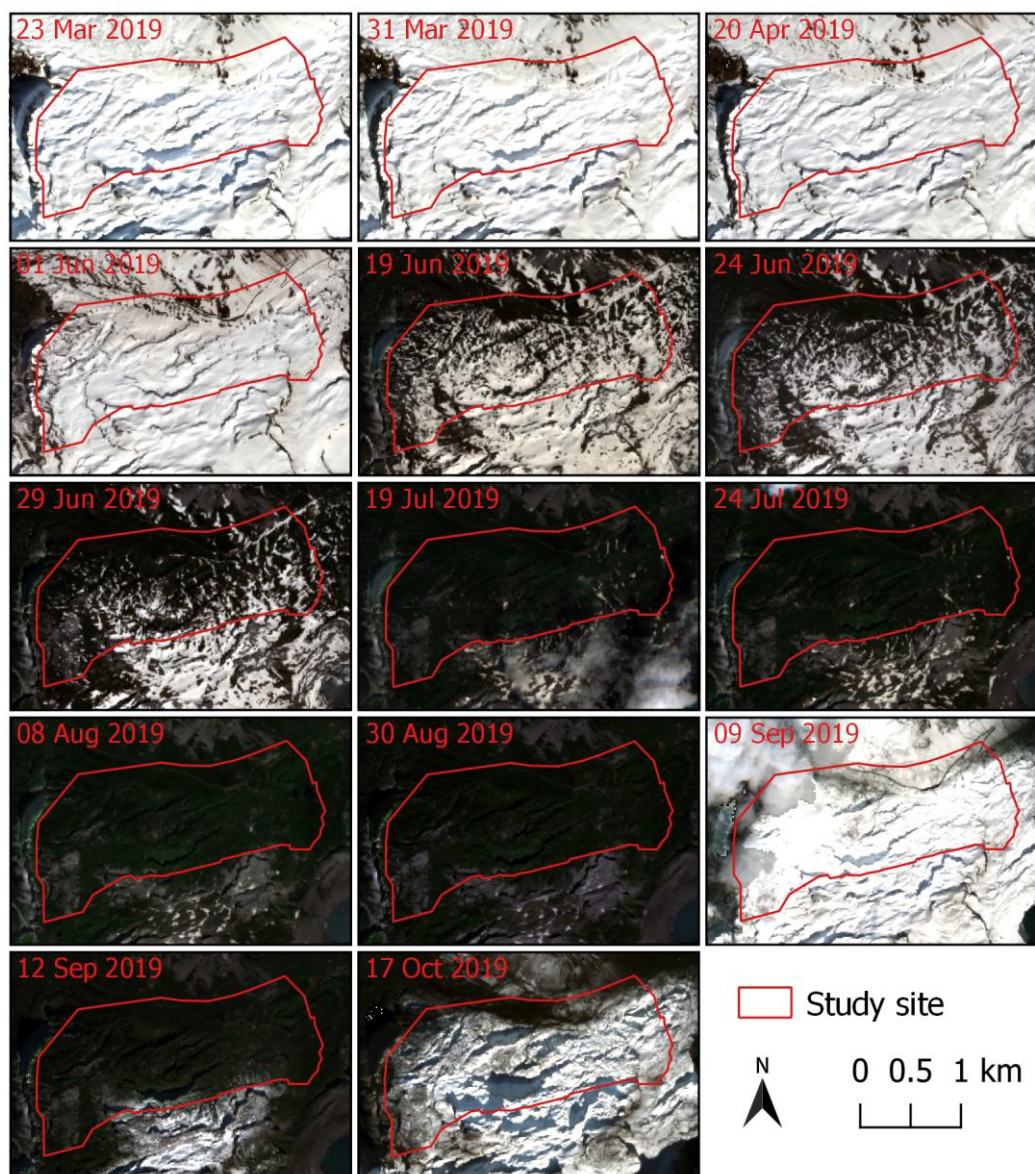


Figure 3.13: Real color composite images of study site derived from SENTINEL-2 data (Band 2, 3, 4).

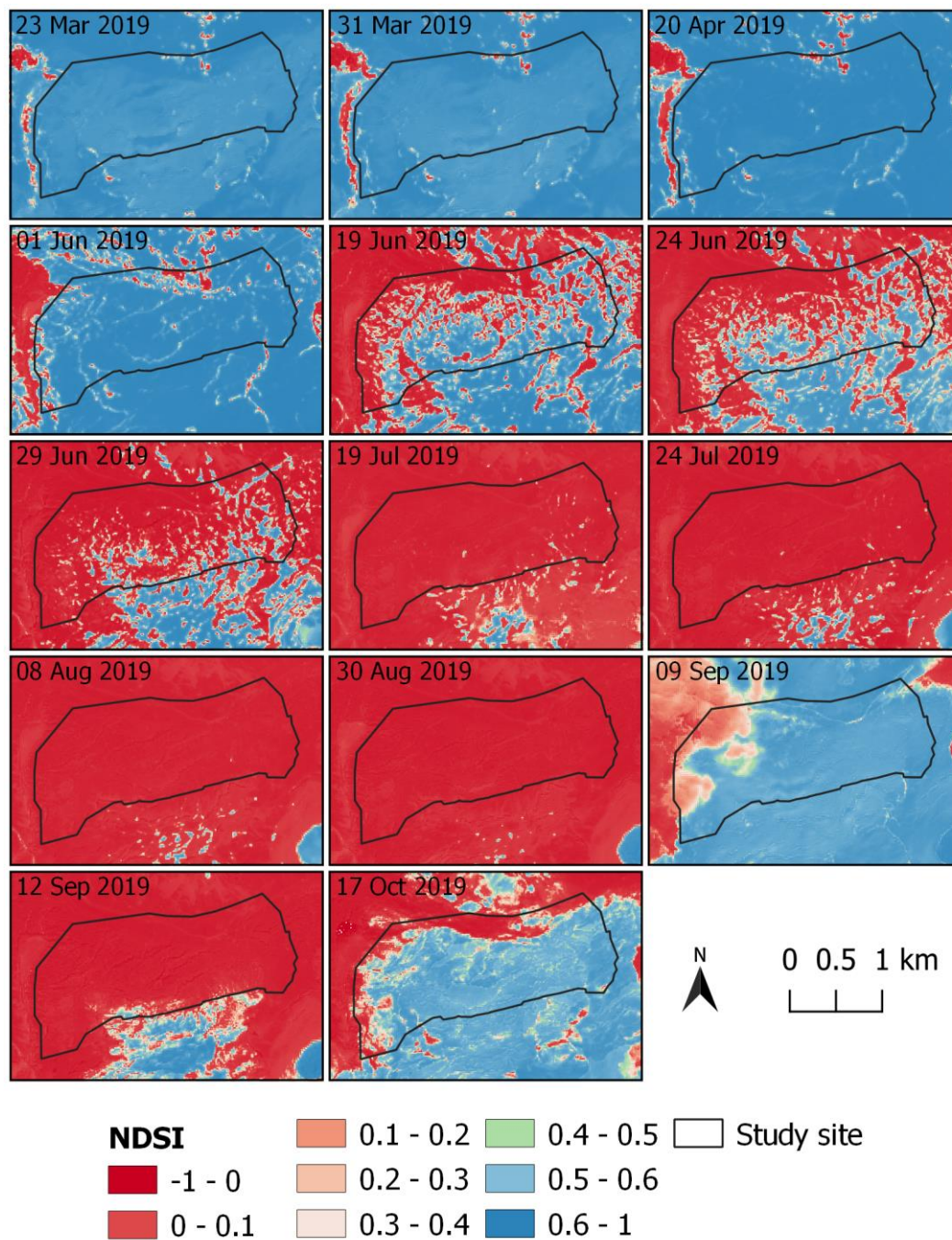


Figure 3.14: NDSI maps of study site derived from SENTINEL-2 data (Band 3, 11).

3.5 Snow water equivalent and ablation rates

The SWE characterizes the hydrological significance of snow cover for which reason the necessary measurements to calculate SWE were performed in the field. Although SWE can be estimated using several remote sensing techniques, its direct calculation involves multiplication of HS measurements by snow density q estimates (Jonas et al., 2009). In Table 3.11 the resulting snow densities from the multiple measurements of each field day are listed. The snow density was calculated as the mean of the multiple performed measurements per day. With 587 kg m^{-3} the measurement of June 24th has the highest snow density. To put the measurements in a

scientific context, Pelto et al. (2019) report glaciological spring snow density of $457 \pm 50 \text{ kg m}^{-3}$. The general denotation of partially melted and compacted snow that has a density of at least 500 kg m^{-3} is *Névé* (Pidwirny, 2008). The SWE (mm) was calculated by multiplying the mean HS (cm) with the snow density (kg m^{-3}) divided by 100:

$$SWE = HS * \frac{\rho_{\text{Snow}}}{100} \quad (6)$$

Table 3.11: Characteristic snow depth values (mean, median, maximum HS), snow density q , snow water equivalent SWE, snow volume V at each day of UAS survey and runoff rate Q of snow covered areas between the UAS surveys.

Date	Mean HS [cm]	HS median [cm]	HS max [m]	q [kg m^{-3}]	SWE [mm]	V [m^3]	Q [mm d^{-1}]
Jun 28 2019	84.19	59.83	6.78	535.48	450.80	272826	33.15
Jul 10 2019	71.01	50.11	4.86	485.51	344.75	38890	52.45
Jul 17 2019	68.14	46.95	4.31	571.79	389.59	19738	55.80
Jul 24 2019	66.70	43.16	3.50	587.15	391.63	5791	

The calculated SWE per square meter had a range from 345 to 450 mm. By multiplying the SWE with the SCA of the specific day, the snow volume V in cubic meters was retrieved. Therefrom, the specific melt amount during the consecutive surveys could be quantified as well as the specific runoff rate Q for the snow-covered areas between the UAS surveys. With 56 mm d^{-1} the runoff rate of snow-covered areas was highest between July 17th and 24th, 2019.

Figure 3.15 illustrates the absolute ablation and the ablation rate in cm d^{-1} between the consecutive flight missions.

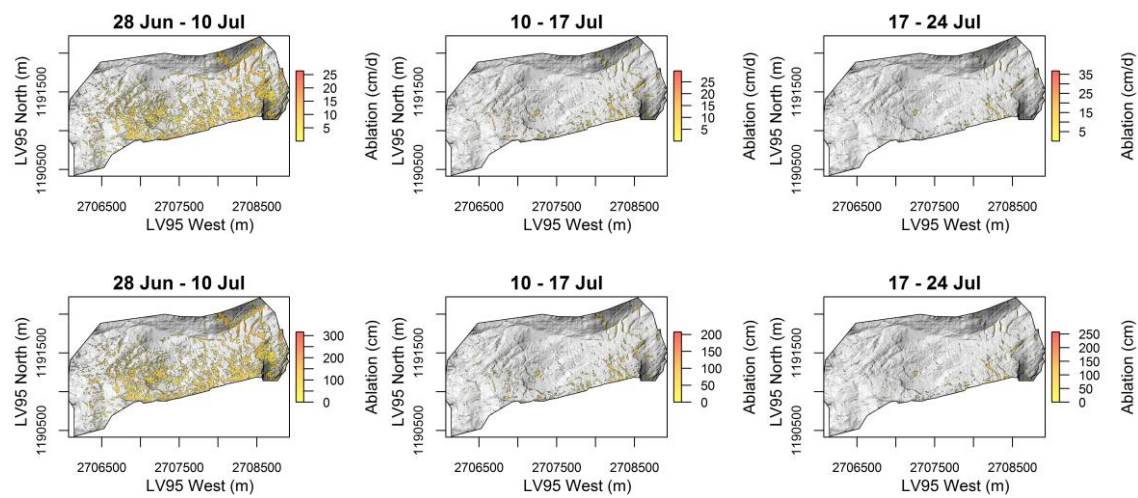


Figure 3.15: Absolute ablation in cm and ablation rate in cm per day for the corresponding periods between the UAS surveys.

With more than 300 and 250 cm total ablation locally, the periods June 28th to July 10th and July 17th to 24th, 2019 showed more snowmelt than the period between. Overall, the period between showed the greatest daily ablation rate with more than 35 cm locally. This is in line with the air temperature record of the IMIS station *Alpler Tor* (Figure 3.16).

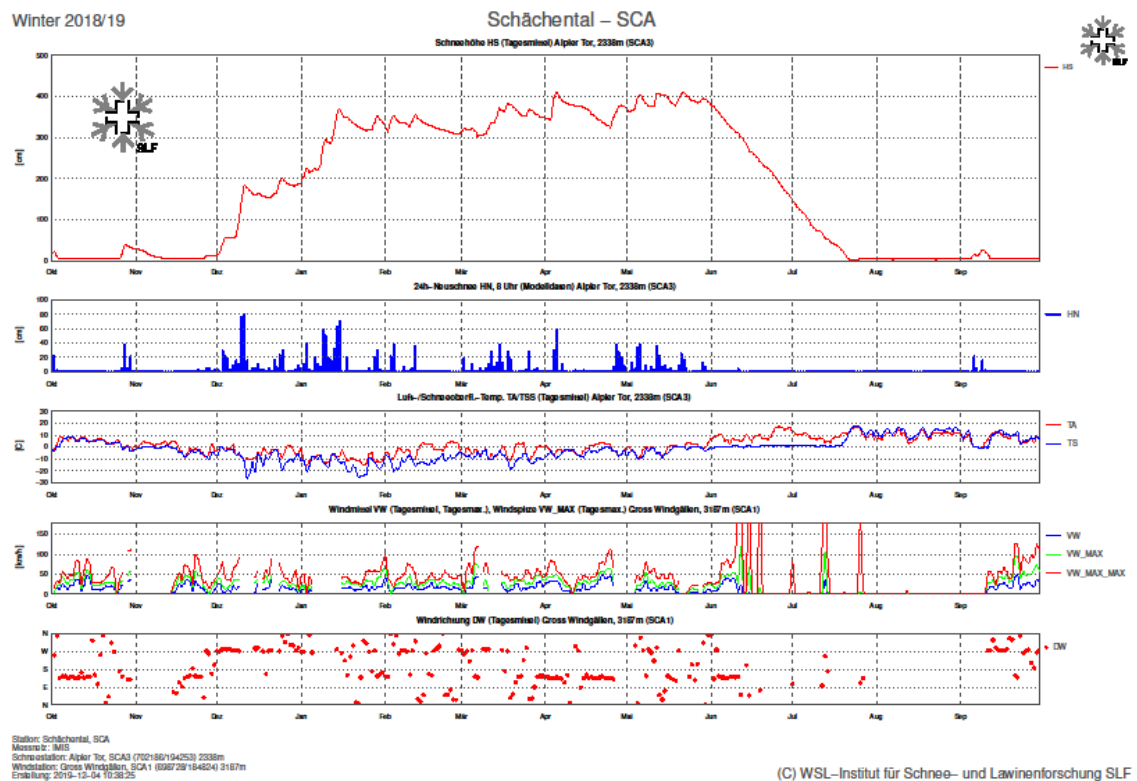


Figure 3.16: Data of the IMIS stations *Alpler Tor* and *Schächentaler Windgällen* between Oct 1st, 2018 and Sep 30th, 2019. Snow depth in cm (HS), 24-h new snow in cm (HN), Air (TA) and snow surface (TS) temperature in °C, wind speed in km h⁻¹ as daily mean (VW), daily mean maximum (VW_MAX), daily maximum (VW_MAX_MAX) and wind direction as daily mean (DW). (SLF-Messdaten©2019, SLF).

According to the runoff station data '*Schächen – Bürglen, Galgenwäldli*' (LV95: 2'692'480.601, 1'191'809.801, 590 m a.s.l.) of the *Federal Office for the Environment* (FOEN), monitored by the Hydrology Division and located 15.5 km west and 1460 m lower than the Klausen Pass (Figure 3.17), the snowmelt peak was on June 11th, 2019 with a daily mean/absolute runoff of 34.4/50.6 m³ s⁻¹. With a monthly mean runoff of 18.4 m³ s⁻¹, June represents clearly the snowmelt period (compared to May and July with 8.9 and 8.2 m³ s⁻¹, respectively). The daily mean runoff during the first and fourth survey varied between 15.9 m³ s⁻¹ (June 28th) and 5.7 m³ s⁻¹ (April 24th) and showed a constant recession indicating the slow melt of the last remaining snow patches.

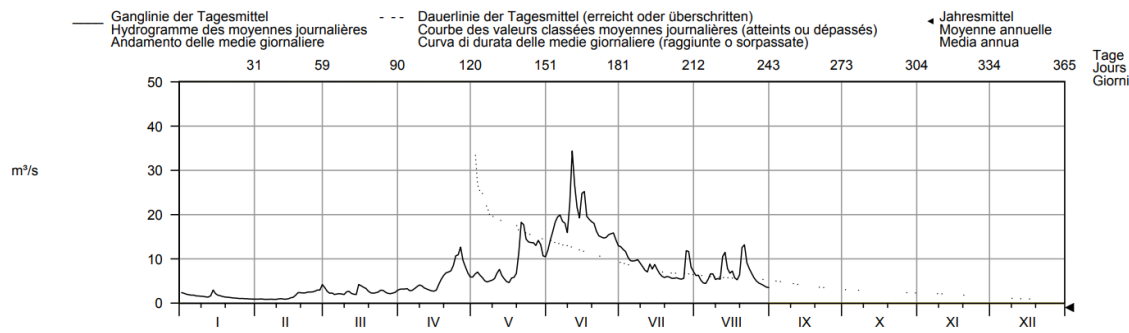


Figure 3.17: Hydrograph of daily mean of the Schächen from January to August 2019 (FOEN, 2019).

3.6 Geospatial analysis

3.6.1 Statistical preliminary investigations

3.6.1.1 Explanatory variables and their distributions

To predict both SCA and HS within the study site, GLMs and LMs were built. Therefore, the values of the explanatory variables had to be derived from the recorded snow-free DSM of 1 m resolution. Figure 3.18 illustrates those derived raster maps.

Elevation describes the height of each raster pixel in meters above sea level while *slope* represents both the direction and steepness of a raster cell expressed in degrees (0–90). *Aspect* describes the compass direction in degrees (0–360) that a slope faces. *Solar radiation* describes the solar input in kilowatt hours per square meters (Wh m^{-2}), calculated for the rough snowmelt period at the site (April 1st to July 31st, 2019), according to the IMIS station data *Alpler Tor* (Figure 3.16). The parameter *Sx* was calculated based on the assumption of a dominant western wind direction (270°). The reference DSM (2 m resolution) of the area of interest was provided by the SLF. *Sx* is based on maximum upwind slopes relative to seasonally averaged winds and used to characterize the wind scalar at each pixel location of the input DSM. Since the data of the wind station *Gross Windgällen* did not show any logical tendency towards the dominant wind direction for the winter half year (Figure 3.19), the dominant wind direction was assumed to be West (270°). This direction is more in line with the topography of the study site where wind channeling effects can be assumed because of the steep faces both, north and south, of the Klausen Pass. *Curvature* is the amount by which a curve deviated from being a straight line or a surface deviates from being a plane. A part of a surface can be concave or convex and the curvature value allows to discriminate both. Since snow favorably deposits in depressions and gets blown away on convex surfaces, curvature was assumed to be a good predictor variable for the snow distribution.

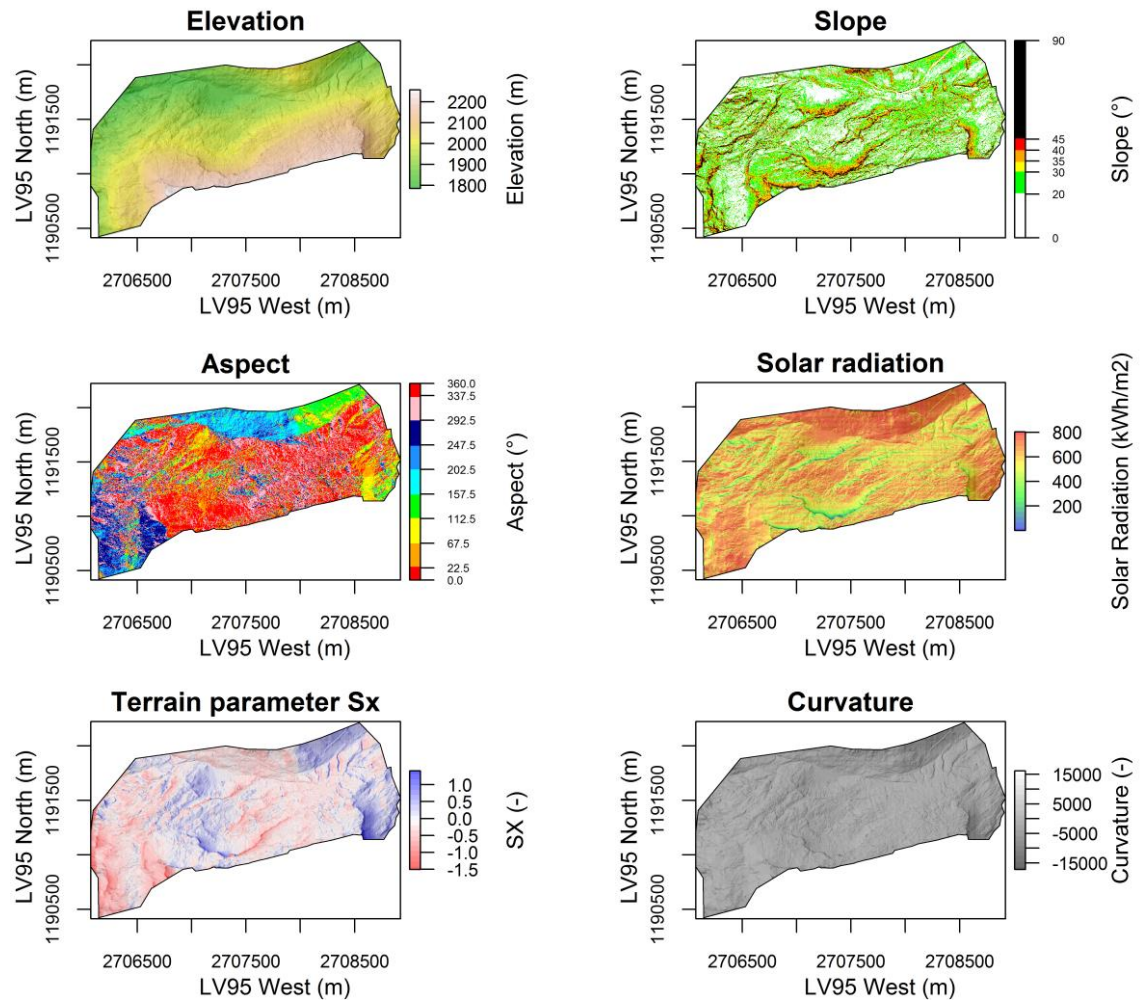


Figure 3.18: Maps of predictive variables elevation, slope, aspect, solar radiation, terrain parameter Sx and curvature underlayed with hill shade (1m resolution).

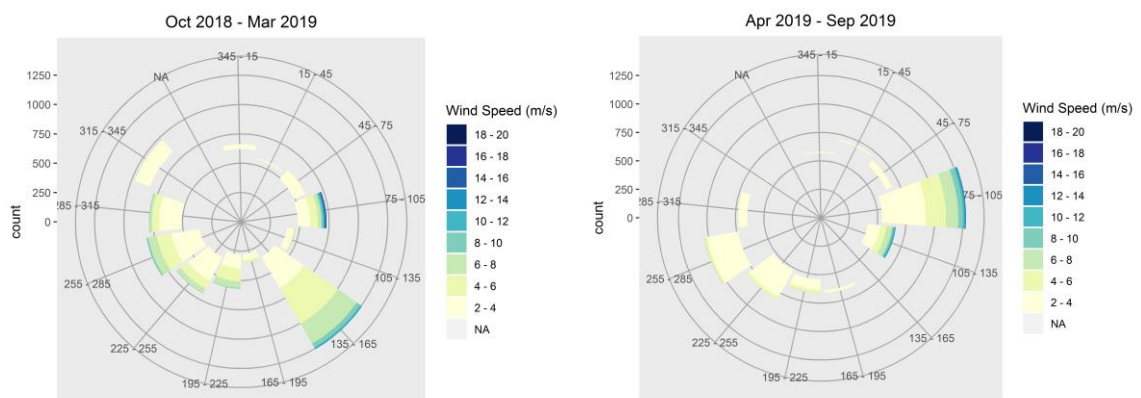


Figure 3.19: View of how wind speed and wind direction are distributed for both winter (left) and summer (right) season according to data of the wind station *Gross Windgällen* illustrated as wind rose.

To get a general impression of how the values of the explanatory variables are distributed within the study area the histograms were plotted and a normal curve was added with the same mean and standard deviation (Figure 3.20). The plots indicate that all parameters besides aspect hold a normal distribution. The outliers of curvature, as listed in Table 3.12, represent extremely high values and account for the deviation of the distribution of the data from the normal distribution since mean and standard deviation are computed from it. When excluding the outliers (values below/above 25th percentile/75th percentile – 1.5 * Interquartile range (IQR)), curvature data follows a normal distribution. The values listed in Table 3.13 represent the skewness and kurtosis of the data. Under the hypothesis of normality, the data should be symmetrical and hence skewness should be equal to zero. Kurtosis should have a value equal to zero under the hypothesis of normality. According to the calculated skewness of the explanatory data, elevation and slope are slightly right (positively) skewed while aspect, the terrain parameter Sx and curvature are slightly left (negatively) skewed. The distribution of solar radiation is strongly left skewed. According to the definition of kurtosis, values greater three represent a leptokurtic, values equal to zero a mesokurtic and values smaller three a platykurtic distribution (Spektrum der Wissenschaft, 2014). While the distribution of elevation is almost mesokurtic, solar radiation, Sx and in particular curvature are platykurtic distributed.

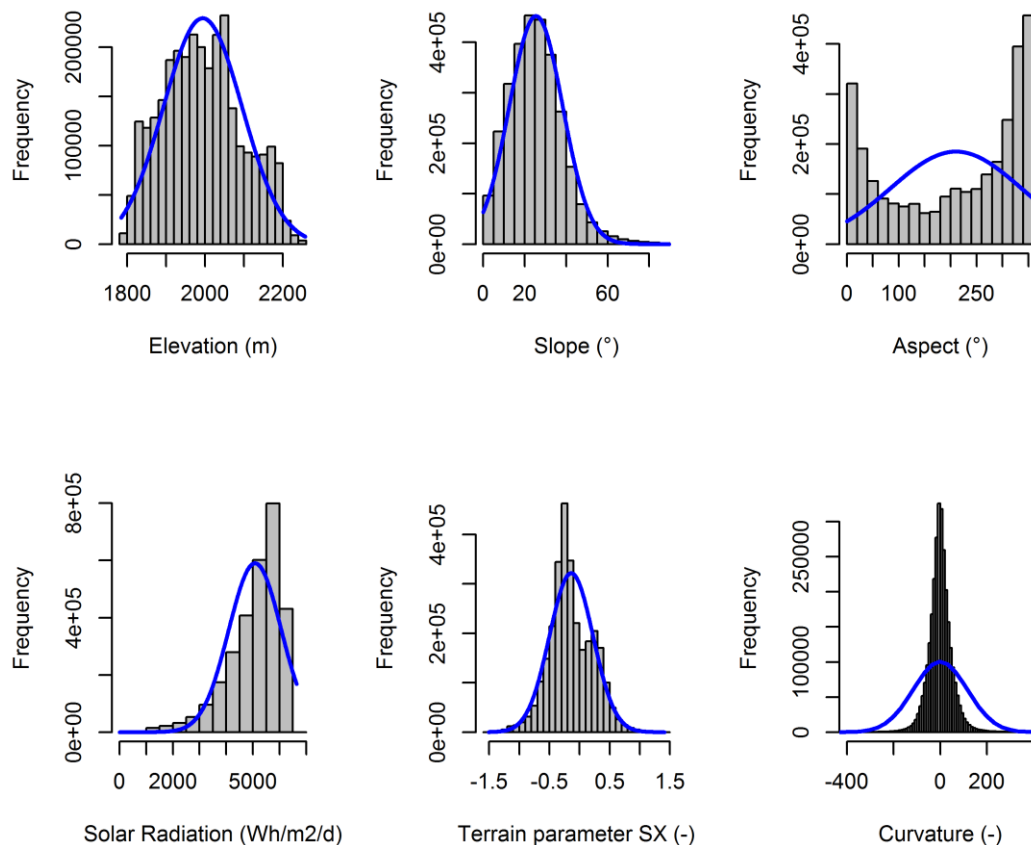


Figure 3.20: Histogram for each explanatory variable at the study site with normal curve with the corresponding mean and standard deviation.

Table 3.12: Statistics (minimum, maximum, mean, median (50%), 25% and 75% quantile) about explanatory variables at study site (1 m resolution).

Parameter	min	max	mean	median	25%	75%
Elevation [m]	1784.28	2257.40	1994.13	1989.52	1916.29	2060.10
Slope [°]	0	90	25.5	24.7	16.2	33.2
Aspect [°]	0	360	210	251	80	327
Solar radiation [Wh m ⁻² d ⁻¹]	2	6640	5081	5330	4578	5828
Terrain parameter Sx [-]	-1.51	1.41	-0.08	-0.19	-0.23	0
Curvature [-]	-17227	161856	-2e-10	-0.77	-26.62	25.93

Table 3.13: Skewness and kurtosis of explanatory variables and HS (1m resolution).

Parameter	Skewness	Kurtosis
Elevation [m]	0.20	2.28
Slope [°]	0.70	4.12
Aspect [°]	-0.43	1.62
Solar radiation [Wh m ⁻² d ⁻¹]	-1.30	4.80
Terrain parameter Sx [-]	-0.40	5.23
Curvature [-]	-0.73	2301
HS [m] Jun 28 2019	1.67	6.52
HS [m] Jul 10 2019	1.60	5.87
HS [m] Jul 17 2019	1.51	5.40
HS [m] Jun 24 2019	1.29	3.99

Figure 3.21 visualizes the positively skewed HS distributions of each survey. The x-axis is adjusted to each survey's maximum HS. This leads to violations of the assumption of residual normality in linear analyses assessing the strength of the relationship between predictors and calculated HS based on the difference DSMs. With a square root transformation of snow depth, as applied by Winstral et al. (2002) for manually sampled HS, the residual normality could not be achieved either. Also, with other transformations the requirement could not be fulfilled for which reason the non-transformed snow depth values were included in the model as input data.

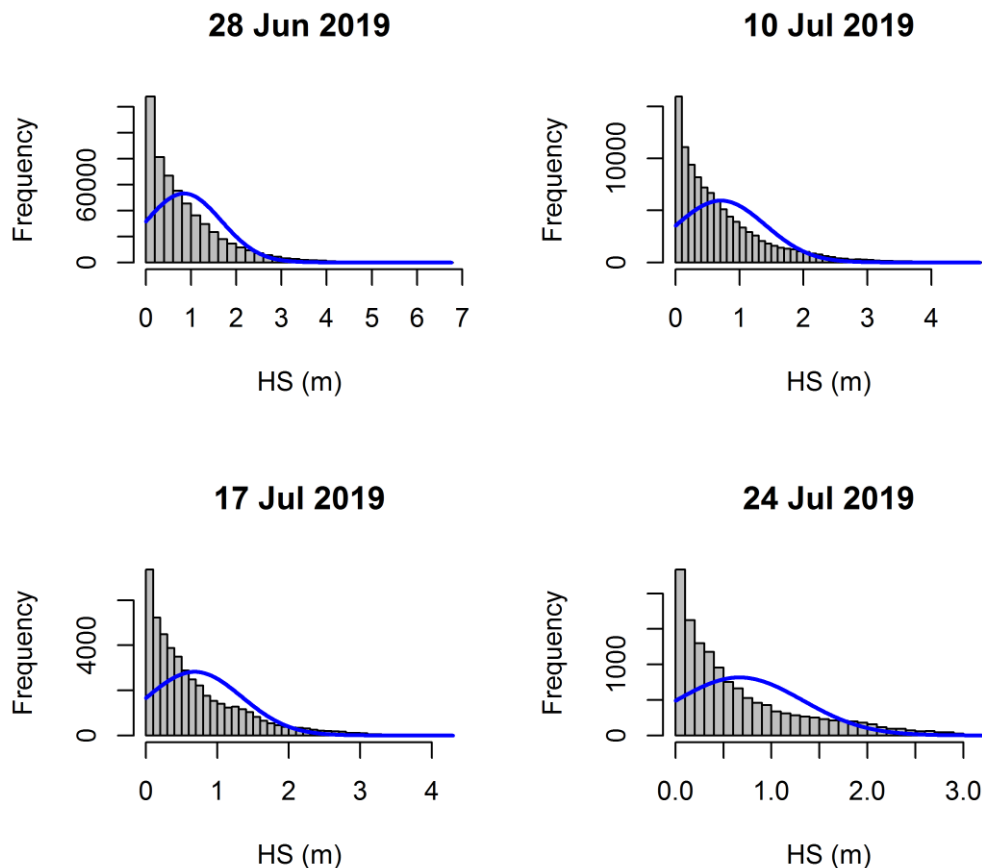


Figure 3.21: Histogram of HS at the study site for each survey with normal curve with the corresponding mean and standard deviation.

3.6.1.2 Correlations between explanatory parameters and response variable HS

With the information about which predictor variable correlates strongest with HS/snow cover, the multiple regression models were built stepwise and controlled for their predictive power. Figure 3.22 shows the correlation matrices of HS with the predictor variables for the four days of survey. The areas of circles show the absolute value of corresponding Pearson's correlation coefficients. Obviously, HS positively correlates most with the terrain parameter S_x and elevation. The correlation decreases with declining snow cover. However, with the greatest correlation coefficient of 0.24 between HS and S_x this relation should be interpreted with caution. Only the predictor variables *slope* and *radiation* as well as *aspect* and S_x feature strong negative correlations among each other. Downscaling the resolution to 10 m did not result in greater correlation coefficients as can be related from Figure A2 in the Appendix.

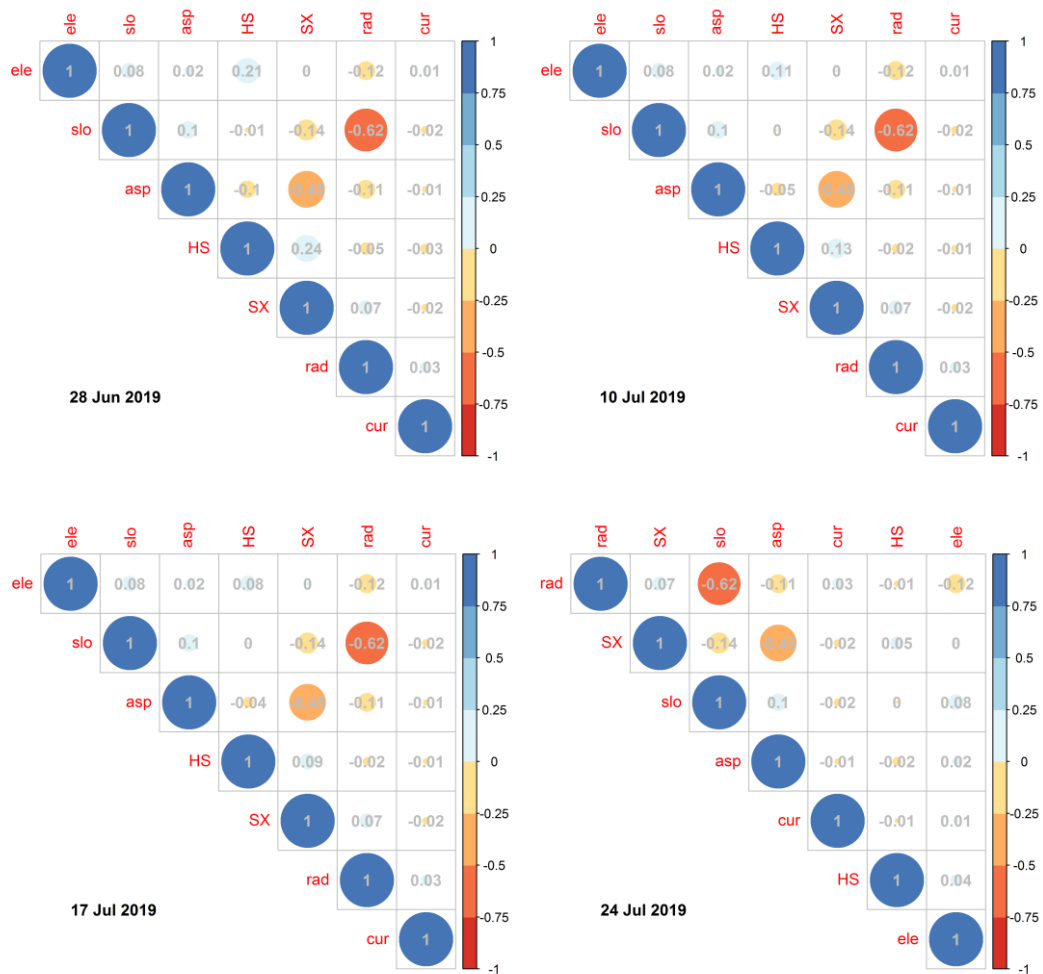


Figure 3.22: Correlation plot with correlation coefficients of dependent variable HS with predictor variables for the four UAS surveys (1m resolution).

For the reason that Pearson's correlation coefficient cannot be calculated for continuous-dichotomous data, a biserial correlation had to be performed to estimate the correlations between the explanatory variables and the categorical data *snow-free/snow-covered*. Similar to the Pearson coefficient, the point biserial correlation coefficients range from -1 to +1. The biserial correlation assumes normal distribution and homoscedasticity of the continuous variable. Table 3.14 lists the resulting correlation coefficients with the two strongest correlated coefficients marked in green.

Table 3.14: Correlation coefficients of biserial correlation between categorical *snow-free/ snow-covered* data and continuous explanatory variables.

	Elevation	Slope	Aspect	Radiation	Sx	Curvature
Jun 28 2019	-0.28	0.03	0.11	0.04	-0.29	0.03
Jul 10 2019	-0.16	0.00	0.07	0.02	-0.16	0.02
Jul 17 2019	-0.11	0.00	0.05	0.02	-0.11	0.01
Jul 24 2019	-0.06	0.00	0.03	0.01	-0.06	0.01

For the predictor variables and the dependent categorical variable *snow-covered/snow-free* the similar pattern (as for dependent continuous *HS*) of decreasing correlation coefficients with declining snow cover can be stated, as Figure 3.23 demonstrates. Overall, the correlation coefficients of *Sx* and *elevation* are slightly higher. With a maximum positive correlation of 0.29 between *snow-covered/snow-free* and *Sx*, this relation should also be interpreted with caution.

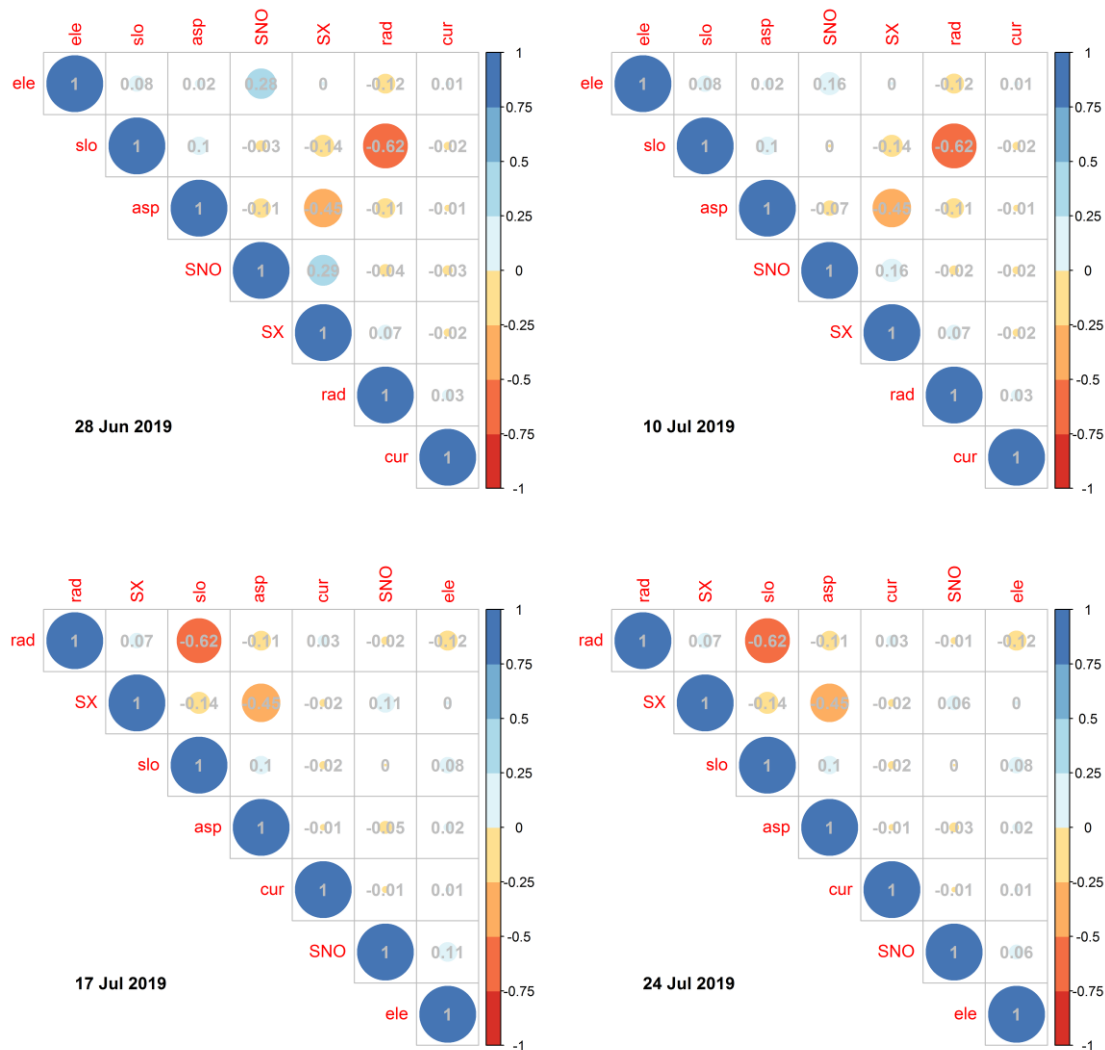


Figure 3.23: Correlation plot with correlation coefficients of dependent variable *snow-covered/snow-free* with predictor variables for the four UAS surveys (1m resolution).

3.6.1.3 Principal component analysis

Possible multicollinearity of the predictor variables was tested with *Principal Component Analysis* (PCA) to reduce the amount of regression parameters on the minimal necessary number.

Collinearity causes two problems:

1. Difficult to tell which variable is important, when two are very similar, and
2. *instable estimates* which means that the optimization algorithm in the regression has more difficulties in finding the optimum (Dormann, 2013).

These problems lead to greater standard errors of the GLM, also known as *variance inflation* (Dormann, 2013). To solve the issue of variance inflation, variables with collinearity must be found and thereof one must be excluded from the regression model.

In the PCA, the correlation of each variable with the other is listed and Pearson's correlation coefficient calculated. The PCA is applied on the correlation matrix and due to standardization not affected by the different ranges of the variables. However, the PCA only works with continuous variables or strictly with multivariate-normal distributed variables (Dormann, 2013). Since the variable *aspect* did not fulfil the latter requirement before and after transformation, and potentially showed collinearity with the parameter *Sx*, it was excluded from the PCA.

Figure 3.24 represents the scree plot, or rather the plot of eigenvalues ordered from the largest to the smallest. According to the plot the first four principal components explain 93% of the variance. Since 90% of explained variance are enough to build a regression model, the fifth principal component (PC) can be neglected. Table 3.15 lists the rotation matrix of the PCA. It can be judged that *radiation* can be excluded from the data set because the variables *radiation* and *slope* both load in the same magnitude on PC1. The variables that load most on the remaining PCs are *curvature*, *elevation* and the *terrain parameter Sx*.

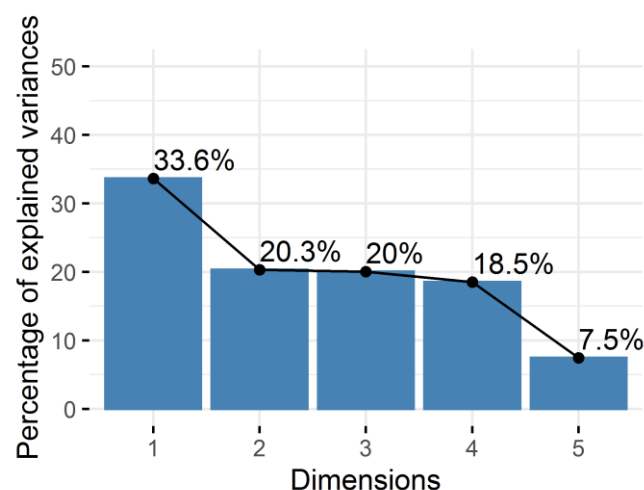


Figure 3.24: Scree plot of the principal components.

Table 3.15: Rotation matrix of the PCA.

	PC1	PC2	PC3	PC4	PC5
Elevation	-0.19	-0.36	0.69	0.60	0.04
Slope	-0.68	0.03	-0.06	-0.18	0.71
Radiation	0.67	0.09	0.00	0.22	0.70
Sx	0.21	-0.65	0.29	-0.66	0.08
Curvature	0.05	0.66	0.66	-0.35	-0.02

Figure 3.25 illustrates the square cosine \cos^2 , the quality of representation of the variables, on the factor map. A high \cos^2 indicates a good representation of the variable on the PC while a low \cos^2 indicates that the variable is not perfectly represented by the PCs. In other words, the factor map tells us that PC1 and PC2 explain together 54% of the variance with *slope* and *radiation* loading greatly on PC1 and *curvature* and *Sx* loading moderately on PC2.

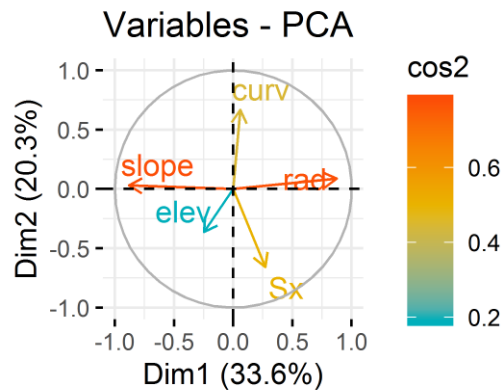


Figure 3.25: Quality of representation of the explanatory variables on the first two principal components.

3.6.2 Multiple linear regression models

With the investigated explanatory topographic variables, the distribution of the three different response variables *snow*, *snow depth* and *ablation* within the catchment was modeled by applying multiple regression models. The findings of the statistical preliminary investigation yielded strong correlations of only the wind sheltering parameter *Sx* and *elevation* with either *snow* or *HS*. Hence it can be assumed that those parameters alone are sufficient for the multiple regression model. According to the PCA, the first four PCs are necessary to explain at least 90% of the variance. For comparison, the regression models were also performed adding the parameters *slope* and *curvature*. The resulting predictive power of the regression models were in each case slightly worse for which reason only the model results with the regression parameters *Sx* and *elevation* will be presented. The results focus on the survey of June 28th,

2019, since the predictive power was in each case best for this survey compared to the recorded data of July 10th, 17th and 24th, 2019. For further information, the respective results can be found in the Appendix as Figures A3, A4, A7.

3.6.2.1 Modeling of snow-covered and snow-free areas

A typical representative of right-skewed distributions, such as in the case of HS, is the Bernoulli-distribution. The GLM was built with the binomial distributed dependent variable *snow-covered/snow-free*. Figure 3.26 illustrates the recorded SCA in comparison with the modeled SCA for June 28th, 2019. For the latter, the probability of snow is represented. It can be noticed that the GLM with the regression parameters *Sx* and *elevation* predicts snow especially in wind-shielded and high elevated areas. In the majority the areas of predicted snow fall within the boundaries of the snow polygons. Seldom snow is predicted with a high probability in areas outside those boundaries. Although the GLM is able to predict this characteristic pattern of snow cover, it only predicts it well for high elevated areas within the study site. Therefore, it has to be concluded that the GLM is of limited suitability for HS prediction within the whole study site. The model equation can be written as follows:

$$Snow = -17.07 + 2.30 * Sx + 0.01 * Elevation \quad (7)$$

According to the GLM summary, the *p-values* of the regression beta coefficient estimates are $< 2.2e-16$. This means, that at all predictor variables are highly significant related to the outcome variable. According to Sullivan and Feinn (2012), a statistical test will always demonstrate a significant difference with a sufficiently large sample. For this reason, *p-values* are considered to be confounded because of their dependence on sample size. Sometimes a statistically significant result means only that a huge sample size was used, as done in this analysis.

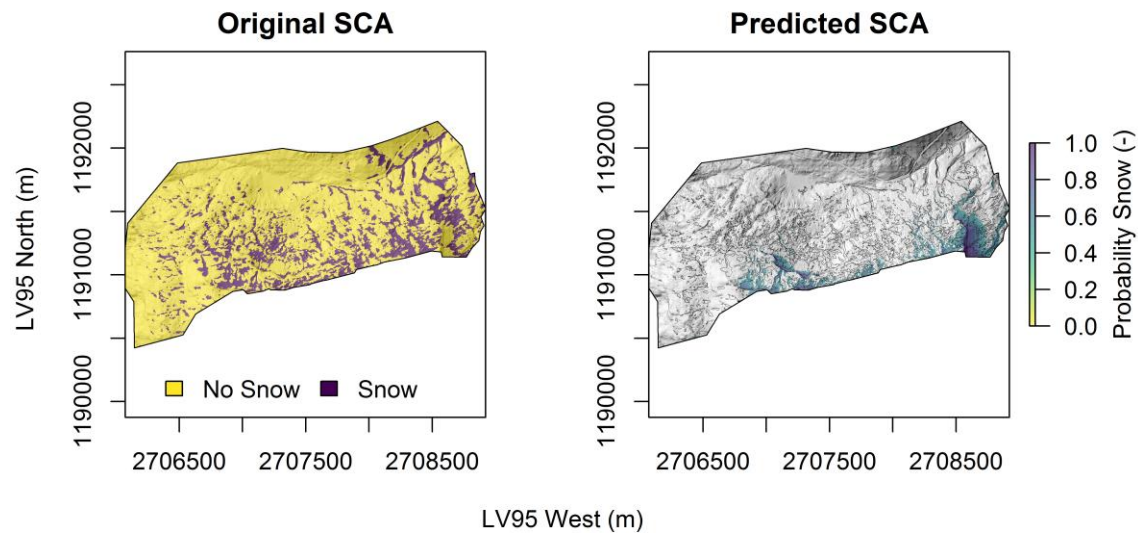


Figure 3.26: GLM output for Snow Cover Extent of June 28th, 2019. Original (left) and predicted (right) SCA. As predatory variables were used S_x and elevation.

Often, the residual-analysis is used as model diagnosis. It tells whether the assumptions regarding the relation between variance and mean apply. However, in the case of Bernoulli-distributed data, the residual-analysis cannot be used for model-diagnosis (Dormann, 2013). Since the GLM output does not give information about the overall quality of the model the *Residual Standard Error* (RSE) was calculated as measure of error of prediction. The lower the RSE, the more accurate the model. The error rate is estimated by dividing the RSE by the mean outcome variable. In this multiple regression example, the RSE is 0.92 corresponding to a 444% error rate.

In addition to the 1 m resolution GLM, the data was resampled to 10 m to compare the model accuracy. Here, the lowest RSE (i.e., 1.01) could be achieved with the regression parameters S_x , *elevation*, *slope*, *radiation* and *curvature*. The error rate is 254%. Consequently, the model accuracy of 1m resolution is higher than that of 10 m. This finding however is not in line with the visual model accuracy assessment since the predicted snow cover pattern of the 1 m resolution GLM seems to be less accurate towards the original record of June 28th, 2019 than the 10 m resolution GLM as the Figures 3.26 and 3.27 demonstrate.

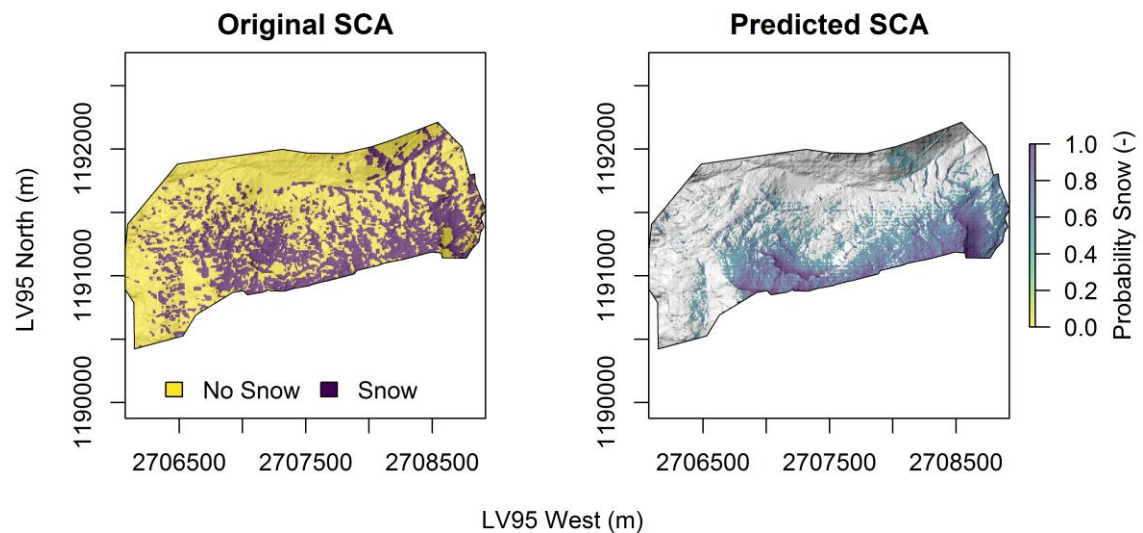


Figure 3.27: GLM output for Snow Cover Extent of June 28th, 2019. Original (left) and predicted (right) SCA. As predictive variables were used *Sx*, elevation, slope, radiation and curvature (10 m resolution).

In order to test whether the information gained by satellite is as sufficient as the UAS data (recorded and resampled to equal resolution of 10 m) a GLM was build based on the SCA estimation from the SENTINEL-2 record of June 29th, 2019 (one day after the first UAS mission). Just as for the recorded data, the highest model accuracy (RSE of 0.99) could be achieved with the regression parameters *Sx*, *elevation*, *slope*, *radiation* and *curvature*. The error rate is 216%. This allows for the conclusion, that the snow cover information retrieved from satellite data to predict SCA is likewise convenient as self-recorded resampled high-resolution UAS data, as the visual comparison of Figure 3.27 and 3.28 shows.

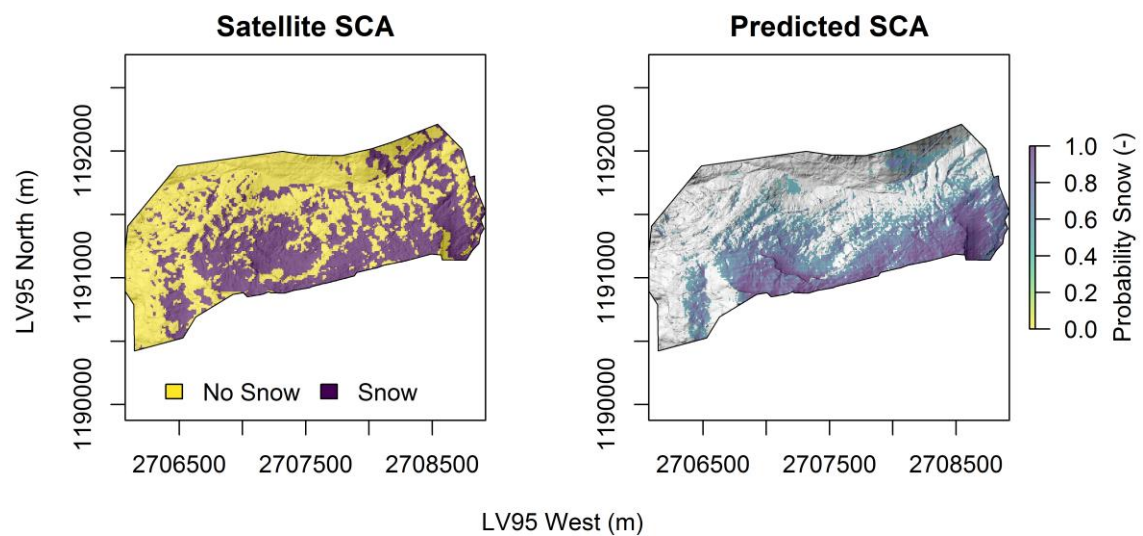


Figure 3.28: GLM output for Snow Cover Extent of June 29th, 2019. Satellite record (left) and predicted (right) SCA. As predictive variables were used *Sx*, elevation, slope, radiation and curvature (10 m resolution).

3.6.2.2 Modeling of snow depth

Figure 3.29 represents the result of the multiple linear regression with Sx and *elevation*, as predictor variables. The model equation can be written as follows:

$$HS = -1.83 + 0.33 * Sx + 0.001 * Elevation \quad (8)$$

Performing the LM adding the parameters *slope* and *curvature* did not score a higher performance. The quality of the predictive power of the MLR was assessed by the R^2 . The R^2 represents the correlation coefficient between the observed values of the output variable and the fitted values. It ranges from 0 to 1. R^2 represents the proportion of variance, in the output variable, that may be predicted by knowing the value of the explanatory variables. A value of close to one indicates that the model explains a large portion of the variance in the outcome variable. A problem with R^2 is that it increases the more variables are added to the model, even if those variables are only weakly associated with the response. A solution is to adjust the R^2 by taking into account the number of predictor variables. The adjustment is the so-called *Adjusted R^2* . The *Adjusted R^2* in the summary output is a correction for the number of explanatory variables included in the prediction model. The *Adjusted R^2* was 0.10 with an RSE of 0.47. The error rate is 287%. The residual analysis could show that the primary assumption of LMs (normal distribution of the residuals) was violated, as the Q-Q Plot in Figure A6 (Appendix) illustrates. The inspection of the HS residuals versus the fitted values of the LM, however, yielded a more or less equal deviation within the total range of the fitted values from the observed values and thus no striking pattern could be observed.

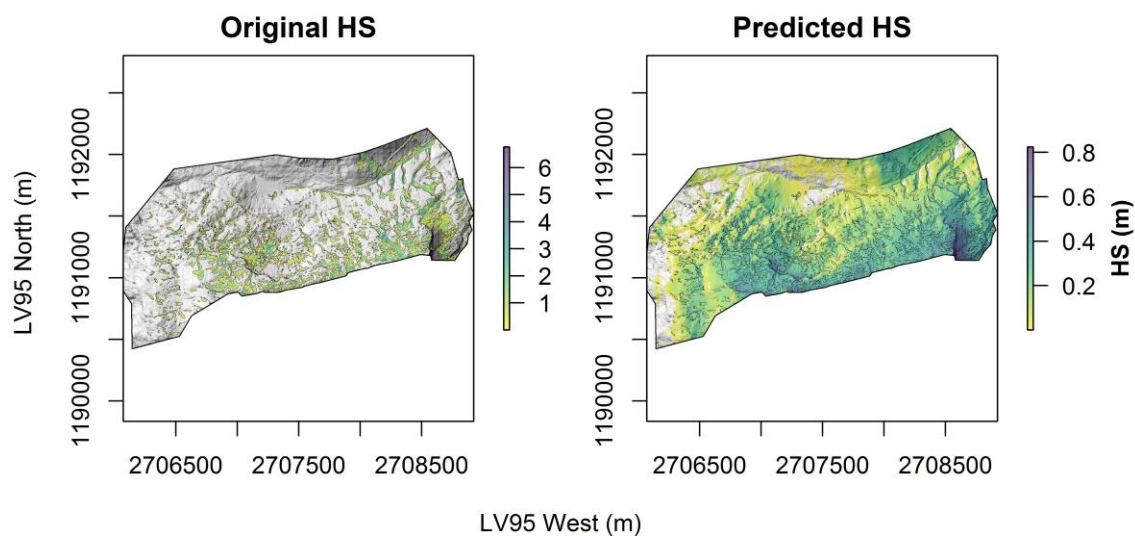


Figure 3.29: LM output for Snow depth of June 28th, 2019. Original (left) and predicted (right) SCA. As predictor variables were used Sx and elevation.

In comparison to the GLM outcome of snow-covered/snow-free areas, the LM predicts snow in most areas within the study side. Only in the lowermost elevated areas no snow existence is predicted. According to the continuous scale of HS, the prediction of greater HS focuses on wind-sheltered areas. In comparison to the GLM outcome, the prediction of snow existence does not concentrate on the highest elevations because in lower elevated areas great HS are simulated, as well. At large, the prediction of absolutely correct HS is rather imprecise (original versus predicted maximum HS almost 7 m versus 1 m), while the predicted HS, with only the two regression parameters *Sx* and *elevation* used, matches to a certain extent with the recorded HS pattern. Still, the prediction deviates far from being as precise as the observation data of 1 m resolution.

3.6.2.3 Modeling of ablation

The main predictor for ablation over a certain period is the solar radiation budget. For the prediction of ablation between the UAS surveys solar radiation budget was assumed to be an important predictor variable. Therefore, the solar radiation budget was calculated for the periods between the consecutive UAS surveys. Since solar radiation has the unit of Watt hours per square meter (Wh m^{-2}) and the periods between the flights had different lengths, solar radiation was standardized by dividing through the amount of days between the flights. This made the radiation raster maps comparable with each other. As Figure 3.30 demonstrates, the daily radiation amounts show only marginal differences between the periods of interest.

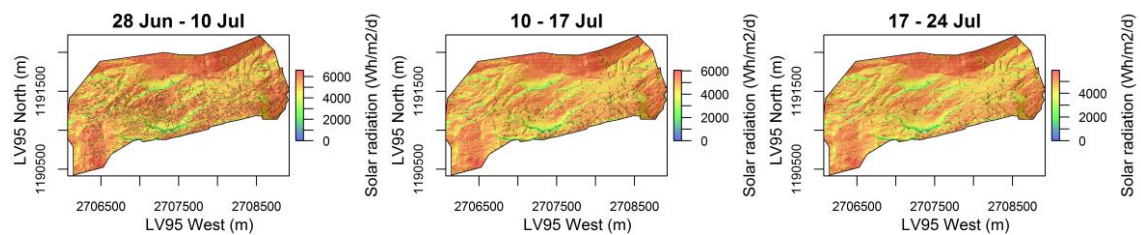


Figure 3.30: Solar radiation maps ($\text{Wh m}^{-2} \text{d}^{-1}$) on hill shade with polygons of snow cover extent. Snow cover extent of June 28th, for period from June 28th to July 10th, snow cover extent of July 10th for period from July 10th to 17th and snow cover extent of July 17th for period from July 17th to 24th.

Although solar radiation can be assumed as main predictor for snowmelt, a simple regression with only *radiation* as predictor variable has not proven to be an appropriate way to model ablation between the single UAS surveys. The best result could be achieved by using *radiation*, *Sx* and *elevation*, as predictor variables. Figure 3.31 represents the result of the MLR. The model equation can be written as follows:

$$\text{Ablation} = -135 - 0.00002 * \text{Radiation} + 0.076 * \text{Elevation} + 24.89 * Sx \quad (9)$$

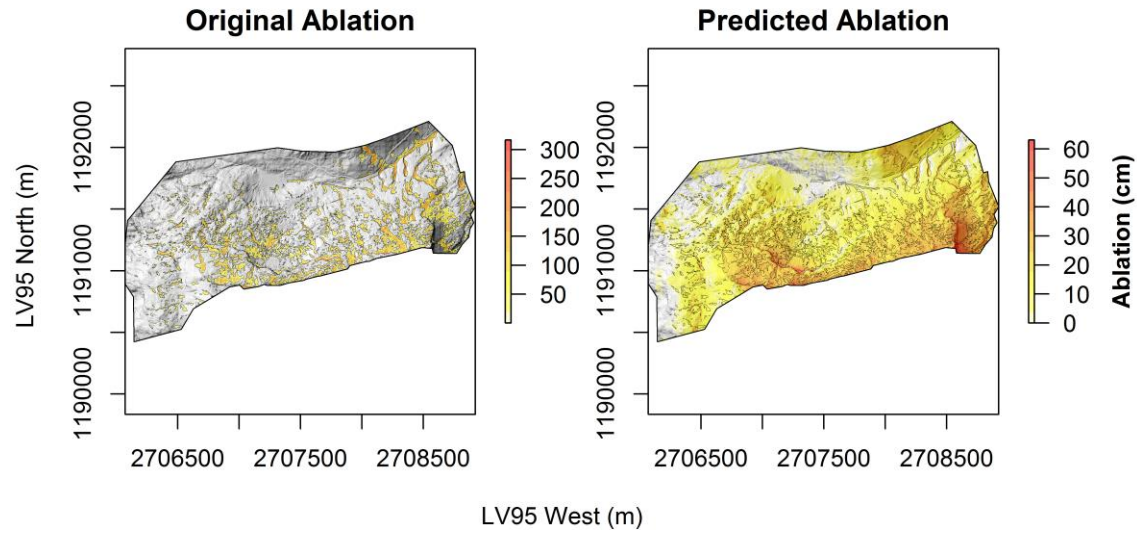


Figure 3.31: LM output for Ablation of between June 28th and July 10th, 2019. Original (left) and predicted (right) ablation. As predictor variables were used radiation, Sx and elevation.

Performing the LM adding the parameters *slope* and *curvature* did not score a higher performance. The adjusted R^2 of the multiple linear regression was 0.11 with an RSE of 34.33. The error rate is 264%. With a modeled ablation maximum of about 60 cm the LM result is clearly underestimating the recorded ablation. As the regression parameter *ablation* does not explain much of the variance of the data, the predictive force of the LM was only slightly improved compared to a regression with only Sx and *elevation*. Therefore, the predicted pattern is quite comparable to that of HS (Figure 3.29). As for the prediction of HS, the residual analysis could show that the primary assumption of LMs (normal distribution of the residuals) was violated, as the Q-Q Plot in Figure A8 (Appendix) illustrates. The inspection of the *ablation* residuals versus the fitted values of the LM, however, yielded a more or less equal deviation within the total range of the fitted values from the observed values and thus no striking pattern could be observed.

The model predicts greater total ablation in higher altitude. This is not in line with the certainty that temperature decreases with elevation, a condition not implemented in the model. Thus, the observed phenomena of higher ablation with increasing elevation arises from the generally smaller HS in lower altitude not allowing for great total ablation quantities within the period of interest. Greatest ablation amounts are predicted in rather high elevated and easterly exposed areas. According to the assumptions of the parameter Sx , those are sections not exposed to wind. This allows for great snow accumulation. The comparison of original and predicted ablation in such areas however shows that both diverge (Figure 3.31).

3.6.3 Differences between snow-free and snow-covered areas

3.6.3.1 Empirical cumulative density functions

To understand, whether the topographic parameters of areas, where snow exists and snow does not exist, are different and whether that difference is significant, the data was split into groups. The following graphs illustrate the *empirical cumulative density function* (ECDF) of specific parameters for the study area and snow-covered or snow-free pixels. Some specific parameters show clear differences in the cumulative distribution while others do not.

Figures 3.32–3.35 show the characteristic ECDFs of each predictor variable for the four UAS surveys (1 m resolution data). The *x-axis* was adjusted to stress the differences between the distributions of snow-covered, snow-free and the whole study site. The graphs show that snow remains in higher altitudes and in likely avalanche accumulation areas (slopes between 20 and 30 degrees). Snow-free areas are mostly in southerly aspects while snow especially remains in rather northerly aspects (325–75°). This is in line with the finding that areas with snow cover feature smaller solar radiation amounts. Wind shelter parameter values smaller zero represent areas exposed to wind. From the graphs one may conclude that snow can favorably be found in areas with low wind exposure. That snow shows a tendency to remain in concave areas (curvature values below zero), is another information that emerges from the analysis. While for the June 28th the ECDF of the snow-covered and especially the snow-free deviate not much from the ECDF of the whole study site, the deviation becomes clearer with proceeding ablation, as the consecutive graphs show.

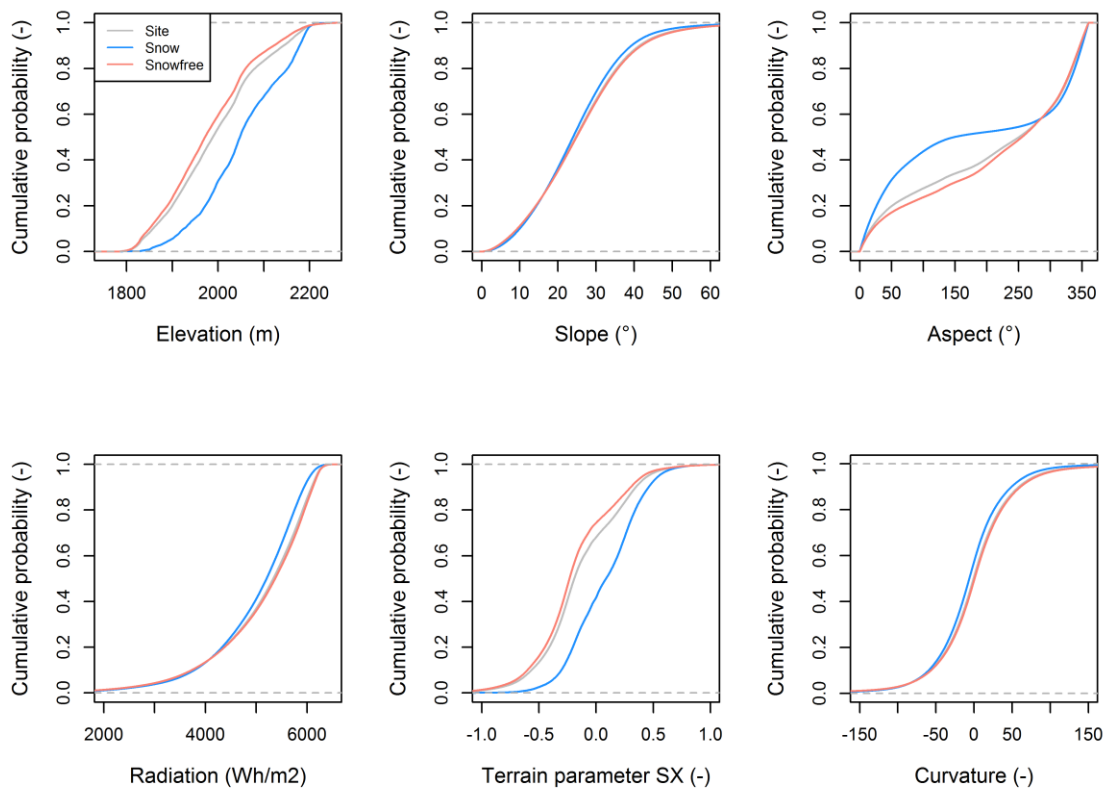


Figure 3.32: ECDF of each predictor variable for June 28th, 2019 (1 m resolution).

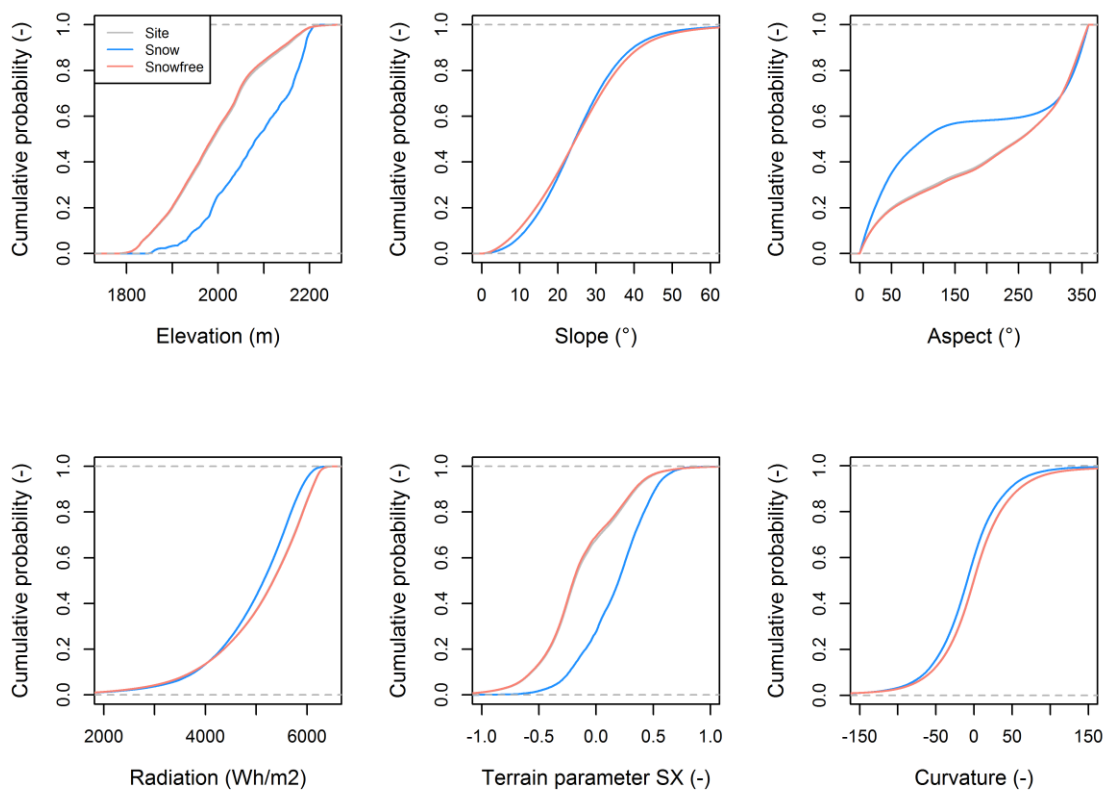


Figure 3.33: ECDF of each predictor variable for July 10th, 2019 (1 m resolution).

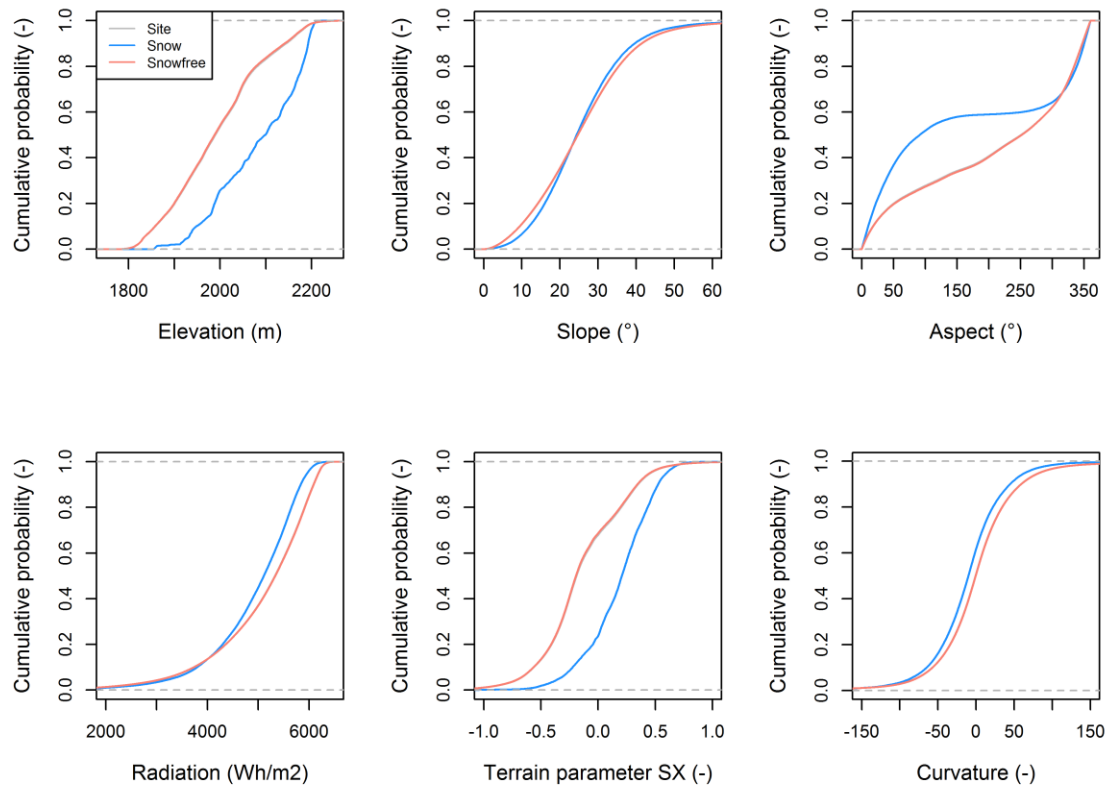


Figure 3.34: ECDF of each predictor variable for July 17th, 2019 (1 m resolution).

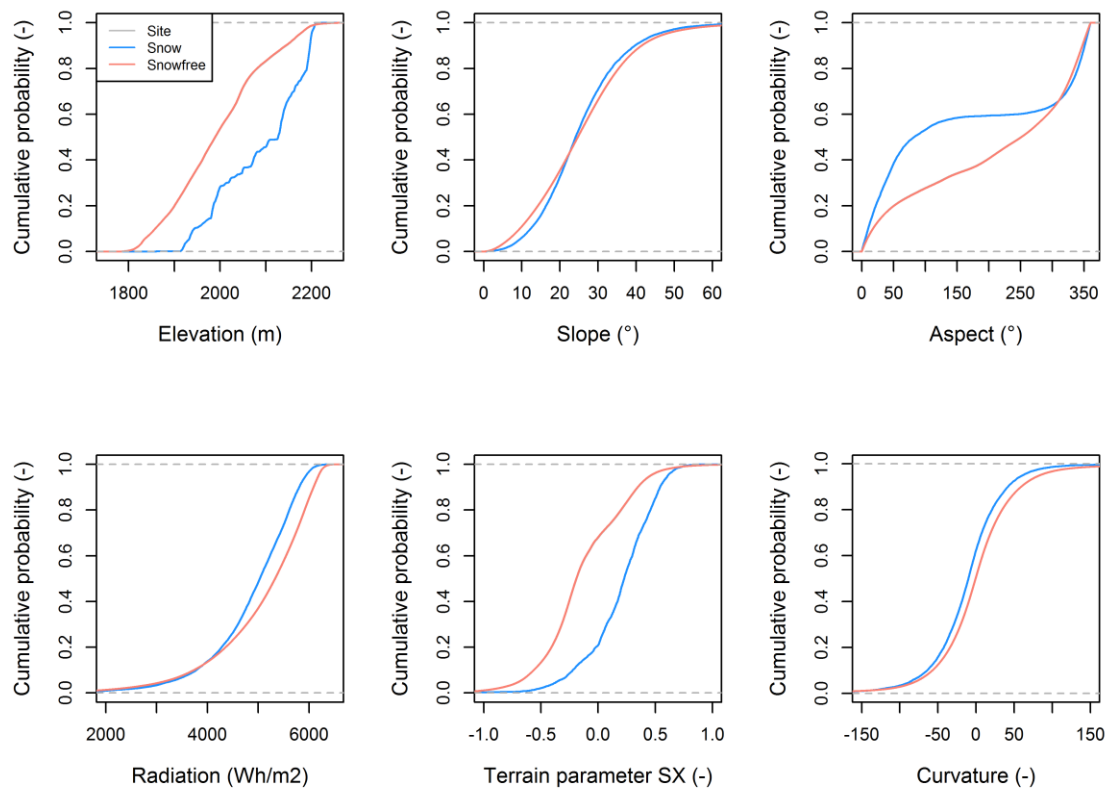


Figure 3.35: ECDF of each predictor variable for July 24th, 2019 (1 m resolution).

3.6.3.2 Effect size

As a further distinctive parameter to test whether the two biserial data groups are significantly different from each other, Cohen's d was calculated. Unlike significance tests, such as ANOVA, effect size is independent of sample size (Sullivan and Feinn, 2012) for which reason Cohen's d suits well to test for statistical significant difference. As already described in chapter 2.4.3.3, Cohen's d expresses the effect size where values above 0.8 describe a strong effect size. Because Cohen's d requires two different data groups, each predictor variable was split into the raster pixels where snow was present and where snow was not present to receive a dichotomous dataset. Subsequently, Cohen's d was calculated for each of the four UAS surveys. Table 3.16 lists the resulting effect sizes of each explanatory variable for the four days of record. While the parameters *slope*, *curvature* and *radiation* hold not even a small effect size, *aspect* holds a small effect size and *elevation* and the wind sheltering parameter *Sx* a big effect size. Consequently, only the latter two parameters hold a significant difference between snow-covered and snow-free areas for the last three UAS surveys.

Table 3.16: Effect size of each predictory variable for the four UAV surveys(1m resolution). Strong effect size is marked in green.

	Elevation	Slope	Aspect	Radiation	Sx	Curvature
Jun 28 2019	0.73	0.08	0.27	0.13	0.74	0.06
Jul 10 2019	0.87	0.00	0.36	0.15	0.87	0.09
Jul 17 2019	0.90	0.01	0.38	0.15	0.90	0.09
Jul 24 2019	0.94	0.02	0.39	0.18	0.93	0.10

3.6.3.3 Areas of first snowmelt

Figure 3.36 shows the characteristic distributions for June 19th, 2019, the first cloud-free SENTINEL-2 image where first parts of the snow cover are melted to ground. This gives information about at which locations snow melts earliest and where it most likely persists the longest at the study site. If not for all parameters, the figure shows similar tendencies as the analysis of the UAS surveys. This sometimes not clear deviation results from the greater snow cover earlier in the season.

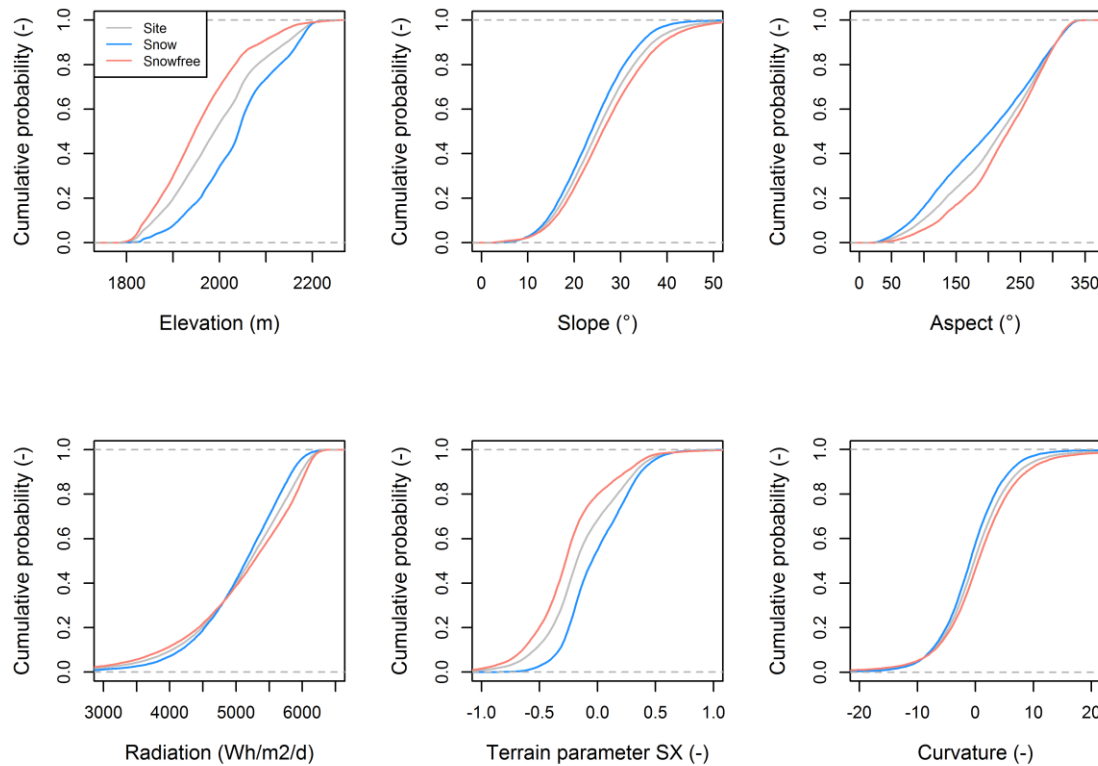


Figure 3.36: 10 m resolution NDSI June 19th, 2019 (threshold 0.42). Day where first areas of snow cover were melted to ground. Cumulative density function of each predictor variable. X-axis adjusted to illustrate the shift better. Comparison of the distribution of each parameter for the whole site and for only snow pixels.

As additional quantitative information about the deviation of the ECDFs, Table 3.17 lists the quantiles of each parameter distribution for the whole study site with the corresponding deviance of snow-covered and snow-free areas. From a positive shift of 51 m in the 50% quantile it can be concluded that snow remains in higher altitudes. The table also shows that the 75% radiation quantiles of snow-covered and snow-free areas differ by 240 WH m⁻² d⁻¹, confirming that solar radiation drives snowmelt.

Table 3.17: 25, 50 and 75% quantiles of parameters of interest for the whole study site. For snow-covered and snow-free areas the deviance to the study site is listed (green = positive shift).

Parameter	Site			Quantile deviance towards whole study site					
	25%	50%	75%	Snow			Snow-free		
	25%	50%	75%	25%	50%	75%	25%	50%	75%
Elevation [m]	1916	1989	2060	54.7	51.0	45.3	-30.3	-43.3	-44.7
Slope [°]	19.1	24.9	31.2	-1.0	-1.2	-1.8	1.0	1.2	1.7
Aspect [°]	151.3	220.1	274.2	-26.8	-17.1	-4.8	29.4	11.0	3.4
Radiation [Wh m ⁻² d ⁻¹]	4633	5208	5699	23.1	-59.2	-121.8	-25.0	67.6	120.7
Sx [-]	-0.34	-0.18	0.09	0.13	0.13	0.11	0.22	0.05	-0.21
Curvature [-]	-3.67	-0.20	3.48	-0.49	-0.70	-1.01	0.51	0.69	0.95

Although some shifts might appear large, there can only be detected a significant difference between snow-covered and snow-free areas in the parameter elevation, as the large effect size demonstrates (Table 3.18). The wind shelter parameter holds medium effect size while aspect, slope and curvature hold a small effect size. The overall values of solar radiation between the two groups seem not to differ at all.

Table 3.18: Effect size of each predictory variable for the NDSI of June 19th, 2019 (10 m resolution). Strong effect size is marked in green.

	Elevation	Slope	Aspect	Radiation	Sx	Curvature
Jun 17 2019	0.88	0.33	0.35	0.05	0.75	0.20

4 Discussion

a. Accuracy of recorded data and challenges in UAV-based mapping of snow depth

The hypothesis that *UAS serve to deliver valuable spatiotemporal HS data on a catchment scale for snow-hydrological modeling* was successfully supported with the acquired data. With the *non-RTK eBee Classic* and the *Trimble R7 GPS Receiver*, five high-resolution orthophotos (7.5 cm) and DSMs (15 cm) could be processed with horizontal and vertical accuracies better than 12 cm and 14 cm, according to the RMSE for the GCPs (Table 3.1). However, an added model accuracy assessment showed that the *snow-covered* DSMs (1–4) had locally different accuracies in z direction in comparison to the *snow-free* reference DSM (5). The DSMs were considered inappropriate for a HS determination on a large scale, although the calculated total mean deviations in respect to the reference DSM of maximum 15 cm in the vertical direction (Table 3.6) indicated an acceptable accuracy. The distribution of DSM errors for the snow-free DSM was spatially not heterogeneous (Figure 3.7). This elevation measurement bias occurred outside of the areas enclosed by the GCPs, particularly at the edges of the study site where image overlap was lower and vertical difference of the earth's surface and take-off location was rather high. Still, this error was only considerably high for surveys 2 and 3 with high elevation errors predominantly in the southwestern region of the study site. This co-registration error, in turn, was related to finding snow-free areas that were not confounded by real changes to the surface, such as vegetative compression, frost heave, or erosion, as described by Nolan et al. (2015). By applying a Median filter of 3 m on the snow-free deviation raster of surveys 1–4 (Figure 3.7), the surface of the original DSMs was corrected for every raster cell by its specific local deviation. This removed local inaccuracies and enabled the precise determination of HS within the whole study site by subtracting the *snow-free* reference DSM from the *snow-covered* DSMs.

With the suitable GCPs in *snow-free* terrain, the accuracy of the HS maps was effectively improved to the level of precision of the generated DSMs, thus between 7.5 and 22.5 cm (1–3x GSD). The achieved DSM-accuracies in this study are in line with those of Lee et al. (2008) but higher than those achieved by Vander Jagt et al. (2015). Although the RMSE of the modeled and probed HS is not better than 0.62, this value can at most only be considered as an approximation for determining the HS accuracy. This is because no dGNSS was available to locate the manual probe measurements with utmost precision, not allowing for a precise validation of the processed HS. Instead, manual measurements were recorded with a GPS of 10 m accuracy, which produced a mean underestimation of the processed HS between 27 and 47 cm⁴, depending on the survey. The determined accuracy of the DSMs (7.5–22.5 cm) rather represents the accuracy of the modeled HS. Consequently, the error of prediction has to be

⁴ Bühler et al., 2016 report 20 cm.

considered as low, and the HS mapping results are of high precision on a large scale. Here, it is important to note the finding of Nolan et al. (2015) that in winter, compressed canopy can produce *negative* snow depths in the difference maps of up to 30 cm of error. Also in this study, the assumption that the differences between maps were caused only by snow accumulation has been violated in places where there was compressible vegetation. Still, the difference between snow-covered and snow-free DSMs results in a systematic underestimation of HS (Bühler et al., 2016).

It appeared that the inaccuracy increased with greater probed HS (Figure 3.12). For comparison, Goetz and Brenning (2019) and Redpath et al. (2018) report a RMSE of snow depth of 15 cm. Nolan et al. (2015) found a standard deviation between airborne manual HS measurements of around ± 0.1 m and thus also mapped HS more accurately. Harder et al. (2016) translate their DSM errors into mean snow depth errors of 8.5 cm. In contrast, the found relation between modeled and probed HS in this study is comparable to the results of Bühler et al. (2016), who report a RMSE of 30 cm for their estimated HS distribution.

With up to 3 cm, the horizontal accuracy is comparable to the one achieved by Harder et al. (2016) with 4.2 cm at an alpine site but lower compared to Goetz and Brenning (2019), with less than 2 cm. Overall, the DSMs have high repeatability as the consistent low geolocation offsets of the five surveys show (Figure 3.6).

Besides the inaccuracies of the positioning of the GPS, HS measurements with an avalanche probe bare further uncertainties. They can be distorted by the penetration of the snow cover not being exactly vertical (especially in deep snowpacks); by thick ice layers or by rough bedrock within the snowpack, which cannot be penetrated by the avalanche probe. They might even penetrate the first ground layers causing systematic overestimation of HS. Thus, the *real* HS most likely lies between the probe measurement and the modeled HS value.

On the whole, not many data sets are available with a horizontal sampling resolution higher than 1 m, as Michele et al. (2016) report. For this reason, these study results correspond to the latest scientific findings in HS mapping with UAS. While most of such studies focus on smaller areas ($< 1 \text{ km}^2$), rather flat terrain and capturing the peak of HS, this study was conducted over a rather large area ($\sim 3 \text{ km}^2$) with a high altitudinal range involving additional flight control challenges and error sources. By capturing the HS distribution of late seasonal snow patterns, this study brings rather novel information into the scientific context of airborne HS mapping. With the first UAS record, the remaining 20% of the snow cover within the study area was captured, and three subsequent flights recorded the depletion to almost 0% in a frequency of about one week between each survey. Based on the high-resolution HS maps and conducted snow density measurements (Table 3.10), detailed information about the SWE and successive ablation could be derived. The listed results, together with their corresponding precision, support the hypothesis that *UAS serve to deliver valuable spatiotemporal HS data on a catchment scale for snow-hydrological modeling* even though it must be limited to modeling

late-seasonal snowmelt. One can only assume that the results found are transferable for recording HS at its peak and utilizing the gained data for more precise modeling of snowmelt peak flow.

Besides the conducted model accuracy analysis and the given information, recall that DEMs are models of the Earth's surface and, therefore, always contain errors and uncertainties. Fisher and Tate (2006) name three categories for sources of errors in DEMs: (1) errors caused by the data acquisition method, (2) errors caused by the processing of the data, and (3) errors caused by the characteristics of the Earth's surface. Because most of these errors cannot be identified and quantified, they have to be treated as uncertainties (Bühler et al., 2012). The argument that older and more weathered surfaces are more suitable than fresh snow surfaces for structure-from-motion software to identify meaningful matching points (Bühler et al., 2016) indicates that recording the HS distribution of late seasonal snow patterns is likely to be associated with fewer errors than HS mapping of smooth snow surfaces earlier in the season, especially after fresh snowfall. However, with subsequent strong winds and large differences in radiation, those surfaces develop detectable features such as sastrugi or wind ripples (Bühler et al., 2016). The visual assessment of the snow surfaces of the generated high-resolution orthophotos and DSMs could, in both products, ascertain detailed snowmelt features, especially due to accretion of debris and dirt that cause a lower albedo of the snow surface and accelerated melt. Still, the orthophotos were not suitable for automatic discrimination between snow-covered and snow-free terrain due to the similarity of karst and snow pixel values. While the available RGB information of the raster image would have been sufficient to classify the snow cover automatically with high precision for a more extensive snow cover with most of the karst covered in snow, it was not the case for the recorded data. In this case, an area of karst that was too large apparently caused mistakes in the classification, which increased with ongoing ablation. The problem here was the inseparable high similarity of karst and snow pixel values. The applied pixel-based clustering algorithm focuses only on the spectral value of each pixel and often results in image speckle and overall inaccuracies when applied to high-resolution imagery (Kelly et al., 2004). This speckle, also known as the *salt-and-pepper effect*, is caused by high local spatial heterogeneity between neighboring pixels (Kelly et al., 2011), as in the case of dark dirt on the bright snow surface. Since each pixel is analyzed independently from its neighbors in the pixel-based paradigm, close neighbors often have different classes, despite being similar. As proposed by Kelly et al. (2011), a segment-based image analysis—in which the image is segmented into similar image objects first, and then the objects are classified based on attributes of and interrelations between the segmented objects to produce the discrete entities (e.g., snow-covered and snow-free terrain)—did not help to alleviate many of the aforementioned problems.

Another potential problem that occurred in some images during the UAS surveys was the reflections of the sun on the snow surface saturating the camera sensor. This generated large

areas of snow with the same pixel value (usually 255 in all bands = white) and complicated the SfM-process because few matching points could be found in the overlapping pictures. This overexposure, a higher light incidence than the sensor can absorb, makes it impossible for the algorithm to detect differences in the images and, consequently, to calculate structures. However, this problem can only be reported for a small fraction of snow cover within the study site. A further problem occurred in the camera settings with the shutter speed not set to *high* (1/2000) as default, for which reason a distortion of about 10 cm resulted from a flight speed of 30 m s^{-1} , also impeding the SfM process. Potentially, multiple launching and landing phases during one UAS survey, as necessary in this study to map the desired area, represent an error source because the camera automatically shuts down in the landing phase. With each launch, the aperture re-opens and camera calibration parameters have to be estimated again. However, this marginal difference described can induce potential problems in the SfM process, when using the same camera calibration parameters for all images captured in one UAS survey.

As snow absorbs more energy in the NIR part of the electromagnetic spectrum than in the visible region (Bühler et al., 2015), discrimination of snow and other terrain features is possible. NIR imagery also brings two substantial advantages for image matching on snow-covered areas: (1) less image saturation due to lower reflectance and (2) more contrast features due to variations in snow grain size (Eker et al., 2019). Since the recorded RGB images in this study do not allow for total discrimination of snow from karst pixels, the applied technique has to be considered inappropriate. With the method used, problems originated that would not have appeared with NIR records. This can be seen in the following example. Due to the inaccuracy of the eBee, especially for surveys 2 and 3, a high bias in relation to the reference was produced in the DSMs by the SfM software (Figure 3.7). To correct this bias, a correct mask of the snow was necessary to clip the snow-covered area and then calculate the deviation of snow-free areas to the reference DSM for each survey. In the next step, the clipped snowfields were interpolated. Subsequently, the closed deviation raster was subtracted from the original record, and a corrected survey with a deviation against zero in the snow-free areas in relation to the reference DSM was retrieved. Only this method guaranteed that a correction of the original snow surface could be applied and generated HS values were accurate in high-resolution. However, RGB did not allow for automatic discrimination, for which reason the snow mask was drawn manually with multiple polygons in *QGIS*, requiring immense user input. One can imagine that drawing polygons 100% accurate in 15 cm resolution would take forever, and, consequently, the result was only a good approximation. This brings mistakes in the interpolation of the snow surface for the reason that the interpolation *start values* (boundary areas of the snow-free sections) are not always exactly at the border to the snowfield (e.g., on top of a boulder, multiple centimeters to a meter away from the snow edge). Thus, locally incorrect elevation outcomes are a consequence to live with. This example emphasizes the need for a correct snow boundary layer to correct a DSM surface that eventually shows unacceptable

deviations from its reference DSM. This information could not be retrieved because images were not recorded in the near-infrared. For studies not addressing high-resolution HS information or studies eventually not dealing with high deviations between two DSMs, a manual polygon mask might be sufficient for surface correction or not even necessary. Still, NIR records are beneficial in that they also allow for precise SCA information, which is valuable information in snow-hydrological studies.

A comparison of SCA retrieved from both UAS and satellite data could determine an underestimation of the maximum recorded percentual snow cover extent at the study site by 9%. However, the absolute error was 42% and increased with ongoing ablation (Table 3.8, Table 3.9). This clarifies the strength of UAS data compared to satellite records to provide detailed SCA information on the catchment scale when such information is needed (e.g., calculating the remaining SWE in a high alpine watershed with existing hydropower generation).

b. Modeling of snow cover and snow depth distribution

This study also tested the hypothesis of whether *late seasonal HS distribution can be linked to topography*. Therefore, correlation coefficients between both HS (continuous) and snow-covered/snow-free (binomial) data and the variables elevation, slope, aspect, solar radiation, a wind shelter parameter S_x , and curvature were calculated. For this analysis, the recorded DSMs were resampled to 1 m resolution. The results indicate that not a single parameter showed either a high (>0.5) or moderate (>0.3) correlation with the snow distribution. The highest correlation coefficients of 0.24/0.29 were found between the parameter S_x and continuous/binomial snow information followed by the parameter elevation with 0.21/0.28. The estimated correlations between the remaining variables are not noteworthy. These findings are in line with other scientific findings. Winstral et al. (2002) found the parameter S_x to be a significant predictor, accounting for more of the variance in the observed HS than could be explained by elevation, solar radiation, or slope. Grünwald et al. (2013) found the parameters elevation gradient, slope, north-eastern aspect and a wind-sheltering index S_x the most frequent in several applied multiple regression models and thus consider those variables as good predictors of snow distribution. However, overall the results do not support the hypothesis that HS distribution can be clearly linked to topography.

Due to the minor correlations found, the conditions to build a multiple regression model with great predictive power were not optimal. Although the significance tests for linear regression stated a significant relationship between each explanatory parameter and the response variable HS or snow/no snow, the received model accuracies were very low with the highest adjusted R^2 of 0.11 (Figure 3.29, Figure 3.31). Because of an excessive number of observations that potentially led to false identification, the predictor variables were most likely declared to be statistically significant. A reduced data set (~1000 data points) could have avoided this problem. Large effect sizes, expressed in the term of Cohen's d , indicating a significant difference

between two data groups, were only yielded for the wind shelter parameter S_x . The general information that could be gained from the multiple regression models was that the outcome was usually best with only the two explanatory parameters S_x and elevation, holding the highest correlations with the dependent variable. On the contrary, slope and curvature had no significant additional benefit for the overall model performance. Therefore, it can be concluded that building the regression models without those parameters scores the same result. Still, the hypothesis, that *based on a high-resolution snow-free DSM and retrieved explanatory parameters, both the HS distribution and snow-free/snow-covered areas can be predicted in detail* has to be rejected. Indeed, the results show that the predicted snow-covered areas resemble the UAS records in space. Nevertheless, the range of HS is predicted very imprecisely and fails, especially in absolute HS correctness. At this point, it should be mentioned that there is no scientific study familiar to the author of this thesis that used high-resolution data of 1 m to predict snow distribution based on multiple regression models, for which reason this study contributes absolutely new information to science. Similar studies addressing the prediction of HS distribution in high alpine areas focus on data aggregated to length scales of multiple meters (Revuelto et al., 2014) or several hundreds of meters (Grünwald et al., 2013; Lehning et al., 2011b) with usually TLS measurements used for HS data acquisition.

For both response variables HS and snow/no snow, the MLR showed better performance with larger SCA. To test the hypothesis whether *satellite data can provide equal information about SCA as recorded high-resolution UAS data in order to model SCA* a contemporary satellite record to the first UAS survey was used to determine SCA based on the NDSI. The snow cover map was used to split the UAS high-resolution DSM (resampled to same resolution as SENTINEL-2 data) into snow-covered and snow-free terrain. The subsequent model accuracy of the GLM showed equal predictive force leading to the conclusion that satellite data can provide the same input information for modeling SCA on 10 m resolution as time-consuming UAS surveys and subsequent data processing (Figure 3.27, Figure 3.28).

Solar radiation is widely considered to be the main predictor of snowmelt. This study investigated the hypothesis that *based on information about incoming solar radiation, the ablation amount during two consecutive flights can be predicted in detail*. The results of the conducted MLR, however, indicate otherwise. To start, almost no correlation between the late seasonal snow patterns and solar radiation could be determined. Consequently, a simple linear regression with solar radiation as a predictor could not model ablation in detail. Only the addition of S_x and elevation (Figure 3.31) resulted in a coarse prediction of ablation with significant weakness in absolute correctness because ablation is underestimated in several magnitudes.

By comparing the characteristic ECDFs of the investigated topographic parameters between snow-covered and snow-free areas for the high-resolution DSMs, several findings could be drawn. The differences between the characteristic distributions noticeably increased with

decreasing snow cover. While the discrepancy of most parameters between snow-covered and snow-free areas is not high for the record of maximum snow extent, the differences appear more obvious in the last snow survey (Figures 3.32-3.35). The analysis showed that towards the end of the snow season, snow remains in higher altitudes and on slopes between 20 and 30 degrees. This result can be attributed to the deposition of avalanches in such slopes. Furthermore, this study confirmed that the larger part of snow-free areas could be found in southerly exposed aspects from the beginning to the end of the melt season. On the other hand, snow remained longest in northerly and northeasterly aspects. Although no correlation could be detected between snow cover and solar radiation, the cumulative density distributions proved that snow-covered areas feature smaller radiation amounts. Hence, snow melts slower in areas with diminished solar energy input. The distribution of the terrain parameter S_x indicates, snow can favorably be found in areas with positive wind scalars and thus low wind exposure, according to the considered main wind direction east. The finding that snow-covered terrain shows a more negative dominated ECDF than snow-free terrain supports the well-known fact that concave areas favor snow deposition. For the majority of the investigated predictor variables, the reported findings cannot qualify as significant and should be considered tendencies. The distribution of the wind shelter parameter within the study site alone shows a significant difference between snow-covered and snow-free terrain, numerically expressed by large effect size (Table 3.15).

For the investigation of whether areas of first snowmelt can be clearly discriminated with snow-covered areas based on topographic parameters, the snow cover extent of June 19th, 2019 was considered. This satellite record was selected for the reason that NDSI calculations produced a SCA of about 50%. This enabled an equal subdivision of the study site. Generally speaking, the ECDFs of the parameters correspond to the aforementioned patterns of the four UAS surveys, though not so clearly due to the greater snow cover extent. In comparison to the UAS records for June 19th, a significant difference in elevation between snow-free and snow-covered terrain was detected. This could be explained by the reduction in temperature with increasing elevation causing enhanced snowmelt at lower elevations. It could perhaps be derived from this result that the influence of rising temperature on discrimination between snow-free and snow-covered terrain with elevation is strongest early in the snowmelt season. As this study shows, with proceeding ablation, those zones cannot anymore be discriminated significantly by elevation. However, other topographic parameters, such as wind exposition throughout the winter season, are more accountable for the remaining characteristic snow distribution. This shows that the statistical relations found are valid for different time periods during the snow season and, consequently, are subject to changes with time, a research question that up till now has not been addressed.

5 Conclusions and recommendations for future research

The parameters S_x and elevation at 1 m resolution showed the strongest correlations with HS in comparison to the other topographic variables. Highest correlations could be detected for days with the greatest snow cover and snow depths, but for later UAS records with thinner and patchier snowpack, the correlations decreased. S_x was the best topographic variable, and the most persistent in time, for explaining HS distribution at the Klausen Pass study site. The influence of other topographic variables on the spatial distribution of HS was lower. A significant difference between snow-covered and snow-free terrain could be detected only for the distribution of the parameter S_x within the study site. This suggests the importance of including this index in future snow studies addressing late seasonal HS prediction. The results from the MLR models were consistent in terms of the coefficient of determination. HS or snow cover prediction shows the best results for days with greater snow extent and deeper snowpacks. According to the model accuracy of such predicting HS distribution for the latest surveys, the topographic variables are not sufficient information to produce precise HS outcomes. These results indicate the temporal variability of statistical relationships during the snow season.

In future studies addressing HS distribution modeling based on topographic variables, one should focus on data clustered to larger sub-areas since past studies obtained greater predictive force of two- or more parameter models in explaining HS distribution near the *time of maximum* seasonal snow accumulation (Grünwald et al., 2013; Lehning et al., 2011). However, the investigations done show that specifically *late seasonal* HS distribution cannot be linked simply to topography, since not even the main predictor of snowmelt—*solar radiation*—can explain its characteristic pattern to a bigger part. From the yielded results it has to be concluded that modeling of snow cover or even HS distribution cannot be carried out in great detail with the topographic parameters used in this study. Certainly, HS is a highly spatiotemporal variable parameter that shows temporally different statistical relationships to the addressed predictor parameters. Future studies should investigate those temporal aspects in greater detail but also look at other variables such as a fractal roughness parameter or even include detailed wind flow fields into their analysis. Also, with the found multiple regression model equations, statistical modeling should be applied to larger catchments and coarser resolution to test for representativeness and a potentially universal statistical correlation to topography.

Using an airborne equipment package costing less than 20,000 € and hence much less than TLS/ALS surveys, this study demonstrates that high-resolution snow depth maps accurate to ± 20 cm with GSDs as low as 7.5 cm can be produced on the catchment scale, contributing valuable information to snow hydrological modeling. A big advantage in comparison to LiDAR data is that photogrammetric records allow for the creation of a color orthoimage that is

perfectly co-registered with the DSM. This enables to unambiguously discriminate between snow and snow-free terrain (Nolan et al., 2015). Digital photogrammetry is about 50% more economical than ALS in data acquisition, and data processing is 10 to 40% more economical resulting in a substantial total price reduction (Bühler et al., 2015), suggesting the benefit of UAVs in snow studies and highlighting their definitive solution to the problem of mapping HS with fine spatial and temporal resolutions. This could represent an alternative to automated point station data to directly obtain distributed measurements of snow parameters. Especially with UAS surveys at the time of snow peak information, precise information about the potential SWE within a catchment can be derived, which is important information not only for government agencies or hydropower companies. The results of this study also prove that fixed-wing UASs flying at high altitudes above ground are able to cover areas of several square kilometers in great detail when wind conditions are favorable. In this respect, they present a great advantage over multirotor drones, limited to smaller areas.

For future research, it is highly recommended to integrate optical sensors at different wavelengths to UAS surveys when the land cover to map contains patchy snow cover because potentially occurring difficulties, such as the discrimination between snow and karst, do not arise in NIR imagery. RGB data complicates or even impedes an automatic classification of snow, as in the case of this study. The search for an appropriate method was without success but involved a great amount of time invested. For this reason, conducted inevitable manual snow classification can only be considered a good approximation snow boundary mask because a fully accurate classification on 7.5 cm high-resolution imagery is time-consuming and does not correspond to the purpose of this thesis. This mask, however, exposed sources of error for the performed cubic interpolation of the snow surface for bias correction of the models, which would not have existed with a precise automatic snow classification.

Besides the snow classification problem, this study confirms the potential of UAS to map HS in great detail. Extreme HS variability of several meters within short distances could be mapped, confirming the major effect of wind and terrain on the characteristic distribution of HS in high alpine areas (Mott et al., 2010). The detailed tessellated snow surfaces, clearly visible in the DSMs, show that small features on the snow surface (e.g., dirt) had a positive effect on the SfM algorithm. However, for a valuable validation of the modeled HS, probe measurements have to be recorded with a dGNSS instead of a regular GPS with unjustifiable accuracy. The usage of recently available UAS systems with dGNSS enables high-resolution DSM products on the centimeter scale. This makes time-consuming dGNSS measurements of GCPs needless for model alignment. Furthermore, image co-registration and bias correction, as performed in this study, might be unnecessary due to the higher accuracy. The cell size investigated in this study is significantly smaller than the ordinary resolution of satellite products. In this context, UAS pose a valid intermediate step between point measurements of snow at high temporal resolutions and satellites, which usually provide continuous information with low temporal and

spatial resolution (see also Michele et al. (2016) and Nolan et al. (2015) on this point). Besides the advantage of centimeter-resolution DSMs in capturing the highly variable HS distribution, results of Michele et al. (2016) show that a metric (or decimeter) resolution provides relevant spatial patterns to describe the relationship between topography and snow accumulation. Keeping the resolution at 20 cm may limit logistical and operational costs as flight height is related to DSM precision.

Before UAS missions, the camera choice and settings should be carefully considered. To counteract camera sensor saturation due to reflections of the sun on the snow, the exposure time should be properly set, and the imagery stored in RAW format using the full bit depth of the sensor. In comparison to JPEG image compression, limited to 8 bits, the RAW imagery is stored in 10 to 14 bits and hence more than 256 grayscale values per band. According to Bühler et al. (2015), this prevents image saturation over bright, snow-covered areas, and information can be acquired even in shadowed areas. Shutter speed is recommended to be set high as default because low shutter speed results in distortion, which is undesired for precise point cloud reconstruction and resulting high-resolution DSMs. Starting the flight missions earlier could have increased the quality of the photogrammetric outcomes because direct illumination of the snow surface, and thus a higher solar reflection, could have been avoided, and in RAW image data, the considerable loss of information in shadowed areas is in any case inexistent.

A further flight campaign next snow season would be valuable not only to capture snow peak and potentially find stronger correlations of topography with the HS distribution but also to obtain HS data during the ablation phase for inter-annual comparison with the here gained data.

6 References

- Adams, M. S., Bühler, Y. and Fromm, R. (2018) 'Multitemporal Accuracy and Precision Assessment of Unmanned Aerial System Photogrammetry for Slope-Scale Snow Depth Maps in Alpine Terrain', *Pure and Applied Geophysics*, vol. 175, no. 9, pp. 3303–3324 [Online]. DOI: 10.1007/s00024-017-1748-y.
- Agisoft (2019) *Agisoft Metashape* [Online]. Available at <https://www.agisoft.com/> (Accessed 14 January 2020).
- Agisoft LLC (2018) 'Agisoft PhotoScan User Manual - Professional Edition, Version 1.4'.
- Anderton, S. P., White, S. M. and Alvera, B. (2004) 'Evaluation of spatial variability in snow water equivalent for a high mountain catchment', *Hydrological Processes*, vol. 18, no. 3, pp. 435–453.
- Avanzi, F., Bianchi, A., Cina, A., Michele, C. de, Maschio, P., Pagliari, D., Passoni, D., Pinto, L., Piras, M. and Rossi, L. (2018) 'Centimetric Accuracy in Snow Depth Using Unmanned Aerial System Photogrammetry and a MultiStation', *Remote Sensing*, vol. 10, no. 5, p. 765.
- Bair, E. H., Rittger, K., Davis, R. E., Painter, T. H. and Dozier, J. (2016) 'Validating reconstruction of snow water equivalent in California's Sierra Nevada using measurements from the NASA Airborne Snow Observatory', *Water Resources Research*, vol. 52, no. 11, pp. 8437–8460.
- Barnett, T. P., Adam, J. C. and Lettenmaier, D. P. (2005) 'Potential impacts of a warming climate on water availability in snow-dominated regions', *Nature*, vol. 438, no. 7066, pp. 303–309 [Online]. DOI: 10.1038/nature04141.
- Bash, E., Moorman, B. and Gunther, A. (2018) 'Detecting Short-Term Surface Melt on an Arctic Glacier Using UAV Surveys', *Remote Sensing*, vol. 10, p. 1547.
- Bavera, D. and Michele, C. de (2009) 'Snow water equivalent estimation in the Mallero basin using snow gauge data and MODIS images and fieldwork validation', *Hydrological Processes*, vol. 23, no. 14, pp. 1961–1972.
- Bernier, M. and Fortin, J.-P. (1998) 'The potential of times series of C-Band SAR data to monitor dry and shallow snow cover', *IEEE Transactions on Geoscience and Remote Sensing*, vol. 36, no. 1, pp. 226–243.
- Blöschl, G. and Kirnbauer, R., eds. (1992) *Flächendetaillierte Modellierung der Schneeschmelze in einem alpinen Einzugsgebiet*.
- Boesch, R., Bühler, Y., Marty, M. and Ginzler, C. (2016) 'Comparison of digital surface models for snow depth mapping with UAV and aerial cameras', *XXIII ISPRS congress, commission VIII*, XLI-B8, pp. 453–458 [Online]. DOI: 10.5194/isprs-archives-XLI-B8-453-2016.
- Brandenberger, A. J. (1959) *Map of the McCall Glacier, Brooks Range, Alaska* [Online], New York, American Geographical Society. (AGS Report 11.).
- Bründl, M., Etter, H.-J., Steiniger, M., Klingler, C., Rhyner, J. and Ammann, W. J. (2004) 'IFKIS-a basis for managing avalanche risk in settlements and on roads in Switzerland', *Natural Hazards and Earth System Science*, vol. 4, no. 2, pp. 257–262.
- Buchroithner, M. F. (1995) 'Problems of mountain hazard mapping using spaceborne remote sensing techniques', *Advances in Space Research*, vol. 15, no. 11, pp. 57–66 [Online]. DOI: 10.1016/0273-1177(95)00075-P.
- Bühler, Y., Adams, M. S., Bösch, R. and Stoffel, A. (2016) 'Mapping snow depth in alpine terrain with unmanned aerial systems (UASs): potential and limitations', *The Cryosphere*, vol. 10, no. 3, pp. 1075–1088.

- Bühler, Y., Adams, M. S., Stoffel, A. and Boesch, R. (2017) 'Photogrammetric reconstruction of homogenous snow surfaces in alpine terrain applying near-infrared UAS imagery', *International Journal of Remote Sensing*, vol. 38, 8-10, pp. 3135–3158.
- Bühler, Y., Marty, M., Egli, L., Veitinger, J., Jonas, T., Thee, P. and Ginzler, C. (2015) 'Snow depth mapping in high-alpine catchments using digital photogrammetry', *The Cryosphere*, vol. 9, no. 1, pp. 229–243.
- Bühler, Y., Marty, M. and Ginzler, C. (2012) 'High Resolution DEM Generation in High-Alpine Terrain Using Airborne Remote Sensing Techniques', *Transactions in GIS*, vol. 16, no. 5, pp. 635–647.
- Bühler, Y., Meier, L. and Ginzler, C. (2014) 'Potential of operational high spatial resolution near-infrared remote sensing instruments for snow surface type mapping', *IEEE Geoscience and Remote Sensing Letters*, vol. 12, no. 4, pp. 821–825.
- Castebrunet, H., Eckert, N., Giraud, G., Durand, Y. and Morin, S. (2014) 'Projected changes of snow conditions and avalanche activity in a warming climate: the French Alps over the 2020–2050 and 2070–2100 periods', *The Cryosphere*, vol. 8, no. 5, pp. 1673–1697.
- Chang, K.-T. and Li, Z. (2000) 'Modelling snow accumulation with a geographic information system', *International Journal of Geographical Information Science*, vol. 14, no. 7, pp. 693–707.
- Clark, M. P., Hendrikx, J., Slater, A. G., Kavetski, D., Anderson, B., Cullen, N. J., Kerr, T., Örn Hreinsson, E. and Woods, R. A. (2011) 'Representing spatial variability of snow water equivalent in hydrologic and land-surface models: A review', *Water Resources Research*, vol. 47, no. 7, p. 435.
- Clifford, D. (2010) 'Global estimates of snow water equivalent from passive microwave instruments: history, challenges and future developments', *International Journal of Remote Sensing*, vol. 31, no. 14, pp. 3707–3726.
- Cline, D. W. (1993) 'Measuring alpine snow depths by digital photogrammetry: Part 1. conjugate point identification, Proceedings of the Eastern Snow Conference, 8–10 June 1993, Quebec City, Canada'.
- Cline, D. W. (1994) 'Digital Photogrammetric Determination Of Alpine Snowpack Distribution For Hydrologic Modeling, Colorado State University, CO, USA'.
- Copernicus Open Access Hub (2019) [Online]. Available at <https://scihub.copernicus.eu/dhus/> (Accessed 21 October 2019).
- Crawford, C. J., Manson, S. M., Bauer, M. E. and Hall, D. K. (2013) 'Multitemporal snow cover mapping in mountainous terrain for Landsat climate data record development', *Remote Sensing of Environment*, vol. 135, pp. 224–233 [Online]. DOI: 10.1016/j.rse.2013.04.004.
- Dadic, R., Mott, R., Lehning, M. and Burlando, P. (2010) 'Wind influence on snow depth distribution and accumulation over glaciers', *Journal of Geophysical Research: Earth Surface*, vol. 115, F1.
- Deems, J. S., Fassnacht, S. R. and Elder, K. J. (2006) 'Fractal distribution of snow depth from LiDAR data', *Journal of Hydrometeorology*, vol. 7, no. 2, pp. 285–297.
- Deems, J. S. and Painter, T. H., eds. (2006) *Lidar measurement of snow depth: accuracy and error sources*.
- Deems, J. S., Painter, T. H. and Finnegan, D. C. (2013) 'Lidar measurement of snow depth: a review', *Journal of Glaciology*, vol. 59, no. 215, pp. 467–479.
- Déry, S. J. and Brown, R. D. (2007) 'Recent Northern Hemisphere snow cover extent trends and implications for the snow-albedo feedback', *Geophysical Research Letters*, vol. 34, no. 22, p. 367.

- Dickinson, W. T. and Whiteley, H. R. (1972) 'A sampling scheme for shallow snowpacks', *Hydrological Sciences Journal*, vol. 17, no. 3, pp. 247–258.
- Dietz, A. J., Kuenzer, C., Gessner, U. and Dech, S. (2012) 'Remote sensing of snow – a review of available methods', *International Journal of Remote Sensing*, vol. 33, no. 13, pp. 4094–4134.
- Doorschot, J., Raderschall, N. and Lehning, M. (2001) 'Measurements and one-dimensional model calculations of snow transport over a mountain ridge', *Annals of Glaciology*, vol. 32, pp. 153–158.
- Dormann, C. F. (2013) *Parametrische Statistik: Verteilungen, maximum likelihood und GLM in R* [Online], Berlin, Heidelberg, Springer. Available at <http://gbv.eblib.com/patron/FullRecord.aspx?p=1206060>.
- Dozier, J. and Shi, J. (2000) 'Estimation of snow water equivalence using SIR-C/X-SAR. II. Inferring snow depth and particle size', *IEEE Transactions on Geoscience and Remote Sensing*, vol. 38, no. 6, pp. 2475–2488.
- Eckerstorfer, M., Bühler, Y., Frauenfelder, R. and Malnes, E. (2016) 'Remote sensing of snow avalanches: Recent advances, potential, and limitations', *Cold Regions Science and Technology*, vol. 121, pp. 126–140.
- Edwards, A. C., Scalenghe, R. and Freppaz, M. (2007) 'Changes in the seasonal snow cover of alpine regions and its effect on soil processes: A review', *Quaternary International*, 162–163, pp. 172–181.
- Egli, L. (2008) 'Spatial variability of new snow amounts derived from a dense network of Alpine automatic stations', *Annals of Glaciology*, vol. 49, pp. 51–55.
- Egli, L., Jonas, T., Grünewald, T., Schirmer, M. and Burlando, P. (2012) 'Dynamics of snow ablation in a small Alpine catchment observed by repeated terrestrial laser scans', *Hydrological Processes*, vol. 26, no. 10, pp. 1574–1585.
- Egli, L. E. (2011) *Spatial variability of seasonal snow cover at different scales in the Swiss Alps*, ETH Zurich.
- Eker, R., Bühler, Y., Schlögl, S., Stoffel, A. and Aydın, A. (2019) 'Monitoring of Snow Cover Ablation Using Very High Spatial Resolution Remote Sensing Datasets', *Remote Sensing*, vol. 11, no. 6, p. 699.
- Elder, K., Dozier, J. and Michaelsen, J. (1991) 'Snow accumulation and distribution in an alpine watershed', *Water Resources Research*, vol. 27, no. 7, pp. 1541–1552.
- Elder, K., Rosenthal, W. and Davis, R. E. (1998) 'Estimating the spatial distribution of snow water equivalence in a montane watershed', *Hydrological Processes*, vol. 12, 10 - 11, pp. 1793–1808 [Online]. DOI: 10.1002/(SICI)1099-1085(199808/09)12:10/11<1793::AID-HYP695>3.0.CO;2-K.
- Elsasser, H. and Bürki, R. (2002) 'Climate change as a threat to tourism in the Alps', *Climate research*, vol. 20, no. 3, pp. 253–257.
- Erickson, T. A., Williams, M. W. and Winstral, A. (2005) 'Persistence of topographic controls on the spatial distribution of snow in rugged mountain terrain, Colorado, United States', *Water Resources Research*, vol. 41, no. 4.
- ESA (2019) *Level-2A Algorithm - Sentinel-2 MSI Technical Guide - Sentinel Online* [Online]. Available at <https://earth.esa.int/web/sentinel/technical-guides/sentinel-2-msi/level-2a/algorithm> (Accessed 14 January 2020).
- Farinotti, D., Magnusson, J., Huss, M. and Bauder, A. (2010) 'Snow accumulation distribution inferred from time-lapse photography and simple modelling', *Hydrological Processes*, vol. 24, no. 27, n/a-n/a.

- Farinotti, D., Usselmann, S., Huss, M., Bauder, A. and Funk, M. (2012) 'Runoff evolution in the Swiss Alps: projections for selected high - alpine catchments based on ENSEMBLES scenarios', *Hydrological Processes*, vol. 26, no. 13, pp. 1909–1924.
- Fisher, P. F. and Tate, N. J. (2006) 'Causes and consequences of error in digital elevation models', *Progress in physical Geography*, vol. 30, no. 4, pp. 467–489.
- FOEN (2019) *Schächen - Bürglen, Galgenwäldli, main station 2491* [Online]. Available at <https://www.hydrodaten.admin.ch/en/2491.html> (Accessed 15 January 2020).
- Foppa, N., Stoffel, A. and Meister, R. (2007) 'Synergy of in situ and space borne observation for snow depth mapping in the Swiss Alps', *International Journal of Applied Earth Observation and Geoinformation*, vol. 9, no. 3, pp. 294–310.
- Freudiger, D., Kohn, I., Seibert, J., Stahl, K. and Weiler, M. (2017) 'Snow redistribution for the hydrological modeling of alpine catchments', *Wiley Interdisciplinary Reviews: Water*, vol. 4, no. 5, e1232.
- Fugazza, D., Senese, A., Azzoni, R. S., Smiraglia, C., Cernuschi, M., Severi, D. and Diolaiuti, G. A. (2015) 'High resolution mapping of glacier surface features. The UAV survey of the Forni Glacier (Stelvio National Park, Italy)', *Geogr. Fis. Dinam. Quat.*, no. 38, pp. 25–33.
- Gibbs, A., NOLAN, M. and Richmond, B. (2015) *Evaluating changes to arctic coastal bluffs using repeat aerial photography and structure-from-motion elevation models*.
- Goetz, J. and Brenning, A. (2019) 'Quantifying Uncertainties in Snow Depth Mapping From Structure From Motion Photogrammetry in an Alpine Area', *Water Resources Research*, vol. 175, no. 9, p. 3303.
- Goodrich, L. E. (1982) 'The influence of snow cover on the ground thermal regime', *Canadian Geotechnical Journal*, vol. 19, no. 4, pp. 421–432.
- Grünewald, T., Bühler, Y. and Lehning, M. (2014) 'Elevation dependency of mountain snow depth', *The Cryosphere*, vol. 8, no. 6, pp. 2381–2394 [Online]. DOI: 10.5194/tc-8-2381-2014.
- Grünewald, T. and Lehning, M. (2015) 'Are flat-field snow depth measurements representative? A comparison of selected index sites with areal snow depth measurements at the small catchment scale', *Hydrological Processes*, vol. 29, no. 7, pp. 1717–1728.
- Grünewald, T., Schirmer, M., Mott, R. and Lehning, M. (2010) 'Spatial and temporal variability of snow depth and ablation rates in a small mountain catchment', *The Cryosphere*, vol. 4, no. 2, pp. 215–225.
- Grünewald, T., Stotter, J., Pomeroy, J. W., Dadic, R., Banos, I. M., Marturià, J., Sproß, M., Hopkinson, C., Burlando, P. and Lehnig, M. (2013) 'Statistical modelling of the snow depth distribution in open alpine terrain'.
- Guneriusen, T., Hogda, K. A., Johnsen, H. and Lauknes, I. (2001) 'InSAR for estimation of changes in snow water equivalent of dry snow', *IEEE Transactions on Geoscience and Remote Sensing*, vol. 39, no. 10, pp. 2101–2108.
- Haefner, H., Seidel, K. and Ehrler, H. (1997) 'Applications of snow cover mapping in high mountain regions', *Physics and Chemistry of the Earth*, vol. 22, 3-4, pp. 275–278.
- Hall, D. K., Riggs, G. A. and Salomonson, V. V. (1995) 'Development of methods for mapping global snow cover using moderate resolution imaging spectroradiometer data', *Remote Sensing of Environment*, vol. 54, no. 2, pp. 127–140 [Online]. DOI: 10.1016/0034-4257(95)00137-P.
- Hamilton, T. D. (1965) 'Comparative glacier photographs from northern Alaska', *Journal of Glaciology*, vol. 5, no. 40, pp. 479–487.

- Harder, P., Schirmer, M., Pomeroy, J. and Helgason, W. (2016) 'Accuracy of snow depth estimation in mountain and prairie environments by an unmanned aerial vehicle', *The Cryosphere*, vol. 10, no. 6, pp. 2559–2571.
- Hedrick, A., Marshall, H.-P., Winstral, A., Elder, K., Yueh, S. and Cline, D. (2015) 'Independent evaluation of the SNODAS snow depth product using regional-scale lidar-derived measurements', *The Cryosphere*, vol. 9, no. 1, pp. 13–23.
- Hood, J. L. and Hayashi, M. (2010) 'Assessing the application of a laser rangefinder for determining snow depth in inaccessible alpine terrain', *Hydrology and Earth System Sciences*, vol. 14, no. 6, p. 901.
- Hopkinson, C., Collins, T., Anderson, A., Pomeroy, J. and Spooner, I. (2012) 'Spatial Snow Depth Assessment Using LiDAR Transect Samples and Public GIS Data Layers in the Elbow River Watershed, Alberta', *Canadian Water Resources Journal / Revue canadienne des ressources hydriques*, vol. 37, no. 2, pp. 69–87.
- Hopkinson, C., Sitar, M., Chasmer, L. and Treitz, P. (2004) 'Mapping snowpack depth beneath forest canopies using airborne lidar', *Photogrammetric Engineering & Remote Sensing*, vol. 70, no. 3, pp. 323–330.
- James, M. R., Robson, S., d'Oleire-Oltmanns, S. and Niethammer, U. (2017) 'Optimising UAV topographic surveys processed with structure-from-motion: Ground control quality, quantity and bundle adjustment', *Geomorphology*, vol. 280, pp. 51–66.
- Jonas, T., Marty, C. and Magnusson, J. (2009) 'Estimating the snow water equivalent from snow depth measurements in the Swiss Alps', *Journal of Hydrology*, vol. 378, 1-2, pp. 161–167.
- Julitta, T., Cremonese, E., Migliavacca, M., Colombo, R., Galvagno, M., Siniscalco, C., Rossini, M., Fava, F., Cogliati, S., Di Morra Cella, U. and Menzel, A. (2014) 'Using digital camera images to analyse snowmelt and phenology of a subalpine grassland', *Agricultural and Forest Meteorology*, 198-199, pp. 116–125.
- Kelly, M., Blanchard, S., Kersten, E. and Koy, K. (2011) 'Terrestrial Remotely Sensed Imagery in Support of Public Health: New Avenues of Research Using Object-Based Image Analysis', *Remote Sensing*, vol. 3, pp. 2321–2345.
- Kelly, M., Shaari, D., Guo, Q. and Liu, D. (2004) 'A comparison of standard and hybrid classifier methods for mapping hardwood mortality in areas affected by "sudden oak death"', *Photogrammetric Engineering & Remote Sensing*, vol. 70, no. 11, pp. 1229–1239.
- Kendra, J. R., Sarabandi, K. and Ulaby, F. T. (1998) 'Radar measurements of snow: experiment and analysis', *IEEE Transactions on Geoscience and Remote Sensing*, vol. 36, no. 3, pp. 864–879.
- König, M. and Sturm, M. (1998) 'Mapping snow distribution in the Alaskan Arctic using aerial photography and topographic relationships', *Water Resources Research*, vol. 34, no. 12, pp. 3471–3483.
- Ledwith, M. and Lundén, B. (2001) 'Digital photogrammetry for air-photo-based construction of a digital elevation model over snow-covered areas - Blamannsisen, Norway', *Norsk Geografisk Tidsskrift-Norwegian Journal of Geography*, vol. 55, no. 4, pp. 267–273.
- Lee, C. Y., Jones, S. D., Bellman, C. J. and Buxton, L. (2008) 'DEM creation of a snow covered surface using digital aerial photography. In Proceedings of the International Archives of the Photogrammetry, Remote Sensing and Spatial Information Sciences, XXXVII (Part B8), Beijing, China, 3-11 July 2008 ; pp. 831–835'.
- Lehning, M., Grünewald, T. and Schirmer, M. (2011a) 'Mountain snow distribution governed by an altitudinal gradient and terrain roughness', *Geophysical Research Letters*, vol. 38, no. 19.

- Lehning, M., Grünewald, T. and Schirmer, M. (2011b) 'Mountain snow distribution governed by an altitudinal gradient and terrain roughness', *Geophysical Research Letters*, vol. 38, no. 19.
- Lehning, M., Löwe, H., Ryser, M. and Raderschall, N. (2008) 'Inhomogeneous precipitation distribution and snow transport in steep terrain', *Water Resources Research*, vol. 44, no. 7 [Online]. DOI: 10.1029/2007WR006545.
- Lehning, M., Völksch, I., Gustafsson, D., Nguyen, T., Stähli, M. and Zappa, M. (2006) 'ALPINE3D: A detailed model of mountain surface processes and its application to snow hydrology', *Hydrological Processes*, vol. 20, pp. 2111–2128.
- Lemke, P., Ren, J. F., Alley, R. B., Allison, I., Carrasco, J., Flato, G., Fujii, Y., Kaser, G., Mote, P., Thomas, R. H. and Zhang, T. (2007) 'Observations: Changes in Snow, Ice and Frozen Ground. In: Climate Change 2007: The Physical Science Basis. Contribution of Working Group I to the Fourth Assessment Report of the Intergovernmental Panel on Climate Change', *Climate Change 2007: The Physical Science Basis*.
- Lendzioch, T., Langhammer, J. and Jeníček, M. (2016) 'Tracking forest and open area effects on snow accumulation by Unmanned Aerial Vehicle Photogrammetry', *ISPRS - International Archives of the Photogrammetry, Remote Sensing and Spatial Information Sciences*, XLI-B1, pp. 917–923.
- Liston, G. E., Haehnel, R. B., Sturm, M., Hiemstra, C. A., Berezovskaya, S. and Tabler, R. D. (2007) 'Simulating complex snow distributions in windy environments using SnowTran-3D', *Journal of Glaciology*, vol. 53, no. 181, pp. 241–256.
- Liston, G. E. and Sturm, M. (2002) 'Winter precipitation patterns in arctic Alaska determined from a blowing-snow model and snow-depth observations', *Journal of Hydrometeorology*, vol. 3, no. 6, pp. 646–659.
- López-Moreno, J. I., Fassnacht, S. R., Heath, J. T., Musselman, K. N., Revuelto, J., Latron, J., Morán-Tejeda, E. and Jonas, T. (2013) 'Small scale spatial variability of snow density and depth over complex alpine terrain: Implications for estimating snow water equivalent', *Advances in Water Resources*, vol. 55, pp. 40–52.
- López-Moreno, J. I., Latron, J. and Lehmann, A. (2010) 'Effects of sample and grid size on the accuracy and stability of regression - based snow interpolation methods', *Hydrological Processes*, vol. 24, no. 14, pp. 1914–1928.
- López-Moreno, J. I. and Nogués-Bravo, D. (2006) 'Interpolating local snow depth data: an evaluation of methods', *Hydrological Processes*, vol. 20, no. 10, pp. 2217–2232.
- López-Moreno, J. I., Revuelto, J., Fassnacht, S. R., Azorín-Molina, C., Vicente-Serrano, S. M., Morán-Tejeda, E. and Sexton, G. A. (2015) 'Snowpack variability across various spatio-temporal resolutions', *Hydrological Processes*, vol. 29, no. 6, pp. 1213–1224.
- Lucas, R. M. and Harrison, A. R. (1990) 'Snow observation by satellite: A review', *Remote Sensing Reviews*, vol. 4, no. 2, pp. 285–348.
- Luce, C. H., Tarboton, D. G. and Cooley, K. R. (1999) 'Sub - grid parameterization of snow distribution for an energy and mass balance snow cover model', *Hydrological Processes*, vol. 13, 12 - 13, pp. 1921–1933.
- Luzi, G., Noferini, L., Mecatti, D., Macaluso, G., Pieraccini, M., Atzeni, C., Schaffhauser, A., Fromm, R. and Nagler, T. (2009) 'Using a Ground-Based SAR Interferometer and a Terrestrial Laser Scanner to Monitor a Snow-Covered Slope: Results From an Experimental Data Collection in Tyrol (Austria)', *IEEE Transactions on Geoscience and Remote Sensing*, vol. 47, no. 2, pp. 382–393.
- Macelloni, G., Paloscia, S., Pampaloni, P., Brogioni, M., Ranzi, R. and Crepaz, A. (2005) 'Monitoring of melting refreezing cycles of snow with microwave radiometers: the Microwave Alpine Snow Melting Experiment (MASME 2002-2003)', *IEEE Transactions on Geoscience and Remote Sensing*, vol. 43, no. 11, pp. 2431–2442.

- Machguth, H., Eisen, O., Paul, F. and Hoelzle, M. (2006) 'Strong spatial variability of snow accumulation observed with helicopter-borne GPR on two adjacent Alpine glaciers', *Geophysical Research Letters*, vol. 33, no. 13, p. 317.
- Mankin, J. S., Viviroli, D., Singh, D., Hoekstra, A. Y. and Diffenbaugh, N. S. (2015) 'The potential for snow to supply human water demand in the present and future', *Environmental research letters*, vol. 10, no. 11 [Online]. DOI: 10.1088/1748-9326/10/11/114016.
- Marchand, W.-D. and Killingtveit, Å. (2004) 'Statistical properties of spatial snowcover in mountainous catchments in Norway', *Hydrology Research*, vol. 35, no. 2, pp. 101–117.
- Marti, R., Gascoin, S., Berthier, E., Pinel, M. de, Houet, T. and Laffly, D. (2016) 'Mapping snow depth in open alpine terrain from stereo satellite imagery', *The Cryosphere*, vol. 10, no. 4, pp. 1361–1380.
- Martinez-Vazquez, A., Fortuny-Guasch, J. and Gruber, U. (2005) 'A. Martinez-Vazquez, J. Fortuny-Guasch, and U. Gruber, Monitoring of the snow cover with a ground-based synthetic aperture radar, EARSel eProc., vol. 4, no. 2, pp. 171–178'.
- Marty, C. (2008) 'Regime shift of snow days in Switzerland', *Geophysical Research Letters*, vol. 35, no. 12, n/a-n/a.
- Mattmann, C. A., Painter, T., Ramirez, P. M., Goodale, C., Hart, A. F., Zimdars, P., Boustani, M., Khudikyan, S., Verma, R. and Caprez, F. S., eds. (2014) *24 hour near real time processing and computation for the jpl airborne snow observatory*.
- McKay, G. A., ed. (1968) *Problems of measuring and evaluating snow cover*.
- Melvold, K. and Skaugen, T. (2013) 'Multiscale spatial variability of lidar-derived and modeled snow depth on Hardangervidda, Norway', *Annals of Glaciology*, vol. 54, no. 62, pp. 273–281 [Online]. DOI: 10.3189/2013AoG62A161.
- Michele, C. de, Avanzi, F., Passoni, D., Barzaghi, R., Pinto, L., Dosso, P., Ghezzi, A., Gianatti, R. and Della Vedova, G. (2016) 'Using a fixed-wing UAS to map snow depth distribution: an evaluation at peak accumulation', *The Cryosphere*, vol. 10, no. 2, pp. 511–522.
- Miziński, B. and Niedzielski, T. (2017) 'Fully-automated estimation of snow depth in near real time with the use of unmanned aerial vehicles without utilizing ground control points', *Cold Regions Science and Technology*, vol. 138, pp. 63–72.
- Mizukami, N. and Perica, S. (2008) 'Spatiotemporal characteristics of snowpack density in the mountainous regions of the western United States', *Journal of Hydrometeorology*, vol. 9, no. 6, pp. 1416–1426.
- Morrison, K., Rott, H., Nagler, T., Rebhan, H. and Wursteisen, P. (2007) 'The SARALPS-2007 measurement campaign on Xand Ku-Band Backscatter of snow', *IEEE Workshop on Signal Processing Systems, 2007: Shanghai, China, 17 - 19 October 2007*. Barcelona, Spain, 7/23/2007 - 7/28/2007. Piscataway, NJ, IEEE, pp. 1207–1210.
- Mott, R., Schirmer, M., Bavay, M., Grünewald, T. and Lehning, M. (2010) 'Understanding snow-transport processes shaping the mountain snow-cover', *The Cryosphere*, vol. 4, no. 4, pp. 545–559.
- Niedzielski, T., Spallek, W. and Witek-Kasprzak, M. (2018) 'Automated Snow Extent Mapping Based on Orthophoto Images from Unmanned Aerial Vehicles', *Pure and Applied Geophysics*, vol. 175, no. 9, pp. 3285–3302.
- Nolan, M., Larsen, C. and Sturm, M. (2015) 'Mapping snow depth from manned aircraft on landscape scales at centimeter resolution using structure-from-motion photogrammetry', *The Cryosphere*, vol. 9, no. 4, pp. 1445–1463.
- Nöthiger, C. and Elsasser, H. (2004) 'Natural hazards and tourism: new findings on the European Alps', *Mountain Research and Development*, vol. 24, no. 1, pp. 24–28.

- Oveisgharan, S. and Zebker, H. A. (2007) 'Estimating Snow Accumulation From InSAR Correlation Observations', *IEEE Transactions on Geoscience and Remote Sensing*, vol. 45, no. 1, pp. 10–20.
- Parajka, J. and Blöschl, G. (2006) 'Validation of MODIS snow cover images over Austria', *Hydrology and Earth System Sciences Discussions*, vol. 3, no. 4, pp. 1569–1601.
- Parajka, J., Haas, P., Kirnbauer, R., Jansa, J. and Blöschl, G. (2012) 'Potential of time - lapse photography of snow for hydrological purposes at the small catchment scale', *Hydrological Processes*, vol. 26, no. 22, pp. 3327–3337 [Online]. DOI: 10.1002/hyp.8389.
- Pelto, B. M., Menounos, B. and Marshall, S. J. (2019) 'Multi-year evaluation of airborne geodetic surveys to estimate seasonal mass balance, Columbia and Rocky Mountains, Canada', *The Cryosphere*, vol. 13, no. 6, pp. 1709–1727.
- Pidwirny, M. (2008) *Glossary of Terms: N* [Online]. Available at <http://www.physicalgeography.net/physgeoglos/n.html> (Accessed 10 October 2019).
- Pomeroy, J. W. and Gray, D. M. (1995) 'Snowcover accumulation, relocation and management', *Bulletin of the International Society of Soil Science* no. 88, no. 2.
- Post, A. (1969) 'Distribution of surging glaciers in western North America', *Journal of Glaciology*, vol. 8, no. 53, pp. 229–240.
- Post, A. (1995) 'Annual aerial photography of glaciers in Northwest North America: How it all began and its golden age', *Physical Geography*, vol. 16, no. 1, pp. 15–26.
- Prokop, A. (2008a) 'Assessing the applicability of terrestrial laser scanning for spatial SD measurements', *Cold Regions Science and Technology*, vol. 54, pp. 155–163.
- Prokop, A. (2008b) 'Assessing the applicability of terrestrial laser scanning for spatial snow depth measurements', *Cold Regions Science and Technology*, vol. 54, no. 3, pp. 155–163.
- Prokop, A., Schirmer, M., Rub, M., Lehning, M. and Stocker, M. (2008) 'A comparison of measurement methods: terrestrial laser scanning, tachymetry and snow probing for the determination of the spatial snow-depth distribution on slopes', *Annals of Glaciology*, vol. 49, pp. 210–216.
- Redpath, T. A. N., Sirguey, P. and Cullen, N. J. (2018) 'Repeat mapping of snow depth across an alpine catchment with RPAS photogrammetry', *The Cryosphere*, vol. 12, no. 11, pp. 3477–3497.
- Revuelto, J., López-Moreno, J. I., Azorin-Molina, C. and Vicente-Serrano, S. M. (2014) 'Topographic control of snowpack distribution in a small catchment in the central Spanish Pyrenees: intra- and inter-annual persistence', *The Cryosphere*, vol. 8, no. 5, pp. 1989–2006.
- Rittger, K., Painter, T. H. and Dozier, J. (2013) 'Assessment of methods for mapping snow cover from MODIS', *Advances in Water Resources*, vol. 51, pp. 367–380.
- Rixen, C., Teich, M., Lardelli, C., Gallati, D., Pohl, M., Pütz, M. and Bebi, P. (2011) 'Winter tourism and climate change in the Alps: an assessment of resource consumption, snow reliability, and future snowmaking potential', *Mountain Research and Development*, vol. 31, no. 3, pp. 229–237.
- Rossini, M., Di Mauro, B., Garzonio, R., Baccolo, G., Cavallini, G., Mattavelli, M., Amicis, M. de and Colombo, R. (2018) 'Rapid melting dynamics of an alpine glacier with repeated UAV photogrammetry', *Geomorphology*, vol. 304, pp. 159–172.
- Rott, H., Cline, D., Duguay, C., Essery, R., Haas, C., Macelloni, G., Malnes, E., Pulliainen, J., Rebhan, H. and Yueh, S., eds. (2008) *CoReH2O - A Ku- and X-Band SAR Mission for Snow and Ice Monitoring* (7th European Conference on Synthetic Aperture Radar).
- Rovansek, R. J., Hinzman, L. D. and Kane, D. L. (1996) 'Hydrology of a tundra wetland complex on the Alaskan Arctic Coastal Plain, USA', *Arctic and Alpine Research*, vol. 28, no. 3, pp. 311–317.

- Schanda, E., Matzler, C. and Kunzi, K. (1983) 'Microwave remote sensing of snow cover', *International Journal of Remote Sensing*, vol. 4, no. 1, pp. 149–158.
- Schweizer, J., Kronholm, K., Jamieson, J. B. and Birkeland, K. W. (2008) 'Review of spatial variability of snowpack properties and its importance for avalanche formation', *Cold Regions Science and Technology*, vol. 51, 2-3, pp. 253–272.
- senseFly Ltd (2016) 'User Manual: eBee'.
- Serreze, M. C., Clark, M. P., Armstrong, R. L., McGinnis, D. A. and Pulwarty, R. S. (1999) 'Characteristics of the western United States snowpack from snowpack telemetry (SNOTEL) data', *Water Resources Research*, vol. 35, no. 7, pp. 2145–2160.
- Shook, K. and Gray, D. M. (1996) 'Small - scale spatial structure of shallow snowcovers' , *Hydrological Processes*, vol. 10, no. 10, pp. 1283–1292.
- Slater, A. G. and Clark, M. P. (2006) 'Snow data assimilation via an ensemble Kalman filter', *Journal of Hydrometeorology*, vol. 7, no. 3, pp. 478–493.
- Smith, F. M., Cooper, C. F. and Chapman, E. G., eds. (1967) *Measuring Snow Depths by Aerial Photography*.
- Spektrum der Wissenschaft (2014) *Kurtosis* [Online]. Available at <https://www.spektrum.de/lexikon/geographie/kurtosis/4488> (Accessed 15 January 2020).
- Sturm, M., Goldstein, M. A. and Parr, C. (2017) 'Water and life from snow: A trillion dollar science question', *Water Resources Research*, vol. 53, no. 5, pp. 3534–3544 [Online]. DOI: 10.1002/2017WR020840.
- Sullivan, G. M. and Feinn, R. (2012) 'Using Effect Size-or Why the P Value Is Not Enough', *Journal of graduate medical education*, vol. 4, no. 3, pp. 279–282.
- Tedesco, M. and Miller, J. (2007) 'Northern Hemisphere Snow-Covered Area Mapping: Optical Versus Active and Passive Microwave Data', *IEEE Geoscience and Remote Sensing Letters*, vol. 4, no. 2, pp. 221–225.
- Trimble Navigation Limited (2019a) *Trimble R7/R8 GPS Receiver User Guide* [Online]. Available at https://www.trimble.com/gps_tutorial/dgps-how.aspx (Accessed 11 September 2019).
- Trimble Navigation Limited (2019b) 'trimble-r7-gnss-datasheet' [Online]. Available at <http://old.agis.sk/produkty/geodeticke-prijimace-gnss/trimble-r7-gnss--datasheet.pdf> (Accessed 18 September 2019).
- Vander Jagt, B., Lucieer, A., Wallace, L., Turner, D. and Durand, M. (2015) 'Snow Depth Retrieval with UAS Using Photogrammetric Techniques', *Geosciences*, vol. 5, no. 3, pp. 264–285.
- Wainwright, H. M., Liljedahl, A. K., Dafflon, B., Ulrich, C., Peterson, J. E., Gusmeroli, A. and Hubbard, S. S. (2017) 'Mapping snow depth within a tundra ecosystem using multiscale observations and Bayesian methods', *The Cryosphere*, vol. 11, no. 2, pp. 857–875.
- Winstral, A., Elder, K. and Davis, R. E. (2002) 'Spatial Snow Modeling of Wind-Redistributed Snow Using Terrain-Based Parameters', *Journal of Hydrometeorology*, vol. 3, no. 5, pp. 524–538.
- Wipf, S., Stoeckli, V. and Bebi, P. (2009) 'Winter climate change in alpine tundra: plant responses to changes in snow depth and snowmelt timing', *Climatic change*, vol. 94, 1-2, pp. 105–121.
- Worby, A. P., Markus, T., Steer, A. D., Lytle, V. I. and Massom, R. A. (2008) 'Evaluation of AMSR - E snow depth product over East Antarctic sea ice using in situ measurements and aerial photography' , *Journal of Geophysical Research: Earth Surface*, vol. 113, C5.

- WSL Institute for Snow and Avalanche Research SLF (2019) *Description of automated stations - SLF* [Online]. Available at <https://www.slf.ch/en/avalanche-bulletin-and-snow-situation/measured-values/description-of-automated-stations.html> (Accessed 14 January 2020).
- Zhang, Q., Skjetne, R., Løset, S. and Marchenko, A., eds. (2012) *Digital image processing for sea ice observations in support to Arctic DP operations*, American Society of Mechanical Engineers Digital Collection.
- Zhang, Q., van der Werff, S., Metrikin, I., Løset, S. and Skjetne, R., eds. (2012) *Image processing for the analysis of an evolving broken-ice field in model testing*, American Society of Mechanical Engineers.

7 Appendix

7.1 List of Abbreviations

Advanced Very High Resolution Radiometer	AVHRR
Automated GNSS Network for Switzerland	AGNES
Digital elevation model	DEM
Digital surface model	DSM
Differential Global Navigation Satellite System	dGNSS
Differential Synthetic Aperture Radar	DInSAR
Empirical cumulative density function	ECDF
European Space Agency	ESA
Federal Office for the Environment	FOEN
Generalized Linear Model	GLM
Ground-based Synthetic Aperture Radar Interferometry	GB SAR
Ground control points	GCP
Ground sampling distance	GSD
Inertial motion units	IMUs
Intercantonal Measurement and Information System	IMIS
Light Detection and Ranging	LiDAR
Linear Model	LM
Moderate Resolution Imaging Radiometer	MODIS
Multiple linear regression	MLR
Near-infrared	NIR
Normalized Difference Snow Index	NDSI
Principal component analysis	PCA
Residual Standard Error	RSE
Root mean square error	RMSE
Terrestrial/Airborne Laser Scanning	TLS/ALS
Runoff rate	Q [mmd ⁻¹]
Satellitenpositionierungsdienst der deutschen Landesvermessung	SAPOS
Schweizer Positionierungsdienst des Bundesamts für Landestopographie	SWIPOS
Short-wavelength infrared	SWIR
Shuttle Radar Topography Mission	SRTM
Snow-covered area	SCA
Snow density	q [kg m ⁻³]
Snow depth	HS [m]
Snow monitoring stations	SnoMos
Snow volume	V [m ³]
Snow water equivalent	SWE [mm]
Structure-from-motion	SfM
Synthetic Aperture Radar	SAR
Unmanned aerial system	UAS
Very high resolution	VHR
Visible and Infrared	VIR

7.2 Figures

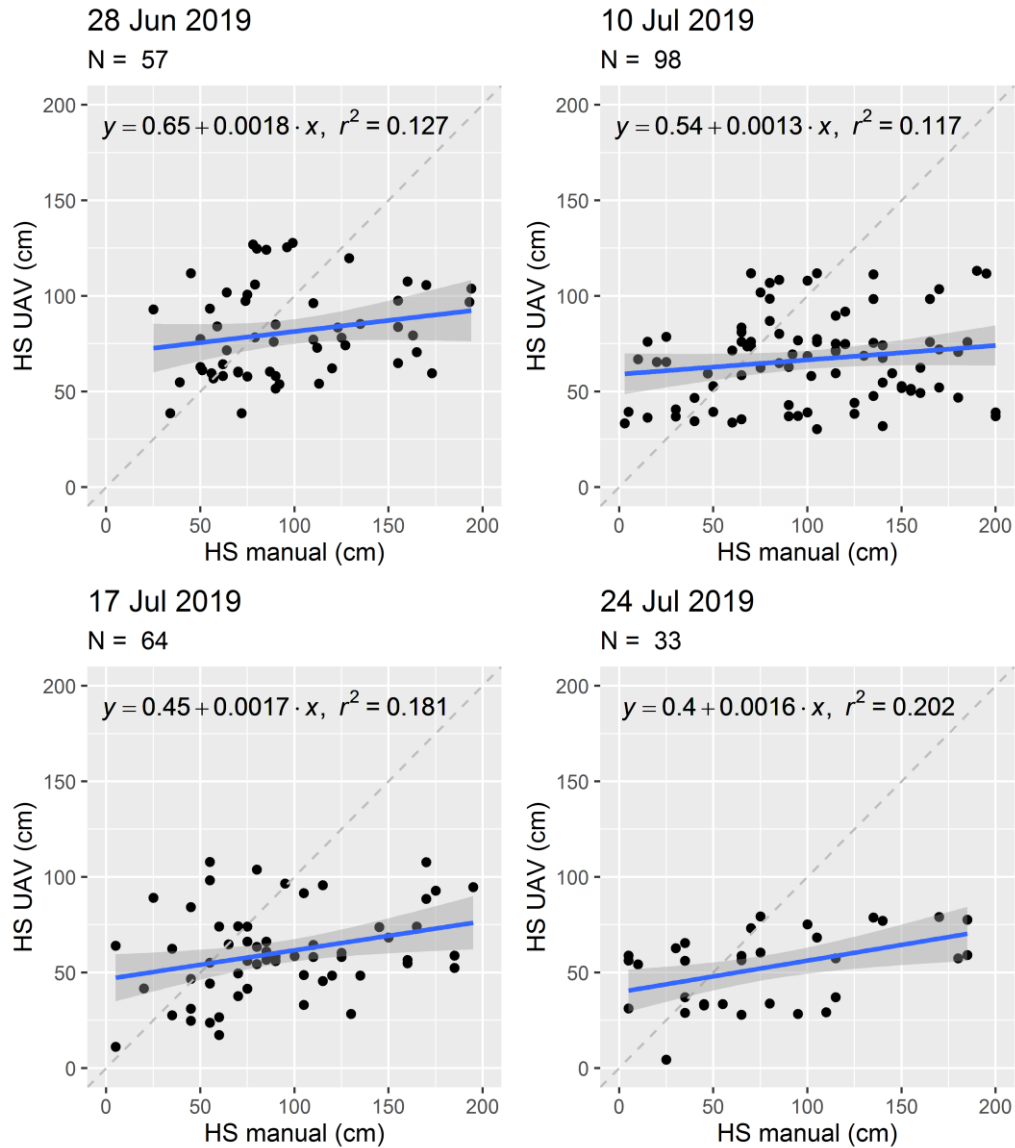


Figure A1: Absolute mean values of manual (Buffer of 10 m) and modeled HS (cm) for the four surveys.

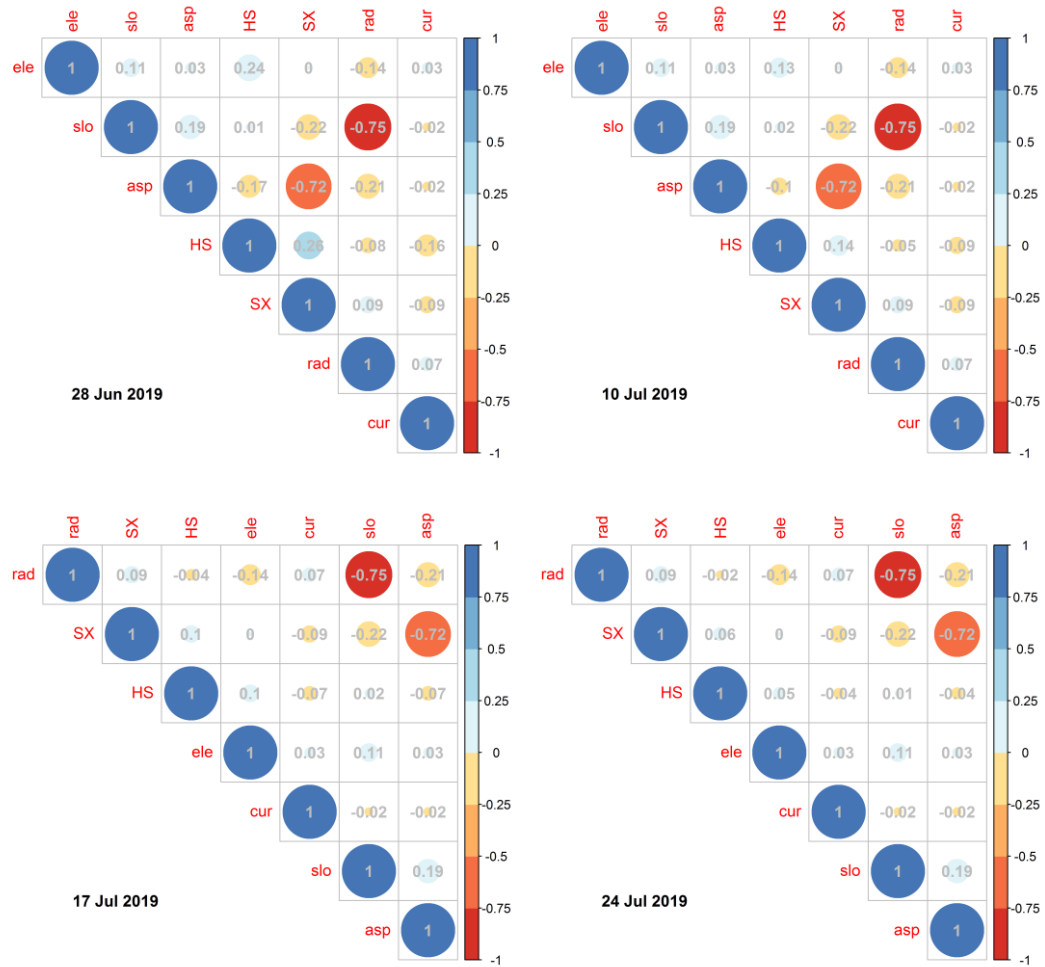


Figure A2: Correlation plot with correlation coefficients of dependent variable HS and predictor variables for the 4 UAS surveys (10 m resolution).

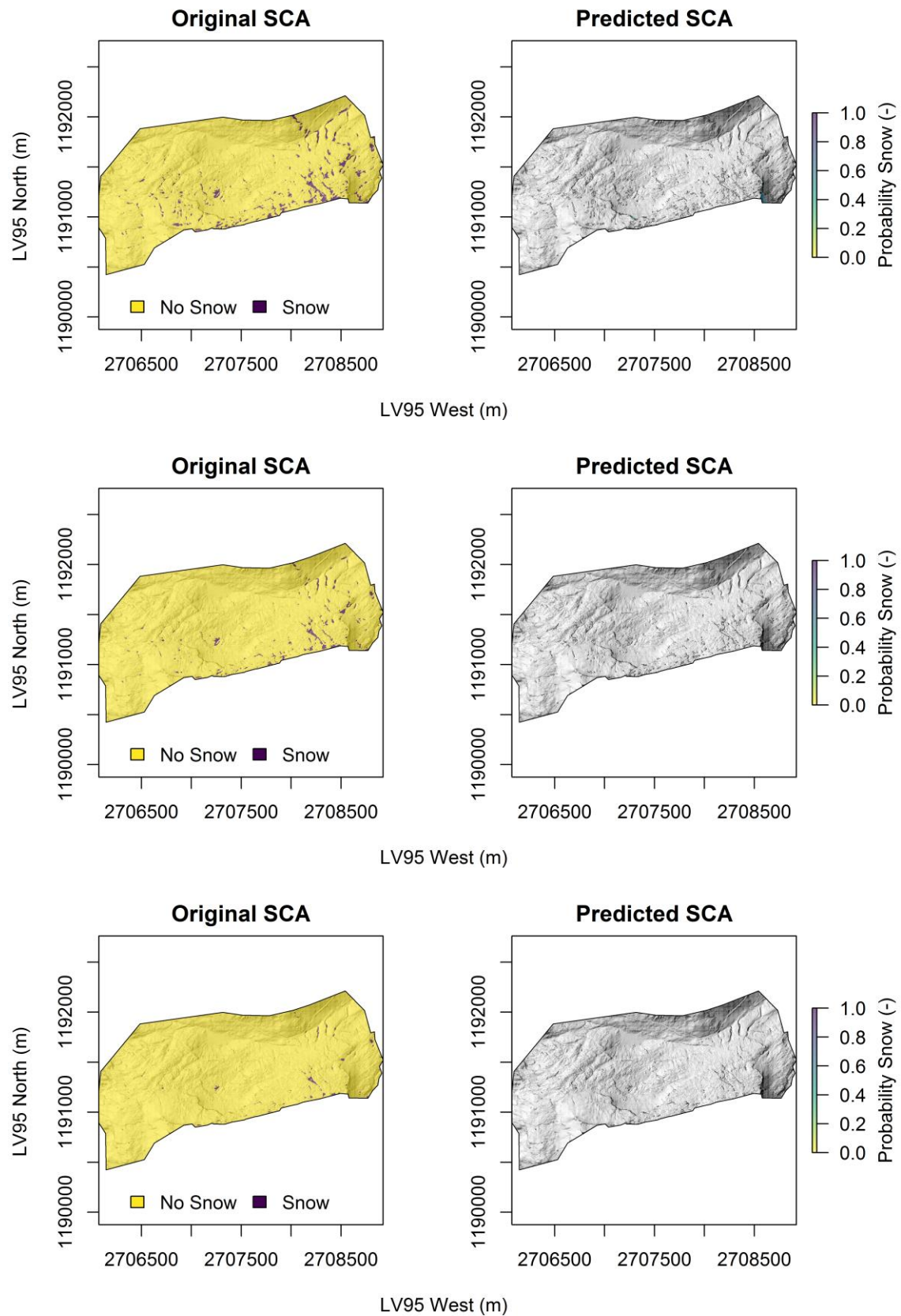


Figure A3: GLM output for Snow Cover Extent of July 10th (1), 17th (2) and 24th (3), 2019. Original (left) and predicted (right) SCA. As predatory variables were used Sx and elevation.

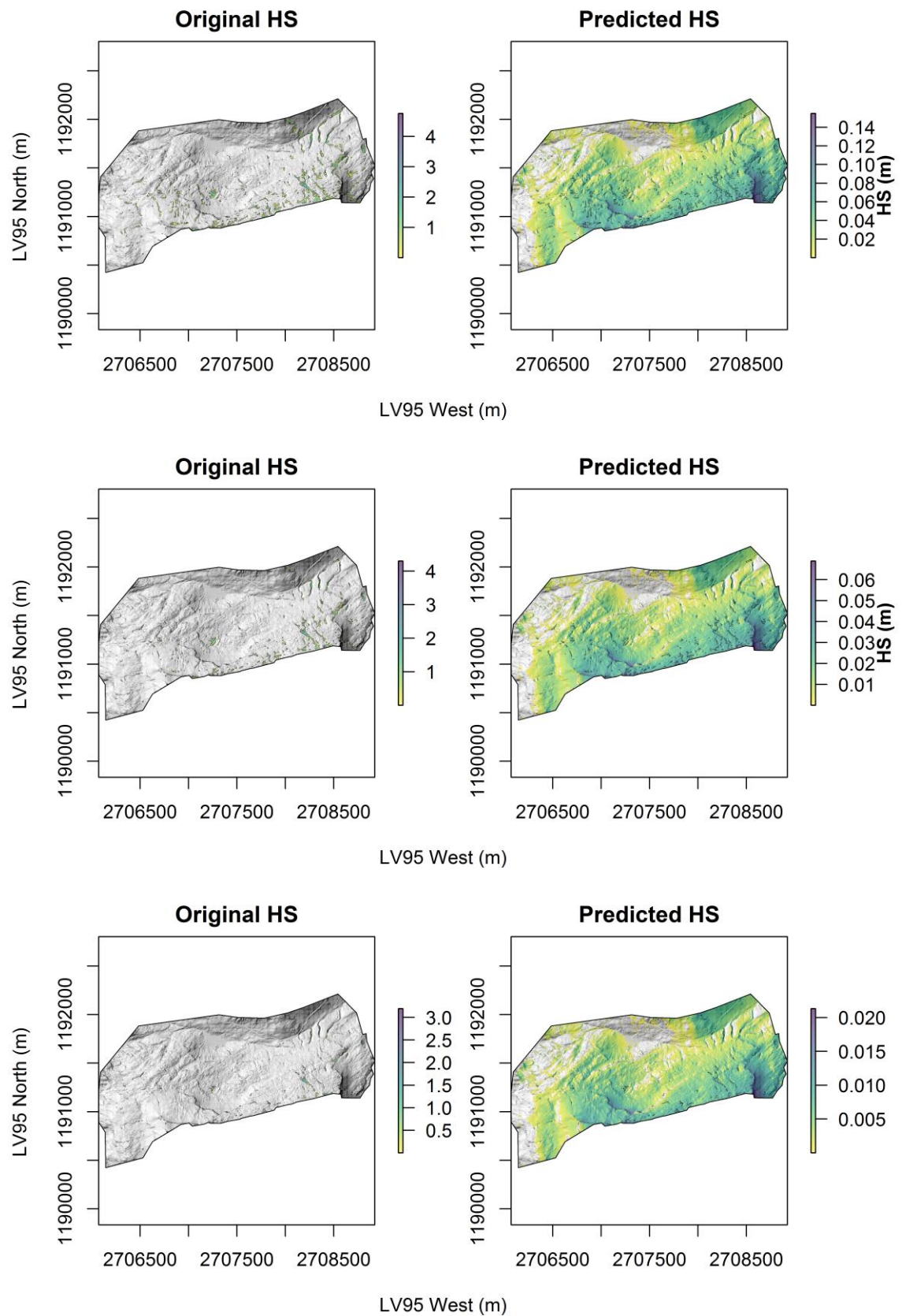


Figure A4: LM output for Snow depth of July 10th (1), 17th (2) and 24th (3), 2019. Original (left) and predicted (right) snow depth. As predictor variables were used Sx and elevation.

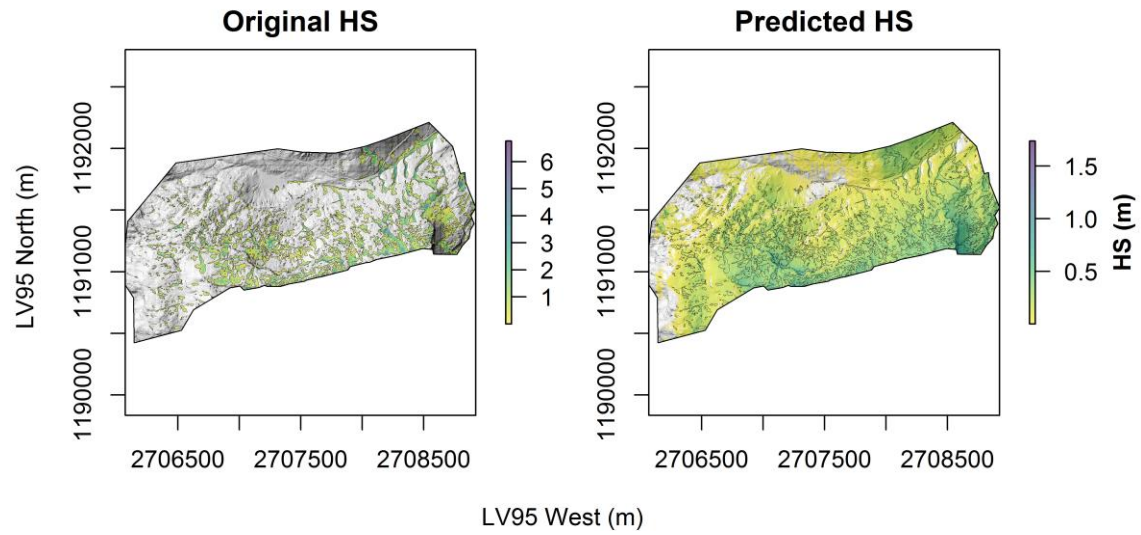


Figure A5: LM output for Snow depth of June 28th, 2019. Original (left) and predicted (right) SCA. As predictor variables were used S_x , elevation, slope and curvature.

The equation can be written as follows:

$$HS = -1.84 + 0.33 * S_x + 0.001 * Elevation + 0.0004 * Slope - 0.0001 * Curvature \quad (10)$$

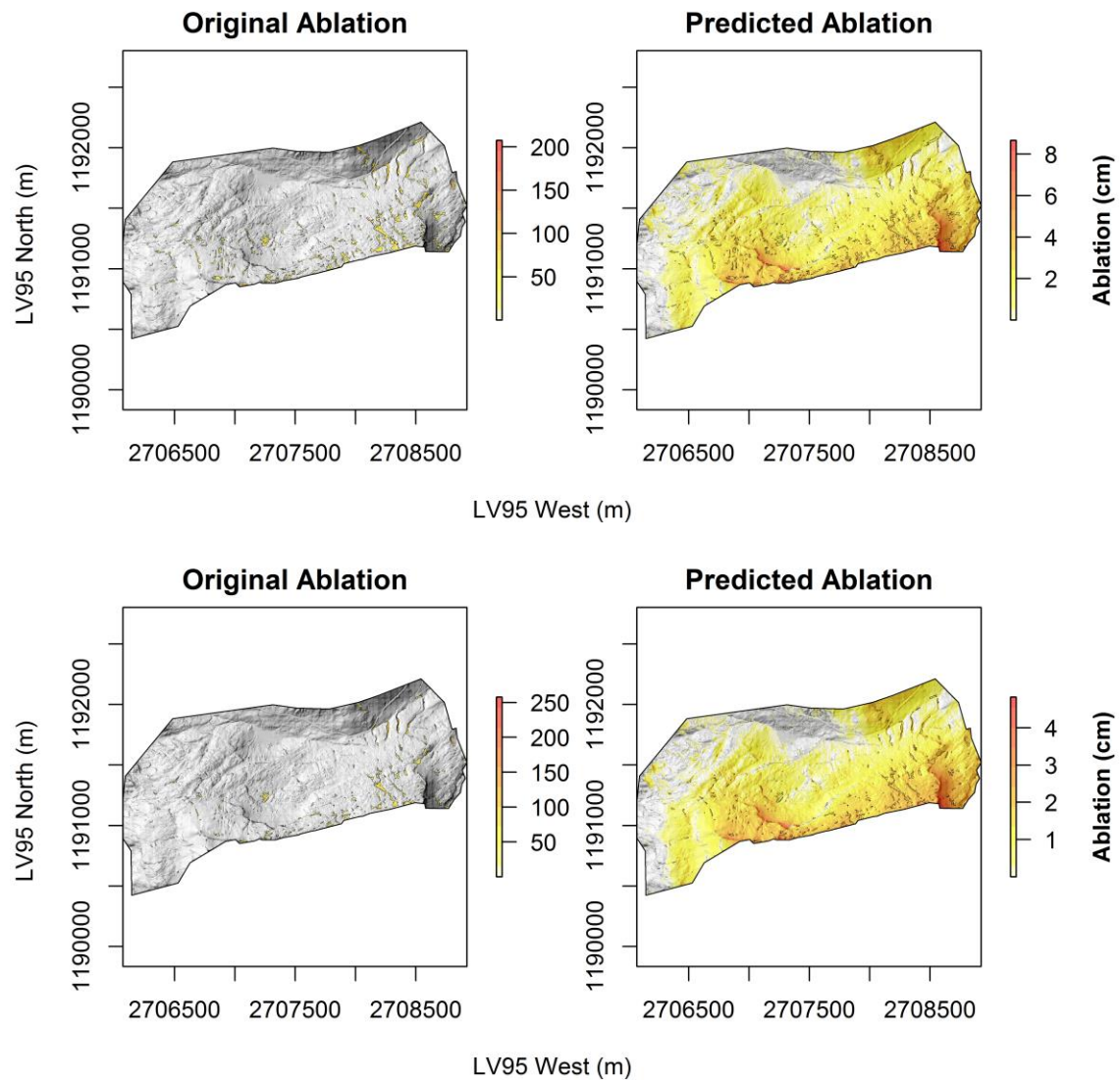


Figure A7: LM output for ablation between July 10th and 17th (1) and July 17th and 24th (2), 2019. Original (left) and predicted (right) ablation. As predictor variables were used radiation, Sx and elevation.

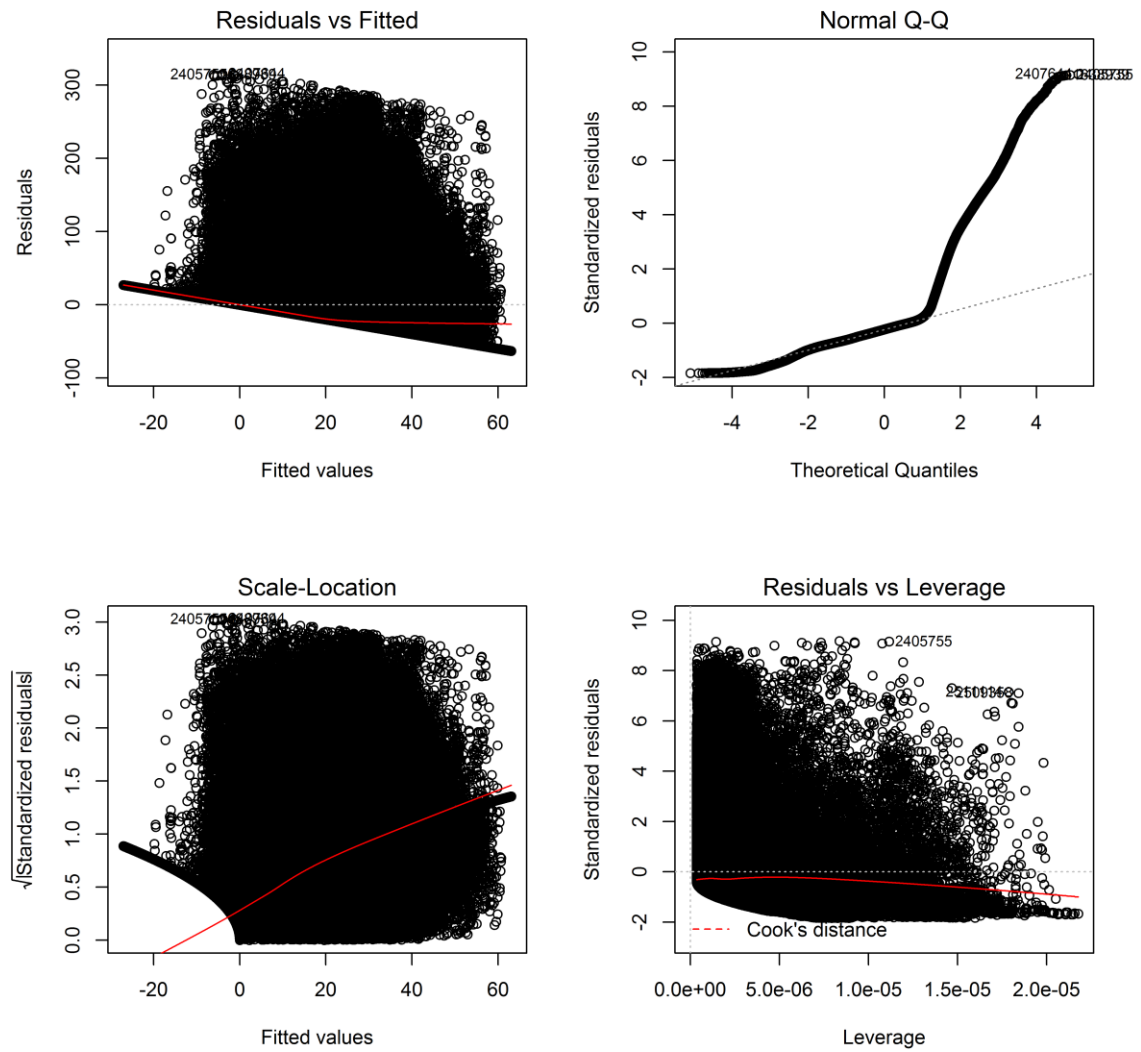


Figure A8: Diagnostical illustrations of the regression-analysis of the LM with ablation as dependent variable (June 28th–July 10th, 2019).

7.3 Tables

Table A1: RMSE of GCPs (June 28th, 2019).

GCP	X error [cm]	Y error [cm]	Z error [cm]	Total [cm]	Image [pix]	Image amount
1	-2.8	-5.3	17.9	18.9	0.1	11
2	-6.0	-1.3	-2.4	6.6	0.3	8
3	5.5	19.4	-18.1	27.1	0.1	26
4	-0.4	-0.6	17.2	17.2	0.1	13
5	10.5	-5.0	-14.5	18.6	0.1	8
6	-7.0	-3.6	5.0	9.3	0.0	1
7	10.5	-1.0	-8.5	13.5	0.2	3
8	5.9	-2.9	-4.0	7.7	0.2	7
9	-11.0	-2.4	0.9	11.3	0.1	9
10	-12.3	-0.8	11.3	16.7	0.1	7
Total	8.1	6.8	11.8	15.8	0.1	

Table A2: RMSE of GCPs (July 10th, 2019).

GCP	X error [cm]	Y error [cm]	Z error [cm]	Total [cm]	Image [pix]	Image amount
1	-9.1	-5.2	9.2	14.0	10.8	11
2	6.2	3.3	3.5	7.9	3.8	2
3	9.5	18.4	-21.3	29.7	9.6	20
4	-4.2	-1.0	9.2	10.1	8.6	22
5	-0.1	-0.4	-3.3	3.4	1.0	9
6	8.1	-6.8	-12.8	16.6	34.3	9
7	14.0	-16.0	9.2	23.2	1.5	3
8	-2.2	-0.1	1.3	2.5	2.3	5
9	-3.4	6.2	4.2	8.3	27.1	5
10	-18.8	1.7	0.9	18.9	9.6	8
Total	9.3	8.5	9.6	15.8	14.0	

Table A3: RMSE of GCPs (July 17th, 2019).

GCP	X error [cm]	Y error [cm]	Z error [cm]	Total [cm]	Image [pix]	Image amount
1	-9.7	-15.7	12.6	22.4	0.0	16
2	3.7	-3.4	-2.2	5.5	0.1	14
3	9.4	23.8	-19.9	32.5	0.1	34
4	-5.0	-2.4	5.9	8.0	0.1	20
5	6.2	12.3	3.7	14.3	0.2	5
6	4.1	-3.4	-19.9	20.6	0.2	14
7	9.4	6.2	19.7	22.6	0.5	3
8	-9.6	-17.5	-15.5	25.3	0.4	4
9	2.2	5.4	9.5	11.1	0.2	8
10	-10.7	-5.2	6.8	13.7	0.1	8
Total	7.6	11.8	13.3	19.3	0.2	

Table A4: RMSE of GCPs (July 24th, 2019).

GCP	X error [cm]	Y error [cm]	Z error [cm]	Total [cm]	Image [pix]	Image amount
1	-12.5	-18.4	5.2	22.9	0.2	16
2	-3.1	-4.7	0.2	5.6	0.1	13
3	15.9	22.5	-0.7	27.6	0.1	34
4	3.6	-3.2	3.2	5.8	0.1	18
5	4.1	0.3	-10.6	11.4	0.1	7
6	6.7	7.7	1.4	10.3	0.5	11
7	-7.7	-4.4	-12.1	15.0	0.6	4
8	-10.4	2.6	-4.2	11.5	0.1	12
9	5.4	9.2	9.2	14.1	0.6	10
10	-1.9	-11.7	8.3	14.5	0.2	10
Total	8.3	10.9	6.9	15.3	0.3	

Table A5: RMSE of GCPs (September 13th, 2019).

GCP	X error [cm]	Y error [cm]	Z error [cm]	Total [cm]	Image [pix]	Image amount
10	-1.9	-11.7	8.3	14.5	0.2	10
7	-7.7	-4.4	-12.1	15.0	0.6	4
8	-10.4	2.6	-4.2	11.5	0.1	12
4	3.6	-3.2	3.2	5.8	0.1	18
5	4.1	0.3	-10.6	11.4	0.1	7
9	5.4	9.2	9.2	14.1	0.6	10
6	6.7	7.7	1.4	10.3	0.5	11
3	15.9	22.5	-0.7	27.6	0.1	34
2	-3.1	-4.7	0.2	5.6	0.1	13
1	-12.5	-18.4	5.2	22.9	0.2	16
Total	8.3	10.9	6.9	15.3	0.3	

Table A6: Average camera location error (X – Easting, Y - Northing, Z - Altitude).

Date	X error [m]	Y error [m]	Z error [m]	XY error [m]	Total error [m]
Jun 28 2019	3.953	19.116	48.197	19.520	52.000
Jul 10 2019	-	-	-	-	-
July 17 2019	-	-	-	-	-
July 24 2019	103.744	31.426	47.242	108.399	118.246
Sep 13 2019	0.982	0.982	47.371	1.881	47.408

Ehrenwörtliche Erklärung

Hiermit erkläre ich, dass die Arbeit selbstständig und nur unter Verwendung der angegebenen Hilfsmittel angefertigt wurde.

Ort, Datum

Unterschrift